"OPTICAL AND ELECTRON MICROSCOPIC STUDIES ON INDENTED SILICON CARBIDE CRYSTALS "

A Thesis
presented to the Faculty of Science
of the University of London
in candidature for
the Degree of Doctor of Philosophy

by

Salah-Ud-Din M. Sc.

T
BPG
Din
138,705
Sept. 77

Tolansky Laboratory,
Royal Holloway College,
University of London,
Egham, Surrey.

January, 1977

ProQuest Number: 10097430

All rights reserved

INFORMATION TO ALL USERS
The quality of this reproduction is dependent upon the quality of the copy submitted.

In the unlikely event that the author did not send a complete manuscript
and there are missing pages, these will be noted. Also, if material had to be removed,
a note will indicate the deletion.

ProQuest 10097430

Published by ProQuest LLC(2016). Copyright of the Dissertation is held by the Author.

All rights reserved.
This work is protected against unauthorized copying under Title 17, United States Code.
Microform Edition © ProQuest LLC.

ProQuest LLC
789 East Eisenhower Parkway
P.O. Box 1346
Ann Arbor, MI 48106-1346

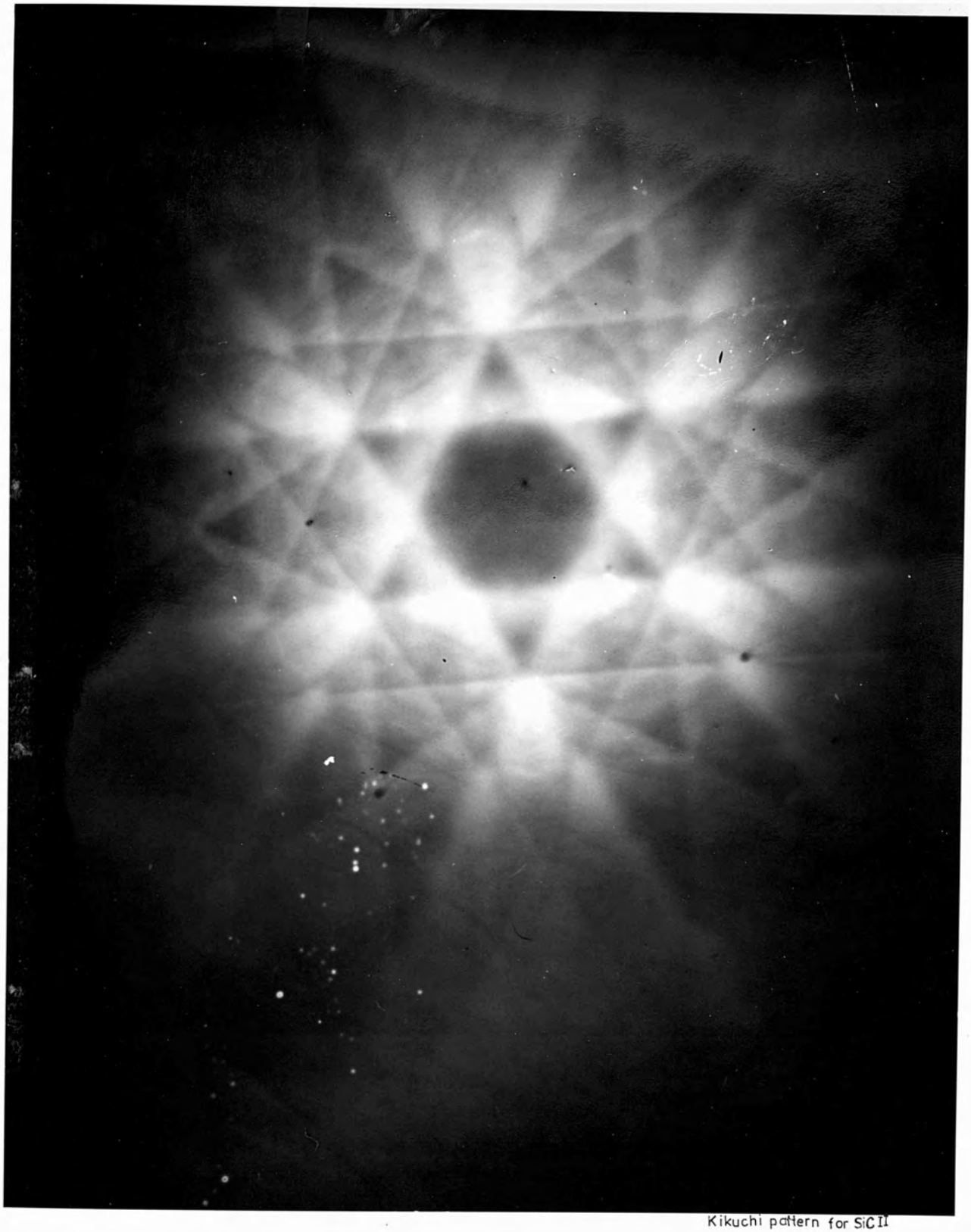

Kikuchi pattern for SiC II

Dedicated to my parents

ACKNOWLEDGEMENTS

The author wishes to express his profound sense of sadness at the loss of his teacher and supervisor, the late Professor S. Tolansky, F. R. S. Grateful acknowledgement is made for Professor Tolansky's continuous guidance and encouragement until his untimely death in March, 1973.

The author is indebted to Dr R. F. Miller for his constant interest, guidance and useful discussions throughout the last two years.

The author would like to record his appreciation of the assistance of Dr A. Shamim on the use of the Plasma Torch for annealing experiments.

The author is also indebted to McMaster University, Ontario, Canada, for allowing the use of the scanning electron microscope and the x-ray diffraction camera.

ABSTRACT

The static indentation hardness test has been applied to the study of the environment effects on hardness, plastic deformation, and fracture properties of silicon carbide crystals.

Measurements of microhardness on the (0001) planes show that the hardness of silicon carbide is significantly lowered by water absorbed from the air. Upon annealing the crystals, at very high temperatures, the hardness is found to increase.

A three-dimensional distribution of stress, beneath an indenter, has been evaluated using 'elastic equations'. The mechanics of crack initiation around the contact circle of a spherical indenter with the specimen has been analysed. The crack extension force, for a crack propagating downward from the surface of the specimen, has been evaluated.

Evidence of plastic deformation by slip is provided by a number of indentations, specially those with the spherical and double-cone indenters. $(10\bar{1}0)$ is the preferred slip plane.

CONTENTS

CHAPTER I

INTRODUCTION

CHAPTER I

Introduction

While considerable literature has built up concerning methods of measuring hardness and a great deal of hardness data have been accumulated on both metallic and non-metallic materials, during the 1950's and 1960's[1], the interest in the study of hardness impressions is fairly recent. Search for high strength materials, which resist wear, deformation and fracture, for various technological uses, make this study important. The main subject of this dissertation is hardness impressions on silicon carbide crystals with a view to find crystallographic deformation modes and understand propagation of indentation induced cracks. Other major areas included in the study are the following:

(i) Factors affecting the hardness of silicon carbide.

(ii) Relationship between the hardness anisotropy and the modes of crystallographic deformation.

In this introductory chapter a brief survey of four main applications of hardness test indentations will be described. These are as follows:

(a) Correlation of hardness with properties of materials.

(b) Plastic flow induced by hardness test indentations in ductile, and brittle materials.

(c) Directional hardness anistotropy and its relationship with effective resolved shear stress on slip systems.

(d) Indentation induced cracks.

Chapter 2 describes the material's properties. The experimental techniques used in this work have been outlined in Chapter 3. The constructional details of the ion-bombardment apparatus are given in this chapter. In Chapter 4, solutions for complex stress fields ,beneath an indenter (the diamond ball indenter), and crack extension force are given. The computed results of the stress field components (σ_{rr}, $\sigma_{\theta\theta}$, and σ_{zz}) and maximum shear stress are presented graphically in Chapter 5. The computed results of crack extension function $\psi(c/a)$ and the crack extension force are also presented. Effects of adsorbed water and annealing on indentation hardness are reported. Possibility of localized plastic deformation during hardness indentation of silicon carbide at room temperature is investigated. The results of hardness anisotropy are compared with the effective resolved shear stress. The ring cracks and vents cracks associated with the hardness impressions have been reported in this chapter. Finally, Chapter 6 contains discussions, conclusions and suggestions for future work.

1.1. The hardness test.

The indentation test, in this work, refers to a technique in which a fairly high pressure is applied within a localized area of a crystal by pressing a loaded indenter of a specific geometry. In line with the suggestions by Grodzinski[2], the hardness test has the

following types according to the range of load on the indenter:

(i) micro-indentation hardness test ... ... load (1-200 g)

(ii) light load hardness test ... ... load (200g-10kg)

(iii) macro-indentation hardness test ... load above 10 kg.

1.2 The geometry of the diamond indenters

1.2.1 The diamond pyramid (Vickers) indenter (Fig. 1.1.a)

Smith et al.[3] introduced a square-based pyramid with two opposite faces separated by an angle of 136°. This indenter is now commonly known as the Vickers indenter.

The Vickers hardness number (H_v) is given by the ratio of the load W, in kg, to the contact area of the impression, in mm^2,

$$\text{i.e.} \quad H_v = \frac{2\,W\,\sin\frac{\theta}{2}}{d^2} = \frac{1.8597\,W}{d^2},$$

where d is the mean of the diagonals of the impression in mm and $\theta = 136°$.

It is generally found that when the indenter is removed, after making the hardness test indentation, the impression is not a perfect square. For certain materials, the impression has concave boundaries due to 'sinking-in' of the material around the indentation. In these cases the diagonal are elongated and thus giving erratic low hardness numbers. In the case of highly worked materials, the impressions have convex boundaries, due to 'piling-up' of the material. This tends to shorten the diameter, therefore, an incorrect hardness number will be obtained. Certain corrections have to be applied in view of these effects.

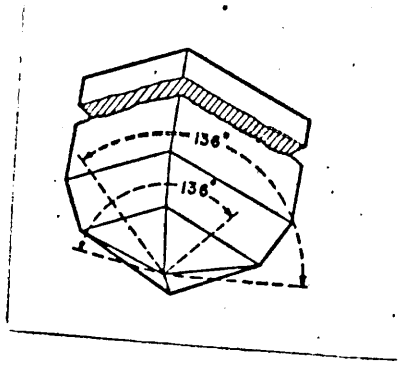

Fig.1.1.a.

The 136° diamond pyramid indenter

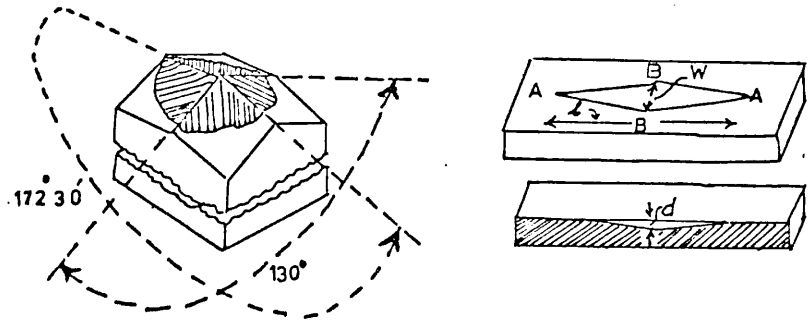

Fig. 1.1b. Shape of Knoop Indenter

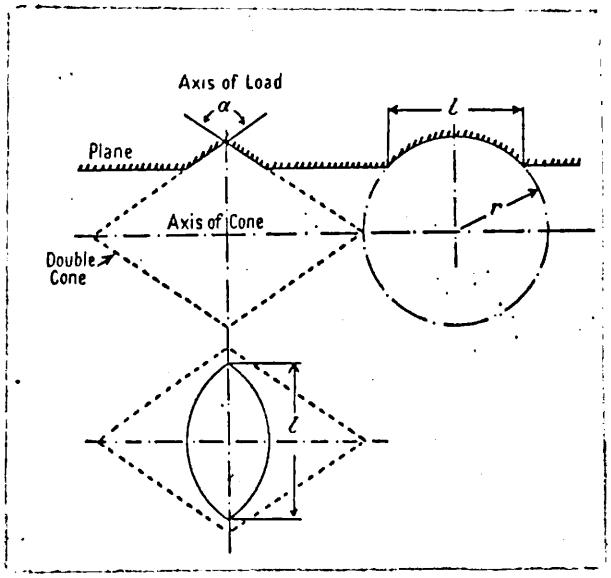

Fig.1.1.c. Geometry of a double-cone indentation.

1.2.2 The Knoop Indenter Fig. 1.1.b.

Knoop[4] constructed a diamond pyramid having a base in the form of an extended rhombus. The angles between the faces at the vertex of the Knoop pyramid are 130° and $172^{\circ}\ 30'$. The length AA is 7 times the width BB. The depth of the indentation 'd' is approximately 1/20th of its length. The geometry of the indenter is such that the elastic recovery of the indentation is greatest along BB and smallest beyond the length AA.

This indenter constitutes either an attachment to a metallographic microscope or an individual instrument. It is useful in the study of directional hardness anisotropy.

The Knoop hardness number (H_K) is given by

$$H_K = \frac{W}{0.07028.\ \ell^2} ,$$

where ℓ is the length of the long diagonal in mm.

1.2.3 The double-cone indenter.

The Vickers and the Knoop indenters have not received as much acclaim as the double-cone indenter. The pyramid indenter have sharp pointed ends, so when they are pressed against a hard material, there is a high concentration of stress near the ends. This stress concentration can result into the breakage of ends or damage to the walls of indentation. Grodzinski[5] introduced the double-cone indenter which has not got pointed ends. The double cone is cut from a single diamond. It may be considered equivalent to two right circular cones joined together base to base so that the

curved surfaces are apart by more than 90°. The indentation with this kind of indenter is elongated and shallow. (Fig. 1.1. c).

Grodzinski[5] shows that the area of the indentation, $A = \frac{\ell^3 \tan \alpha/2}{6\,R}$, where R is the radius of the cone, $\frac{a}{2}$ is the angle between the normal to the indented plane and the cone and ℓ is the length of the indentation. The depth of the indentation is shown to be equal to $\frac{\ell^2}{8\,R}$ and the width $\frac{\ell^2 \tan \alpha/2}{4R}$.

The double-cone hardness $(H_{dc}) = \frac{W}{C\,\ell^3}$ where C is a constant which depends on the geometry of the indenter and is

$$= \frac{\tan \alpha/2}{6\,R}$$

The indenter used in this study, had $\alpha = 154^{\circ}$ and R = 2 mm, therefore, the hardness number, $H_{dc} = \frac{W}{0.3609\,\ell^3}$

The indentations produced by the double-cone indenter are much shallower than those which would be produced by the Vickers and the Knoop indenter, on the same material. There is very small recovery in the length of an indentation. A large recovery takes place along the width but the width does not come into the formula.

1.3 Uses of the hardness test

The hardness test is widely used for measuring certain mechanical properties of materials, despite the fact that sophisticated techniques are available. The reason is that it is quick, simple, convenient and non-destructive. It may be applied to make an estimate of those mechanical properties of materials which have a

specific correlation with their hardness. A number of important uses of this method occur in connection with the possibility of applying concentrated or point loads in studies of plastic deformation, identification of slip system, dynamic character of dislocations and fracture of crystalline solids.

While considering the application of the hardness test, the materials which exhibit similar mechanical behaviour are considered to be in one group. This is done to secure a full understanding of the process taking place in a certain group. The materials under investigation fall into three groups, 1) ductile, 2) semi-brittle, and 3) very brittle.

The hardness test has little or no advantage over the conventional bulk testing methods in studying the process of deformation in ductile materials. Large single crystals with oriented surfaces can easily be prepared. The samples can be tested under controlled conditions in simple bending, compression and tension. In the case of hard and brittle materials the difficulty is the preparation of large quality single crystals of oriented surfaces. Most of the brittle materials have a low thermal shock resistance, therefore, they require a slow cooling after bulk deformation. The hardness test is particularly useful for the investigation of plastic deformation, because high [illegible] pressures are developed beneath an indenter which can initiate plastic flow even at room temperature. For semi-brittle materials, the hardness test has been found to be equally important as for the brittle materials. It has been used to

study the effects of surface condition on the bulk mechanical behaviour and to examine the dependence of dislocation mobility on temperature, impurities and environment.

1.3.1 Hardness and properties of ductile and semi-brittle materials

Up to the present time there have been many attempts to correlate hardness and physico-chemical properties of materials. Richer[6] attempted to interpret hardness on the basis of the stress/strain relationship in a tensile test. Davidenkov[7] constructed stress/strain diagrams from hardness measurements. Hill[8] and Tabor[9] have shown that an indenter may be considered as a flat rigid die penetrating an elastic-plastic material. The Vickers hardness number, H_v, of the fully work-hardened material and the corresponding yield stress Y, are related by the equation

$$\frac{H_v}{Y} \simeq 3$$

Boeklen[10] obtained a correlation between hardness and stress-strain diagrams with the energy balance. Braun[11] found a connection between structural conditions of material and character of load dependence of hardness. He differentiated between a fully annealed specimen and one having been cold-worked to give a permanent strain. According to him, there was a relationship between hardness and extension to fracture, the latter being influenced by the degree of cold-work. Murphy et al.[12] expressed the relation between ultimate strength and Vickers hardness number for various metals as:

$$Y = A + B H$$

where H is hardness number, A and B are the constants dependent on the moduli of the material under hardness test. Chuze et al.[13] found a correlation between hardness and heat conductivity in non-metallic crystals.

Microhardness test (also called micro-indentation hardness test) arose as a result of an investigation into the measuring conditions such as using very small loads. A number of papers have appeared, in the literature, on the use of the microhardness test for studying individual structural components of metallic alloys and mixed single crystals. Bochvar et al.[14] and Sauliner[15] studied the structural components of cast aluminium-copper and aluminium-silicon binary alloys by this method. Drits et al.[16] used this method to study structural constituents of alloys of Pb-Sb, Pb-Sn and Sn-Sb systems. Their investigations showed that microhardness of the eutetic remained constant. Friedkin[17] evaluated work-hardening of walls of holes by microhardness tests. Brenner et al.[18] made a hardness study of multiple diffusion of beryllium in very pure aluminium., Bueckle's[19] investigations on supersaturated Al-Mn alloys revealed that heterogeneities in metals cause characteristic bends in microhardness curves. Gudtsov et al.[20] investigated the ageing process of metals and alloys by microhardness measurements during vacuum anneal. Arkharov et al.[21] studied the hardening at grain boundaries of alloys of high purity copper with 1% Zn, Ga, Ge, Sn and Sb. A number of workers have used this test to study the properties

of electro deposited metals. Using this method the influence of the thickness of the deposit on the structure and properties of electro-deposited metals, was studied by Sammour et al[22]. The relation between hardness and grain size was found to be almost linear. Glazov et al.[23,24] applied this test to the investigation of binary and ternary equilibrium diagrams of metallic systems. Glazov et al.[25] and Chernevaskaya[26] applied this method to study the composition of solid solutions. Chernevaskaya showed that the formation of a solid state solution in a two component system, e.g. CaF_2-SrF_2 single crystals, is accompanied by an increase in microhardness. In the absence of a solid solution the micro-indentation hardness was almost constant. Koval'skii et al.[27] also observed a linear relationship between the microhardness and the composition in TiC - NbC.

1.3.2 Hardness and properties of brittle materials

A direct linkage has been established by several investigators between microhardness and crystal's chemical properties. Povarennykh[28] found that crystals with covalent bonds were harder than those in which ionic bonds were predominant. The chemical bond in monocarbides of transition metals and its effect on the hardness of compounds were studied by Howotny et al.[29]. They found that the hardness of the carbides was mainly determined by the covalent bonds. Wolff[30] indicated the dependence of the microindentation hardness for elements of silicon carbide groups, and compounds of the A^{III} B^{V} or

A^{II} B^{VI} type on the interatomic distance. Petzold[31] interpreted the microhardness of some silicates and glass on an atomistic basis.

According to Goldschmidt[32] the hardness for salt crystals, on Moh's scale, was given by the expression

$$H = S \cdot e_a \cdot e_c \cdot r^{-m},$$

where e_a and e_c are the valences of the ions [illegible] of the anions and cations, r is the interatomic distance; S, m are constants. Rebinder[33,34] used the microindentation hardness test as a tool of investigation of the effects of surface-absorption environment on the surface free energy of a solid. Gendelev et al.[35], on the basis of experiments on crystals of yttrium iron-gallium and iron-aluminium garnets, established a relation between the microhardness of the faces and the external shape of the crystals. They found that on the (110) face the [111] direction always had the smallest microhardness. This anisotropy was believed to be due to the comparative ease of penetrating between <111> rows in which the nonintersecting columns of octahedra occur.

Goryunova et al.[36] studied the relation between hardness of semi-conductor compounds of the A^{II} B^{IV} C_2^V type and certain electronic properties such as heat resistance and activation energy of the intrinsic electrons. They found that as the metallic nature of the compound increased, the mechanical strength, heat resistance and the activation energy of the intrinsic electrons decreased.

1.4 Plastic flow around hardness test indentations in ductile materials

It has long been recognised that when an indenter, usually a ball, cone or pyramid, presses strongly enough on the surface of a crystal, it creates surface distortions around indentations. These distortions are commonly described as either 'piling-up' or 'sinking-in' (See Fig. 1.2). O'Neill's [37] work is probably the first phenomenological analysis of these effects. Crow et al.[38] and Lysaght[39] studied the characteristics of these distortions in heavily cold-rolled strips and plastics, respectively, and adopted similar classifications as O'Neill. According to O'Neill, 'piling-up' is a condition in which the perimeter of the surface of contact of the indenter and the sample is above the original level. This type of distortion will naturally lead to convexity in the superficial outline of a pyramid indentation if the distortion, as may be expected, is less at the corners than at the opposite faces. In the case of ' sinking-in', the perimeter of the contact is below the original level and concavity will,therefore ,result. In O'Neill's classification , no account of the influence of recovery has been indicated and same is true of Lysaght's classification of distortions. Thibault and Nyquist[40] used an optical polarization method to examine the flow of material around the Knoop indentations on silicon carbide crystals. They found that the affected material generally extended from the centre of the indentations to a distance approximately equal to the length of the long diagonal. Yakutovich, Vandyashev and Surikova[41] used a

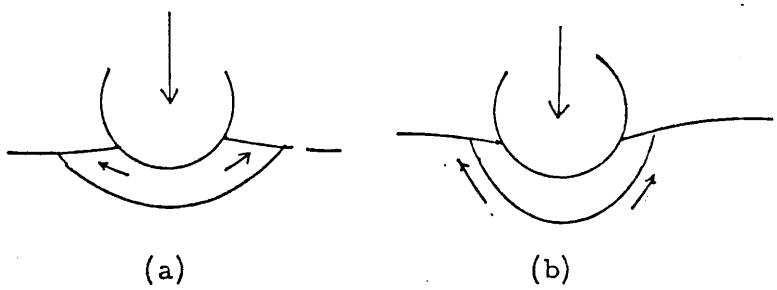

Fig. 1.2 .

(a) For highly worked metals the flow of metal around the indenter produces ' piling-up ', (b) for annealed metals the displacement of metal occurs at regions at a small distance from the indenter so that ' sinking-in ' occurs.

probe method to measure indentations and flow patterns. A probe attached to an accurate dial gauge was lowered until it made electrical contact with the surface. A profile section of the surface was obtained by means of a traversing mechanism and dial readings. This method is satisfactory for measuring large indentations (diameter more than 1 mm). Tolansky et al.[42, 43, 44, 45] employed highly sensitive multiple beam interference methods to investigate the flow patterns produced by hardness indentations on tungsten carbide; nickel-steel, duraluminium and tin. Currently, an increasing number of investigators are resorting to this technique. Boyarskaya[46] has investigated the plastic flow in PbS crystals using interferograms of the indented surfaces. Takeo[47] applying this technique to Mn-Zn ferrite single crystals observed significant bending of interference bands close to the hardness impressions which he belived was due to a slight rise of the surface near the impressions.

1.4.1 Plastic flow during indentation of semi-brittle materials

Smakula[48] and Klein[49] are probably the first to describe the indentation in terms of slip process. Seitz[50] introduced the concept of prismatic dislocations and prismatic punching. Gilman and Johnston[51] were first to note that dislocations can be revealed by etching the crystals. Gilman and Johnston working on LiF crystals and Stokes[52] on Si, independently showed that dislocations can be introduced by dropping small hard spheres on the crystals. Ever since Gilman's experiment of direct observation of dislocations

by etching, the hardness test combined with the etch method has been used by several investigators in studies of processes such as generation and multiplication of dislocations, origin and multiplication of glide bands, dislocations motion etc.

Etch pits around indentations on the (100) faces of ionic alkali halide crystals with rock salt type structure [NaCl, LiF, NaF, KCl,] have been found to be in the form of a rosette. The eight rays of the rosette, Fig. 1.3, correspond to the intersection of (110) plane with the cleavage plane (100). The diagonal rays (made up of tiny etch pits) along the <110> directions correspond to the edge components of half loops on {100} planes at 90° to the surface, and the rays along <110> correspond to the screw components of half loops on the (110) planes at 45° to the surface. Indentations on (001) plane of PbS, which has covalent bonding, show a rosette with four rays after etching. The analysis of three-dimensional etch pit distribution reveals that primary slip in PbS occurs as <110> (100). In ionic crystals of rock salt structure it is <110> (110).

1.4.2 Plastic flow around hardness test indentations in brittle materials

Brittle materials generally possess a covalent bond or there is a considerable portion of covalent bonding. They do not show any bulk deformation when stressed at room temperatures. Dislocation motion is restricted due to a large lattice resistance. Plastic deformation by slip may occur when such a material is heated at a temperature approximately equal to 2/3rds of its melting point.

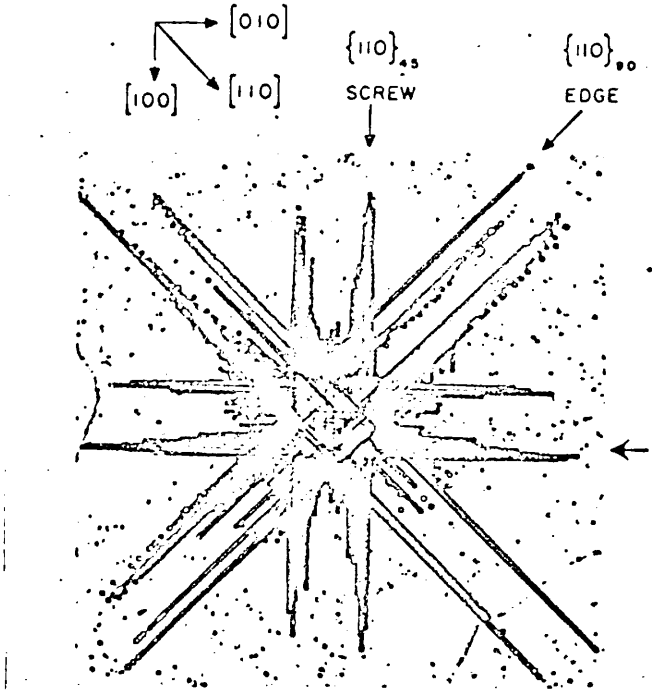

Fig.1.3 . Rosette made of rows of etch pits around a Vickers indentation on (001) surface of MgO.

Certain covalent materials, such as metal carbides, ceramic alumina and semi-conductors silicon and germanium, have been observed to deform plastically even at room temperature by hardness indentations. The plastic deformation due to hardness indentations, however, is localized in a small region around an indentation. In some cases it is so small that use must be made of electron microscopy.

During the last decade, there has been a considerable interest in the indentation studies on these materials. Plasticity of Ge and Si crystals, at room temperature, by hardness indentations, has been a controversial subject. Churchman[53], Trefilov et al.[54], Sumino[55], and Krylov and Iveronova[56] made hardness indentations on Ge and Si crystals. They used the etching technique to find out whether these materials had been deformed. They all agreed that dislocation motion was not detectable unless the indentations were made when the crystals were at 500°C or above. Pugh and Samuel[57] and Johnson[58] found fresh etch pits on etching Ge crystals which had been subjected to impacts by falling tiny hard spheres. They believed that the cracks, which were produced by the impacts, were responsible for the generation of dislocations. Tramposch and Rinder[59], making hardness test indentations with a spherical indenter when the crystals were inside a warm etchant, observed characteristic etch patterns around the indentations. Craig[60], Ikeda[61] and Rinder[62] found that annealing the indented crystals before etching helped in revealing the otherwise undetectable etch patterns. But it could not be decided

whether the annealing resulted in the dislocation motion in order to relieve the internal stresses or resulted in the generation of dislocations to relieve the elastic energy which was stored during the indentation. The answer to this question was provided by Carroll[63] and Nikitenko et al[64]. They observed dislocations in the vicinity of the hardness indentations, by electron microscopy techniques, without annealing the specimen after indentation.

The material which has been so extensively investigated for evidence of plastic deformation at room temperature as much as Ge and Si crystals is aluminium oxide (α-Al_2O_3). Palmour et al[65] observed plastic flow in sapphire. Recently, Hockey[66] and Rozhanskii et al.[67] made independent studies on indented sapphire crystals using a transmission electron microscope. Both found an evidence of plastic deformation in sapphire indented at room temperature.

Refractory carbides have probably received the widest attention, on studies of their plasticity at room temperature, in order to understand the process of abrasive wear and the residual effects of surface conditions on mechanical, chemical and electrical properties.

The results of recent experiments on refractory carbides have been summarised in Table I. 1 with brief remarks.

TABLE I.1 Plasticity of some transition metals carbides/refractory carbides by room temperature indentations

Material	Structure	Investigator	Predominant slip systems		Method of observation
			Primary	Secondary	
Tungsten Carbide		Corteville et al.[68]	$<11\bar{2}0>(0001)$	Prismatic $<11\bar{2}0>(10\bar{1}0)$	Optical microscopy
		French and Thomas[69]			
	Hex.	Takahashi and Freise[70]			
Molybdenum Carbide	Hex.	Vahldiek[71]	$<11\bar{2}0>(0001)$	Prismatic $<11\bar{2}0>(10\bar{1}0)$	Optical microscopy
Uranium Carbide	cubic	Rhodes[72]	$<110>(001)$	$<110>$ (111)	Etch-pit technique
		Hannink[73]	$<110>(111)$		
Niobium Carbide	cubic	Rowcliffe[74]	$<110>(110)$		
		Morgan et al.[76]	$<110>(111)$	$<110>$ (110)	
Titanium Carbide		Hannink et al.[75]	$<110>(110)$		
		Rowcliffe[74]			
Tantalum Carbide	cubic	Rowcliffe[74]	$<110>(111)$		Optical and etch-pit techniques

(continued ....)

TABLE I.1 (Continued)

Material	Structure	Investigator	Predominant slip systems		Method of observation
Vanadium Carbide ($VC_{0.84}$)	cubic	Rowcliffe[74]	$<110>(110)$		
Hafnium Carbide	cubic	Rowcliffe[74]	$<110>(110)$		Optical and etch-pit techniques
Zirconium Carbide	cubic	Hannink et al[73]	$<110>(110)$		
α- Silicon Carbide	Hex. II	Shaffer[78]	$(10\bar{1}0)<11\bar{2}0>$	*secondary $(0001)<11\bar{2}0>$	Optical technique and Electron microscopy using replica technique
		Present work	$(10\bar{1}0)<11\bar{2}0>$		
	Hex. I		$(10\bar{1}1)<01\bar{1}4>$		

*(Believed to be operating at very high temperatures)

1.5 Anomalous Hardness

Despite a considerable amount of work that has been done in the field of hardness testing, there have been significant anomalies between the results of various workers investigating the same problem, some of which have not been resolved. The discrepancies arising due to errors in making and measuring hardness impressions can be resolved if these errors are kept to a minimum. There has been a big controversy over the question as to whether recovered hardness is independent of the load. Hardness numbers obtained at high loads have been fairly constant for a material but for the lower range of loading diverse results have been obtained. Of the many workers who investigated the variation of hardness with load a majority of them obtained results which showed an increase in hardness with decrease in load. Examples of this type of variation are found in papers by Knoop[4], Berhardt[79], Mitsche[80], Schulze[81]. Samuels[82], Mott[83] and others[84,85], however, noted marked decrease in hardness with load. Meincke[86] and Grodzinski[5] from their studies on sintered silicon carbide, indented with Vickers and double-cone indenters, found that as the load on the indenter was increased an increase in hardness to a certain maximum value occurred according to a hyperbolic law. Onitsch[87] attributed the difference in hardness numbers for the two ranges of load, in a polycrystalline material, to the fact that the low load hardness impression (micro-indentation) is entirely within a grain, in contrast to several grains covered by an impression at

high loads . Even this concept is not in accordance with the experimental observations. For instance, it does not explain why for a particular grain size, a decrease in indentation size should have further effect on the hardness. Grodzinski[5] redefined hardness independent of load and expressed it as

$$\text{Hardness } H = \frac{P}{d^n}$$

where n is a constant of the material under examination and H is the load producing a recovered indentation of unit length, i. e. d = 1.

During the past few years, materials scientists and metallurgists have reviewed the low load hardness anisotropy in the light of the effects of the environment. Rebinder[33] was the first one to discover the effect of environment on the flow properties of solids. The effect arising from the surface active species has been termed the "Rebinder effect". Mitshe et al.[80] and Walker et al.[88] studied the effects of adsorbed water on hardness in non-metallic materials. Westbrook[90] and Jorgensen[89] introduced the idea of "wet" and "dry" hardness. The former refers to the hardness measurement in the ambient air and the latter in the dry condition when the solid is desorbed, quenched and tested in anhydrous reagents like lithium aluminium hydride in ether or dry toluene . Their results for some ionic and covalent solids showed time independent hardness in dry condition. In the "wet" condition, hardness was found to be lowered and time dependent. This type of variation in hardness was termed by them as "Anomalous Indentation Creep."

1.6 Directional Hardness anisotropy.

Hardness anisotropy is a well-known phenomenon. Much work has been reported in this field for many metals and non-metals, both cubic and hexagonal structures. One of the earliest experiments in which the directional hardness was indicated was by O'Neill[91] who pressed steel balls against aluminium single crystals and observed that the resulting impressions were elliptical. Schulz and Hanemann[92] found that Vickers diamond indentations on aluminium crystals were slightly asymmetric. They attributed this asymmetry to the directional hardness anisotropy. Hardness tests on these crystals by O'Neill[91] showed a small difference in hardness of the (100), (110) and (111) planes. Winchell[93] and Thibault et al.[40] initiated the study of directional hardness of minerals using Knoop indenters. Daniels and Dunn[94] investigated the effect of crystal orientation on Knoop hardness of metallic single crystals. They found that the hardness of silicon ferrite varied periodically with direction of the long diagonal of the Knoop indenter with respect to the crystal. Tolansky et al.[45] studied the directional hardness variations in tin and bismuth crystals. Sandulova[95] investigated the anisotropy in hardness of silicon. Ablova[96] reported anisotropy in germanium. The anisotropy between (111) and (100) planes of Si was 22%, and 15% between (111) and (110) planes of Ge. Attinger[97] found that the double-cone hardness of α-Al_2O_3 varie from 950 to 2070 Kg/mm^2. Stern[99] observed hardness variations on different planes of silicon carbide crystals. Garfinkle and Garlick[98] have shown that Knoop hardness values for several cubic crystals do

not depend on the crystal plane but only on the crystallographic directions. In the case of hexagonal crystals, however, the hardness differences in different planes have been observed. Work of Meincke[99] on zinc and copper crystals has provided the first evidence supporting these observations.

It is difficult to discuss adequately the results of all papers which have appeared recently on directional hardness anisotropy. The fact that a wide range of directional hardness values has been reported in the literature for hexagonal silicon carbide crystal has called our attention to this material. For instance, Peter and Knoop[100] examined the microhardness of black and green silicon carbide crystals and report average Knoop hardness as 2100 Kg/mm^2 with a maximum of 2140 Kg/mm^2. According to them the hardness decreased midway between $[\ 10\bar{1}0\ ]$ and $[\ 11\bar{2}0\ ]$ orientations on (0001). Shriramurty[101], using a double-cone indenter, showed that SiC has a maximum hardness 3307 Kg/mm^2 along a $<11\bar{2}0>$ direction and minimum as 1992 Kg/mm^2 at 40^o to it on one side and 20^o on the other side on the basal plane. Shaffer[78] did not notice any anistropy on the basal plane but found a difference of 800 Kg/mm^2 between the hardest and softest direction in the crystal on the prismatic plane $(10\bar{1}0)$. It appears that the divergence of the various values is due to the poor technique of measuring the actual size of the impression due to incipient cracking at the corners of indentation.

1.6.1 Directional hardness anisotropy and effective resolved shear sress (E.R.S.S.)

Daniels and Dunn[94], while carrying out their studies on the directional hardness anisotropy, in silicon iron and zinc crystals, using the Knoop indenter, proposed a model according to which the hardness was determined by an effective resolved shear stress (E.R.S.S.). In this model, they assumed that only one slip system was acted upon by all the four facets of the indenter, namely, the slip system for which E.R.S.S. of any of the individual facets was the highest. According to this model, the material beneath an indenter is assumed to be deformed by a tensile force parallel to the steepest slope of the individual facets of the indenter. The rotation of the element of material close to the facets of the indenter is taken into account. The effective resolved shear stress is expressed by the well known equation

$$\tau = \frac{F}{A} \cdot \cos\Phi \cdot \cos\lambda \cdot \cos\psi$$

(See Figs. 1.4 a-c for explanation of the symbols)

where,

F = applied force
A = area supporting F
λ = angle between axis of F and slip direction (SD)
Φ = angle between axis of F and normal to the slip plane (SP)
ψ = angle between the axis of the indenter and axis of rotation (AR) for a given plane system.

The term $\cos\psi$, in the above equation is called the ' constraint term '. It is a measure of the ease with which a slip system may rotate to allow the penetration of the indenter. According to Brookes[211], this constraint term of Daniels and Dunn is incompletely defined. For instance, consider an indentation on the (001) plane of a MgO crystal and its two slip planes [110] at right angles to it.

By setting the angle $\psi = 90^{\circ}$, i.e. when the indenter's facets are parallel to one of the 90°-type slip planes, the constraint term becomes zero. But this was not found to be the case. Because the E.R.S.S. is zero on these planes only when 'H', the axis parallel to the indenter facet and perpendicular to 'F', is along the $\langle 110 \rangle$ direction. . For all other orientations of the indenter slip can occur on the $\{110\}\langle 1\bar{1}0 \rangle$ slip systems. This is supported by the etch pits which are found parallel to these planes. According to Brookes, the maximum constraint is not defined by $\psi = 90^{\circ}$ alone. It is necessary for the slip direction 'SD' to be parallel to 'H' so that 'AR' is at 90° from 'H'. If γ is the modifying angle, then the constraint term is $= \frac{\cos \psi + \sin\gamma}{2}$

The modified expression for the E.R.S.S. is, therefore,

$$\tau = \frac{F}{A} . \cos\phi . \cos \lambda . \frac{\cos \psi + \sin\gamma}{2}$$

Several investigators [201, 202, 94] have successfully explained the hardness anisotropy, in crystals with similar slip sytems, using the E.R.S.S. distribution on the slip planes. It has been suggested that bulk plastic flow within the crystal controls the hardness anisotropy.

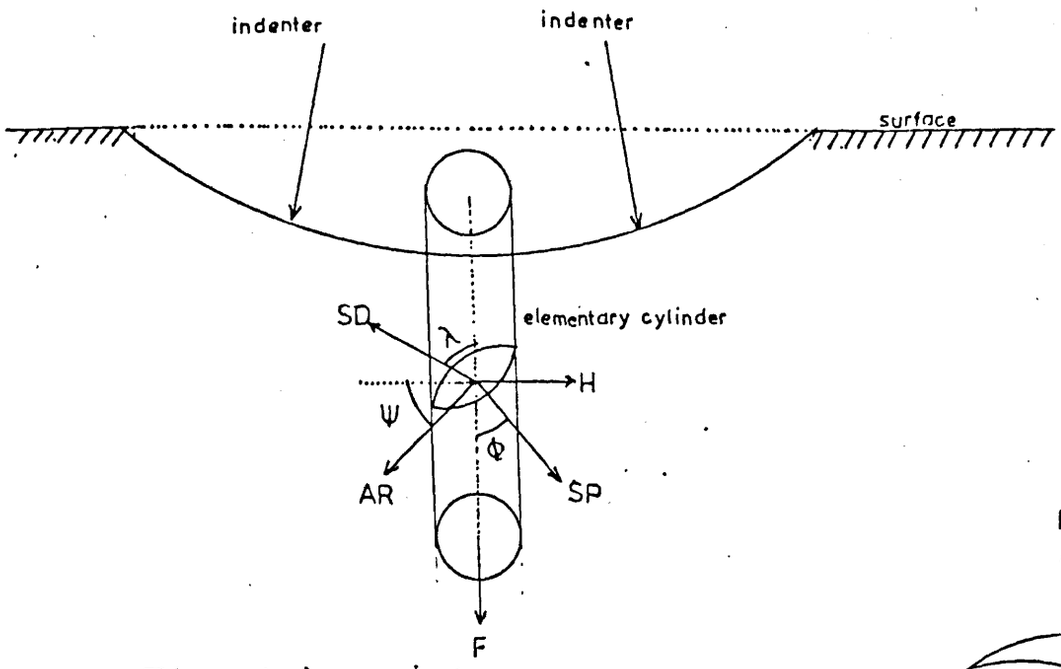

Fig. 1.4 . (a)

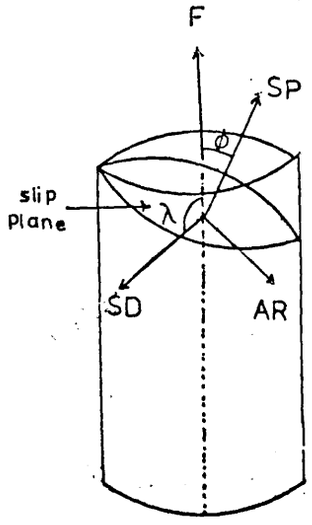

(b)

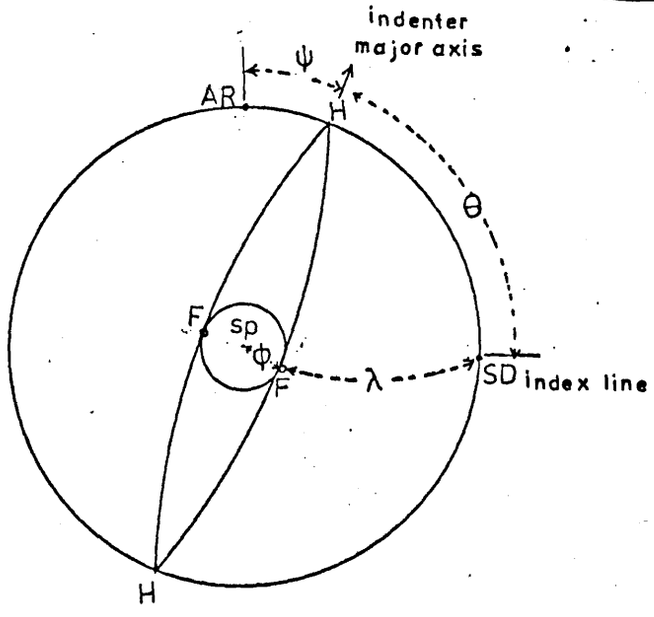

Fig. 1.4 . (c)

1.7 Plasticity of silicon carbide crystals

The role of screw and edge dislocations, intersecting the basal planes, in the growth of silicon carbide crystals, is now an established fact.

Verma and Amelinckx[102-105][106-109] explained the spiral growth patterns on the screw-dislocation theory of Burton, Cabrera and Frank.[110] Mitchell[111] established a correlationship between screw dislocations and the known polytypes of silicon carbide. Bhide and Verma[112] realised that the concept of pure screw dislocations could not explain all the growth features on silicon carbide crystals. They proposed a combination of screw dislocations and edge dislocations which could give a satisfactory explanation of some of the growth features. Horn and Gevers[113][114] used the conventional etch technique for studying dislocations in silicon carbide.

Amelinckx et al.,[115] were the first to show that silicon carbide (type II) has characteristics of those materials which can be deformed plastically at high temperatures. They found evidence of dislocations with $<11\bar{2}0>$ Burgers vector intersecting the basal planes. Using X-ray diffraction microscopy, they found that some $<11\bar{2}0>$ Burgers vectors also intersect another plane viz. the corrugated plane $(\bar{3}301)$ - a pseudo plane composed of $(1\bar{1}01)$ and $(\bar{4}401)$ strips. Their observations, thus, established the possibility of cross-slip. Hamilton[116] determined the Burgers vector of purely screw dislocation as $<0001>$ for the 4H type silicon carbide whiskers.

At room temperature, well-defined Vickers and Knoop hardness indentations have been produced by Hockey[117] in 4H type silicon carbide and corundum crystals. He observed high dislocation densities beneath the indenters.

1.8 Birefringence

In the case of an isotropic material, an electromagnetic radiation is transmitted with equal velocity in all the directions. This is generally the case in crystals in the cubic system. In anisotropic materials, the transmission of an electromagnetic radiation will vary according to the direction of the ray in the crystal.

Birefringence or double refraction is a phenomenon which is associated with anisotropy. Even non-crystalline materials such as glass, which normally act as isotropic crystals, become anisotropic when strained and show birefringence. Similarly, crystalline silicon, which is isotropic, has been observed[118] to be birefringent when strained. The birefringent patterns from these materials are similar to naturally anisotropic, uniaxial crystals, such as calcite or quartz. These patterns provide useful information for the solution of a two-dimensional stress problem.

If a crystalline material is plastically deformed by the application of an external force, upon its removal some strain will still exist in the material, known as the 'frozen-in' strain.

A crystal having solid inclusions or precipitation particles or having small regions of 'frozen-in' strains due to plastic deformation may give rise to birefringence around the inclusions and the strained

regions when placed between the crossed nicols. Lang[119] attributed the birefringence of some diamonds to these causes.

Bond and Andrus[120] and Nye et al.[121] obtained photographs of birefringence produced by extremely small stress fields around individual edge dislocations in silicon crystals. Bond and Andrus investigated the stress distribution in the immediate neighbourhood of an edge dislocation in silicon using polarized infrared light. They obtained contours of intensity of transmitted light. Bullough[122] calculated the intensity distribution in the transmitted light through a crystal of silicon containing a single edge dislocation. He found that the intensity distribution around the dislocation obtained by Bond and Andrus from the photographs and the intensity distribution obtained by him from the theoretical considerations agreed fairly well. He also noted that an edge dislocation and a region around an inclusion both gave similar intensity contours, the only difference was that of absolute magnitude.

Lederhandler[123] investigated the stress-induced birefringence in silicon. Urosovskaya et al.[124] carried out a study of indentation figures in cesium halide crystals by the birefringence method. Examination, in transmitted polarized light, of a test sample cut along an indentation figure, showed birefringence bands along vertical slip planes. Okuda[125] et al. made studies on the birefringence patterns arising from plastic deformation in single crystals of NaCl - NaBr solid solutions.

1.8.1 Birefringence studies of stress around a hardness test indentation on a silicon carbide crystal.

Thibault et al.[40] obtained a rosette of birefringence due to transmitted plane polarized light around a Knoop indentation on a silicon carbide crystal. No attempt has been reported so far, in the literature, on analysis of the transmitted intensity. Though it is not possible to make quantitative estimation of the stress distribution around an indentation (due to the non-existence of data of the stress-optical constants of silicon carbide), the birefringence method is very useful for a qualitative estimation of the 'frozen-in' strain or the stress causing the birefringence.

1.9 Hardness test indentation and fracture of brittle materials

The indentation hardness test is regarded as a very versatile and convenient way of investigating the fracture properties of brittle materials. Small regions of very high stress intensity can be produced by indentations. The stresses generated by an indentation are predominantly shear and compressive. The tensile component of the stress field is relatively smaller but its role is important in fracture. The shear and compressive stresses give rise to conditions which are favourable to structural densification and a deformation of an irreversible kind. The latter leads to a permanent, residual impression on the surface of the crystal upon the removal of the indenter. In conventional bulk mechanical deformation tests, the conditions mentioned above do not appear. This is because a brittle fracture of the test sample is inevitable due to internal tensile

stresses which are always present and superimpose tension. The hardness test is, therefore, very useful in characterization of deformation parameters.

Observations on indentation-induced fracture have been carried out by some investigators, in materials such as tungsten carbide, magnesium oxide, glass, fused silica, sapphire and silicon carbide. The fracture studies have been aimed at understanding abrasion, grinding, erosion and tool-cutting properties.

CHAPTER II

SILICON CARBIDE - ITS PROPERTIES AND USES

2.1 The place of silicon carbide in science and industry.

Due to its remarkable oxidation resistance and hardness, together with its stability up to very high temperatures, silicon carbide has found an important place in industry as a refractory material and abrasive. Some other valuable characteristics are summarised below:

High strength, corrosion resistance, wear resistance.

High thermal stability, very slow oxidation rate at extremely high temperatures.

Chemical reactivity with halogens and with several metal oxides.

Semiconducting and rectifying properties.

Low absorption of thermal neutrons.

Low thermal expansion.

Earliest uses of silicon carbide were lapping, polishing, wire sawing of stones, abrasive blasting and similar operations using small and sharp loose grits. It was established long ago that silicon carbide would react with iron with deoxidizing effect and thus numerous metal oxides could be reduced to metal by silicon carbide additions. It reacts vigorously with halogens at elevated temperatures. Silicon tetrachloride which is produced by burning silicon carbide in chlorine, was used in World War I to produce smoke screens.

The usefulness of silicon carbide as non-linear resistors, varistors, electrical heating elements and ignition firers has been realised fairly recently. It is nowadays used to obtain fine silica for rubber reinforcement, ethylsilicate for foundry sand binder and silicon metal manufacture. A great deal of effort is being devoted to the fabrication of silicon carbide devices which can detect charged particles and record ultra violet radiations.

Silicon carbide forms a thermocouple with graphite producing a thermo e.m.f. of about 25μV/degree C. It is also used as a thermocouple tip material, having an advantage over other ceramic or oxide refractory thermocouples which undergo intergranular cracking and corrosion in gaseous media and various molten metals and slags. Cold cathodes of silicon carbide are extensively used in electron guns. These have the advantage of being highly stable, having wide energy gap and possessing large electron mobility. Silicon carbide is stable when exposed to radiations from an atomic reactor. Both carbon and silicon have low thermal neutron absorption cross-section. These properties have made silicon carbide an outstanding contributor for dispersing the fission products of uranium carbide in silicon carbide in the shape of microspheres.

Grown p-n junctions are used as a detector of phonons or nuclear particles. The operation depends upon the formation and

collection of electron-hole pairs produced by the passage of the photon or particle through the detector. Another important feature of such junctions is that they emit light when a current is passed.

For refractory applications, such as heating elements of SiC, thermocouple protectors, rocket motor nozzles and combustion chambers, rotors of gas turbines and power generators etc., silicon carbide is fabricated by reaction-sintering with the addition of a small percentage of one or more materials, e.g. MgO, CaO, SiO_2 or Al_2O_3. The bonded materials have good strength, oxidation resistance and heat conductivity.

2.2 General physical properties of silicon carbide crystals

Silicon carbide is a very hard crystalline solid. Its hardness is placed at number 9 in Mohs scale of hardness, between diamond (10) and topaz (8). It is claimed that some types of silicon carbide will scratch certain varieties of diamond. Eagle et al.[131] reports the bend strength of silicon carbide crystals at room temperature as 25,000 psi.

Silicon carbide has a high refractive index n_o (for the ordinary ray) = 2.647 and n_e (for the extraordinary) = 2.69, for the sodium line $\lambda = 5890\ A^o$. When shiny, transparent crystals are viewed between the crossed polarizers all the crystals show some degree of birefringence which could be due to the result of the presence of a pile of dislocations, precipitates, fracture or

plastic deformation of the crystal.

Taylor[132] found the thermal conductivity of SiC to be 0.244 cal/cm ^{o}C at 200^{o}C and 0.101 cal/cm^{o}C at 1000^{o}C. The coefficient of linear expansion has been reported[133] as $4 \times 10^{-6}\ ^{o}C^{-1}$ as the mean value between 0^{o} and 1000^{o}C. Silicon carbide has a remarkable high thermal stability. It has not got any congruent melting point and dissociates into carbon and silicon vapours, above 2,000^{o}C. Knippenberg[134] has estimated the vapour pressure of the system SiC +C as 1 atm at 2800^{o}C. Drowart et al[135] found the vapour pressure of different gaseous products (Si, SiC_2 and Si_2C) in equilibrium with SiC + C system as 1 atm at 2850^{o}C.

Silicon carbide is one of the few wide band gap semiconductors and due to its semiconducting properties the electrical properties have been extensively investigated by several investigators. Silicon carbide is a non-conductor when pure and has a resistivity of the order of 10^3 - 10^5 ohm cms. It was generally believed that green silicon carbide crystals were semiconducting due to the excess of electrons (n-type) whereas black crystals were due to the excess of holes (p-type). But Kendall[136] has shown that the black crystals could be of p- or n- type. According to him silicon carbide should be a semiconductor due to the presence of non-stoichiometric amounts of Si or C or to the presence of impurities such as aluminium, boron or nitrogen. Kendall could not make precise measurements to establish whether they were p- or n-type except by simple investigation of the sign of the thermoelectric

coefficient at room temperature. Lely[137] found that the introduction of nitrogen results in the formation of n-type with the donor level lying 0.10 eV below the conduction band. Van Daal et al.[138] reported crystals containing aluminium as an impurity as p-type with acceptor level 0.30 eV above the valence band. The results of the temperature dependence of the concentration of free carriers in (n, p) silicon carbide crystals show that below 500°C the process of injected carrier capture by donor and acceptor centres is prominent; these centres act as electron and hole traps. When the crystal is heated, release occurs, first of electrons from electron traps (or holes from hole traps) which make up the deficiency of carriers in the conduction (or valence band). The onset of intrinsic conductivity begins at 500°C. Some useful information regarding semiconducting characteristics has been gathered from the work of Smith[139], Busch et al.[140], Racette[141] and Choyke et al.[142] The Hall mobility of silicon carbide varies with temperature somewhat differently from the mobility of other semiconductors. The maximum value of 10 $cm^2/V.sec$ at 200°K, for n-type, falls to nearly zero at 90°K; for p-type the maximum mobility has a value of 70 $cm^2/V.sec$ at 200°K and 20 $cm^2/V.sec$ at 1000°K. Choyke expressed the fundamental absorption edge of silicon carbide in terms of phonon emission and absorption. According to him, the transitions corresponding to the band edge are indirect and involve the emission and absorption of phonens of energy 0.09 eV. The calculated value of the forbidden energy is found to be approximately 2.86 eV.

2.2.1 Chemical properties.

Silicon carbide is unattacked by all acids except orthophosphoric acid at 215°C. It reacts with Cu, Ni, Fe and Mn oxides, at temperatures above 1000°C, to give metal silicides and is dissolved or decomposed by fused alkali hydroxides, carbonates and sulphates. Silicon carbide has a high chemical reactivity with halogens. In chlorine it begins to decompose slowly at 600° and completely decomposes at 1200°C giving CCl_4 and $SiCl_4$. Nitrogen reacts at 1400°C with it giving silicon nitrides and C. Hydrogen etching at 1700°C has been reported. It is also attacked by oxygen at high temperatures but up to about 1000°C the oxidation is rather slow. Lea,[143] Nakatogawa,[144] Lambertson[145] and Adamsky[146] investigated oxidation of silicon carbide over a large range of temperatures. Lambertson's results indicate that oxidation in the temperature range from 950° to 1600°C is controlled by the diffusion of some species through SiO_2 film formed over the surface. The diffusion species is either oxygen diffusing into SiC-SiO_2 interface or CO diffusing outward into atmosphere. Above 1650°C oxidation becomes reaction-controlled with the reaction between SiC and SiO_2 as the rate-controlling step.

2.3 Polytypism in silicon carbide.

Silicon carbide appears in a large number of closely related crystal forms. When the morphology of silicon carbide was first investigated, Baumhauer[147] discovered the existence of three types which were arbitrarily named I, II and III in the order of discovery. Ott[148] determined the structures of these types and found a 15 layer rhombo-

hedral, a 6 layer hexagonal and a 4 layer hexagonal form respectively. He also found a cubic form called type IV and 51 layer rhombohedral form known as type V. Thibault[149] regarded type IV as a true modification and termed it as β-silicon carbide. Fig. 2. 1 shows some common polytypes of silicon carbide.

In the literature over 45 different structures which have been identified by X-ray investigations have been reported. All modifications are composed of identical layers and differ only in arrangement of these layers. Each type is identified by the number of layers necessary for the arrangement to repeat itself. The lattice parameters of different polytypes are described as[150]

$$a_o = b_o = 3.078\ ^{o}A$$

$$c_o = 2.518 \times n$$

where n is the number in the hexagonal unit cell. For instance α-SiC rhombohedral structures can also be described with a hexagonal cell, the number of particles in the hexagonal unit cell will be then three times the number in the rhombohedral cell. (Fig. 2. 2).

2.4 Atomic positions in type I (15 R) and type II (6 H) crystals (Wyckoff)[151]

α-SiC (15 R): (Hexagonal-rhombohedral)

Lattice parameters

$a_o = 12.69\ A^{o}$; $\alpha = 13^{o}55'$ (rhombohedral), n = 5

$a_o = 3.073\ A^{o}$; $c_o = 37.70\ A^{o}$ (hexagonal) n = 15

Atomic positions

$$00\ U;\ \frac{1}{3}, \frac{2}{3}, \frac{1}{3} + U;\ \frac{2}{3}, \frac{1}{3}, \frac{2}{3} + U$$

$$U_{carbon} = 0,\ 0.133,\ 0.4,\ 0.6,\ 0.86$$

$$U_{(silicon)_n} = (carbon)_n + 0.5$$

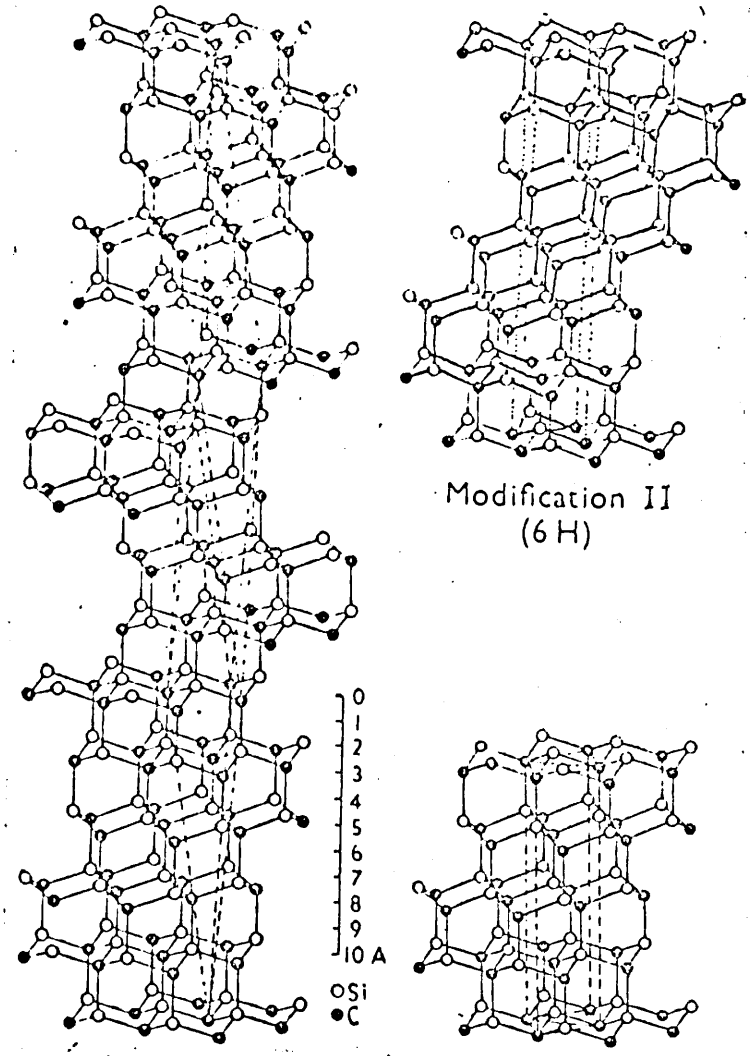

Modification II
(6 H)

Modification I
(15 R)

Modification III
(4 H)

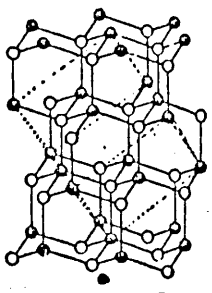

β – Si C
Cubic

Fig. 2.1.

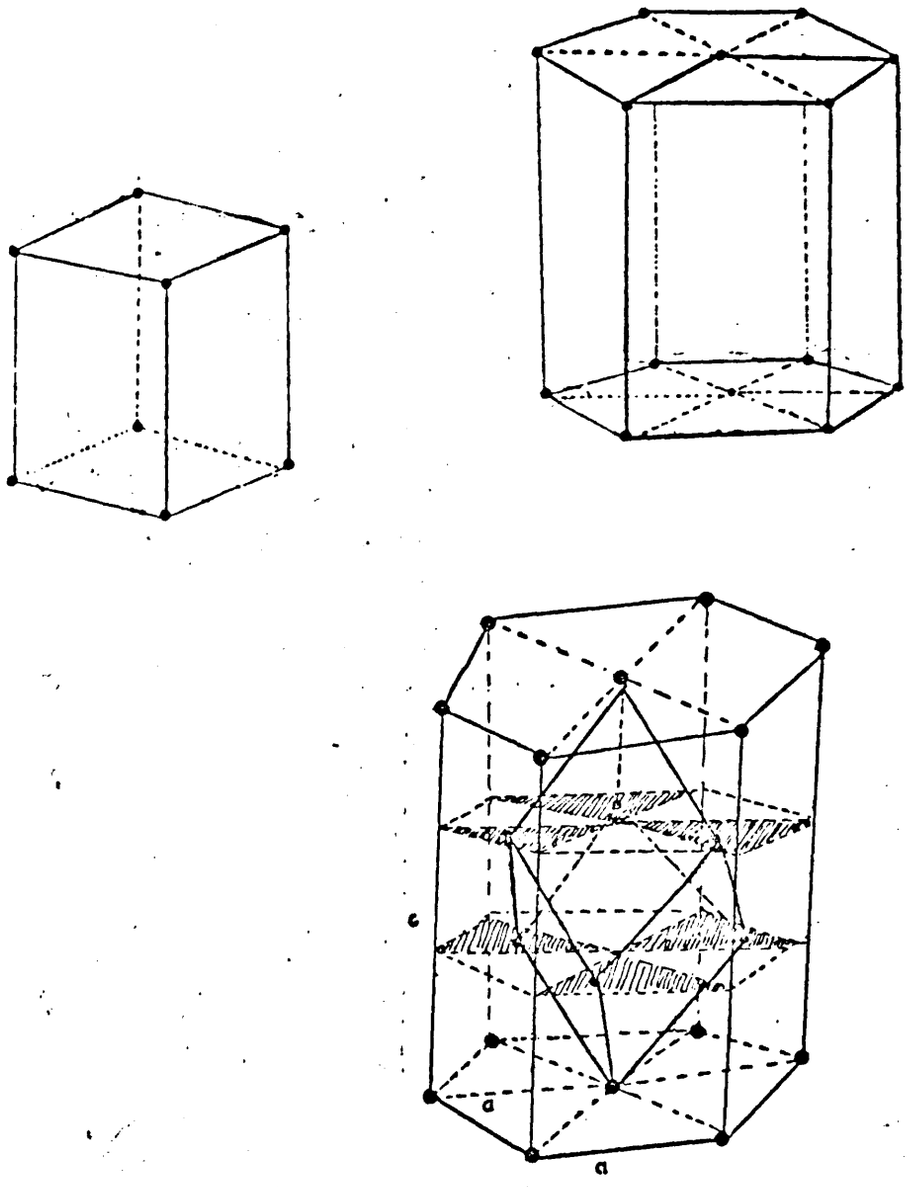

Fig. 2.2 . Primitive cells of SiC.

α- SiC (6H) or type II :

$$a_o = 3.073\ A^o; \quad c_o = 15.08\ A^o$$

The position of its 6 molecules are on tri gonal axes:

$$0\ 0\ U;\ 0,\ U + \frac{1}{2}$$

$$\frac{1}{3},\ \frac{2}{3},\ V;\ \frac{2}{3},\ \frac{1}{3},\ V + 1/2$$

$$U_{(carbon)} = 0\ ; \quad V_{(carbon)} = 0.166,\ 0.833$$

$$U_{(silicon)} = 0.125; \quad V_{(silicon)} = 0.291,\ 0.958$$

2.5 Nature of silicon-carbide

The electronic configuration of silicon and carbon atoms is given by ($1s^2\ 2s^2\ 2p^6\ 3s^2\ 3p^2$) and ($1s^2\ 2s^2\ 2p^2$) respectively.

The Si-C binding can be of two types.

2.5.1 Ionic or electrovalent binding

Both C and Si have four valence electrons in the outermost shells. The C atom, being more electronegative than the Si, is in a position to accept 1 electron fromthe 4 Si atoms bound to it tetrahedrally forming a C^{-4} ion. Each Si atom in turn donates 4 electrons, 1 to each C, therefore, forming a Si^{+4} ion. An ionic bond is formed due to the electrostatic attraction between these ions.

According to this model the Si-C bond length is 1.79 and the C atom is about 3.7 times bigger than the Si atom.

2.5.2 Neutral or covalent bond

If in the tetrahedral bonding of Si and C two electrons from the C atom share the bond with two electrons from Si atom with antiparallel spins, they would complete the stable orbit in their outermost shell. Such a structure where the four bonds are directed to their neighbours have neutral or covalent bond.

The Si-C distance, in this case, is 1.94 and the Si atom is about 1.5 times as big as the C atom.

There are grounds to believe that silicon carbide is essentially a neutral or covalent compound.

Due to a small electronegativity difference between the silicon and the carbon atoms, a small positive charge existing on silicon atoms results in an ionic contribution of about 10% to the bond, as estimated from Pauling's empirical formula (Pauling[152]). This ionic contribution is also deduced from the shift of K_a doublet in the X-ray emission spectra of Si in SiC. This shift depends on the charge on the Si atom, (Faessler[153]), for a number of Si compounds with dissimilar bond character. Like all other crystals which partly have polar binding, SiC shows a maximum in the infrared reflectivity. In the model proposed by Hoóge,[154] the formula relating the refractive index with the dielectric constant of the ionic crystal contains a factor which depends upon the deviation from the perfect ionic model. It has been shown that this factor for SiC is in agreement with that for AB compounds if estimation of positive charge on the atom is made from Pauling's formula.

CHAPTER III

EXPERIMENTAL TECHNIQUES

3.1 Multiple-beam Interferometry.

This technique was developed by Tolansky[155] in 1943 and has received wide recognition for its applications to numerous aspects of metallurgy, metal physics, mirror and surface finishes, hardness testing and so on. Its great power lies in the fact that it reveals quite subtle changes in the height-depth direction.

Interference fringes arise from a system consisting of two thin glass plates, coated with a high-reflecting film by vacuum deposition. For microtopography of an object, one of the glass plates is replaced by the object. Such a system can either be a parallel plate or a wedge shaped, an extremely thin air film separating them.

According to Tolansky, the following conditions should be fulfilled for the production of sharp fringes.

1. The surfaces in contact must be coated with a highly reflecting film of minimum absorption.
2. Thin films should contour the surface exactly.
3. Monochromatic light should be used.
4. The surfaces must be separated by only a few wave-lengths of light.
5. A parallel beam within a tolerance of (1^{o} - 3^{o}) should be used.
6. The light should be normal to the reflecting surface.

3. 2 Fringes of Equal Chromatic Order (F. E. C. O.)

These fringes were first described by Tolansky in 1945. If a section of multiple-beam interference fringes, produced by a monochromatic light, from a wedge system is projected on the slit of a spectrograph, (Fig.3.1), and then this light source is replaced by a white light source, the spectrum in the focal plane of the spectrograph consists of narrow bright fringes separated by much darker intervals. Such fringes were called fringes of equal chromatic order by Tolansky.(155)

It has been shown (Tolansky) that over any section of tne wedge both 't' (the separation between the plates of the wedge) and ' λ ' (wave-length) are variables and fringes are formed at constant t/λ and as the fringes cover a wavelength range, they are chromatic. Assuming normal incidence, for an air film, the fringe order is given by

$$n = 2t/\lambda = 2vt \text{ ; where } v = \text{wave number.}$$

Differentiating

$$\delta n = 2 \delta v \cdot t.$$

For successive orders $dn = 1$, therefore,

$$t = 1/2 \delta v$$

For any given value of t, the fringes are equally spaced and the spacing is independent of the angle between the surfaces. These fringes are related to the topography over the selected section. The direction of the curvature of fringes shows whether the surface is convex (hill) or concave (valley). A convex surface bows the fringes convex to the violet and a concave surface bows them concave to the violet. Tolansky also shows how to evaluate the height or depth of any distortion, if one of the surfaces is not very smooth or contains surface features, using these fringes.

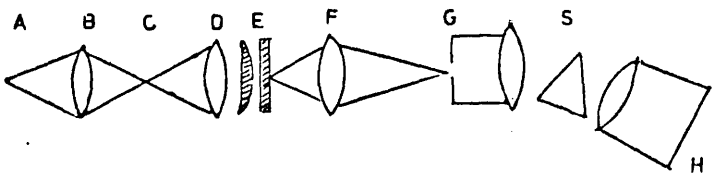

Fig. 3.1. Optical arrangement for F.E.C.O.

A = White light source

C = Circular aperture

E = Interferometer system

G = Slit of a prism spectrograph S

H = Photographic plate on which the fringes appear

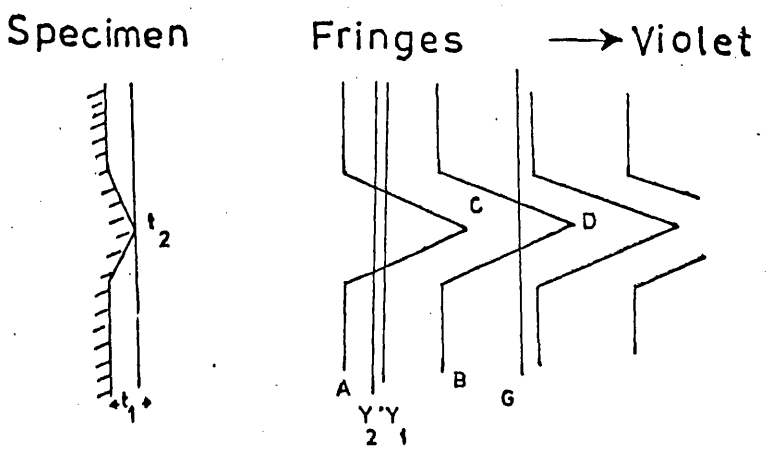

(White light spectrum, Y_2, Y_1 .... G...., superimposed on F.E.C.O. which are convex towards violet)

3.3. The Indentation instruments (Hardness Testers).

3.3.1 Low load (up to 200 gm) indentations.

These were made with standard diamond pyramid, spherical and double cone indenters, mounted on the objective of a Vickers Projection Microscope, in conjunction with a commercial hardness tester made by Cooke, Troughton and Sims. Fig.3.2 shows the apparatus set up on the Vickers microscope. The different letters in the figure denote the following parts of the apparatus:

A ... Coarse motion head

B... Fine motion head

C... Diamond indenter

D... Socket and support block for load centre indicator

E... Rotation stop to load centre indicator

F... Base plate

G... Securing screws

H... Counter weight

I... Vertical pillar

J... Pivot axle bearing with adjusting screws

K... Pocket for auxiliary counter-weights

L... Auxiliary counter weights

M... Beam

N... Lamp housing with red glass window

O... Horizontal bar support to indicator pin

P... Load position indicator

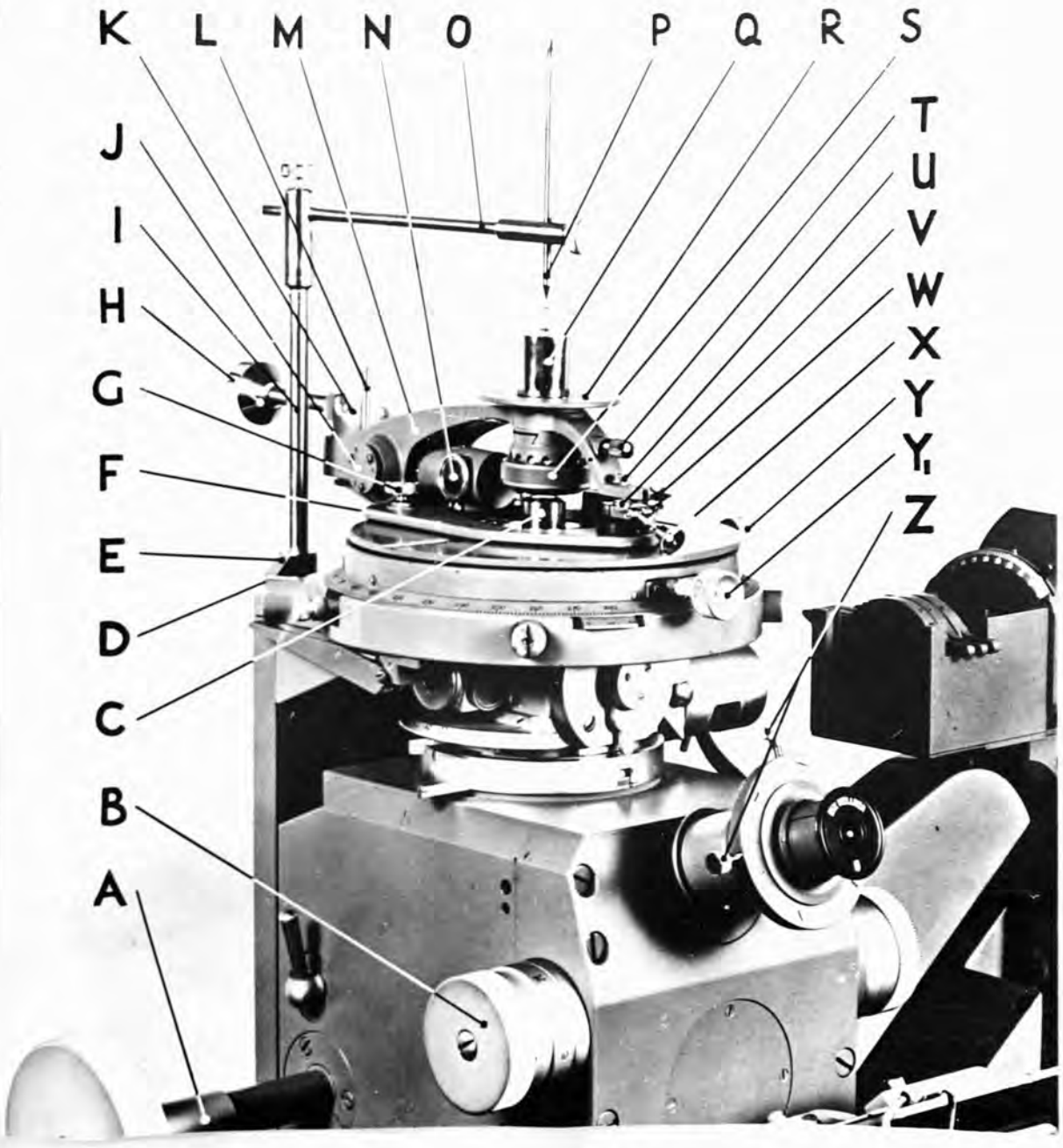

Fig. 3.2. COOKE MICRO-HARDNESS TESTER
Set up on the Vickers Microscope.

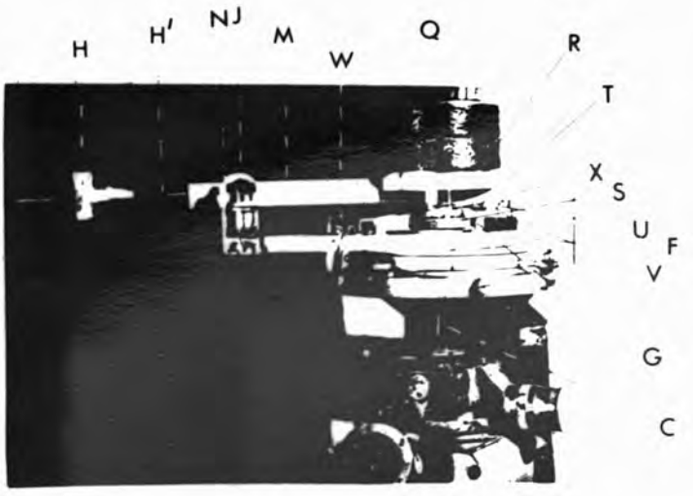

Fig.3.3. Hardness tester for macro - indentations.

Q... Chemical balance weights as 'load'

R... Load plate

S... Collet chuck securing specimen

T... Clamp for S

U... Beam contact tip

V... Base plate contact anvil

W... Low voltage supply

X... Hinged screw lock

Y... Stage cross traverse screws

Z... Stage longitudinal traverse screws

3.3.2 High load (up to 5 kg) indentations

The commercial hardness tester described in the foregoing article was replaced by a more rigid tester which was made in the departmental workshop. This instrument is capable of taking loads up to 7 kg. and is almost as sensitive as the other one. Fig. 3.3 is the photograph of the tester shown mounted on the Vickers projection microscope. The letters stand for the same parts of the tester as in Fig. 3.2.

3.4 Replica techniques

Surface replication was employed to examine the crystals by an A.E.I. EM6 electron microscope. Two types of replicas were prepared:

(1) Plastic replicas

(2) Two-step plastic/carbon replicas.

The following plastic solutions were used for type (1) replicas:

(a) Formvar, polyvinyl formal or polyvinyl acetal resin 1.2% solution in dioxane.

(b) Collodion, pyroxlin, cellulose nitrate - 4% solution in 3 parts ethyl ether, 1 part ethanol.

It was found that the resolution, using this kind of replicas, was not better than 200 A^{o} and the contrast was poor.

The two-step replica method was mainly used for the study of the indented surfaces. The method of preparation is a modification of that employed by the manufacturers of the Bioden plastic film acetyl cellulose, Oken-Shoji Co. Ltd., Tokyo, Japan.

The procedure for preparing replicas by this method consists of the following stages, in order.

(i) Preparation of the surface. Crystals are thoroughly washed first with a detergent and then with hydrogen peroxide or cleaned ultrasonically using acetone.

(ii) The acetyl cellulose film of Bioden of 0.034 mm thickness is cut into a number of pieces a little larger in size than the specimen surface. A piece is lowered into a solvent e. g. methyl acetate, for just a second, the film is then quickly laid over the specimen and pressed gently on it so that there are no air bubbles underneath. After allowing the plastic to harden for a few minutes, in a dust-free atmosphere, it is stripped from the specimen surface. The replica so formed is known as the first-step replica.

(iii) The first-step replica is likely to curl. It is, therefore, placed between two clean glass slides and tightened slightly with paper clips and kept in an oven, at 80°C, for half an hour. This piece is then transferred on to another slide with the reproduced surface facing up and placed in the bell jar of evaporating unit, Edwards coating unit type 3. The bell jar is evacuated to a low pressure (10^{-4} mm Hg).

(iv) The second-step replica is now formed by depositing a thin carbon film. This is done by passing a heavy current of 50 amps through the carbon electrodes (one blunt, the other sharp to give a point source) located inside the bell jar. The replicas are generally shadowed with platinum, silver or gold. The shadowing has the advantages that

- it improves the contrast,
- the shape and dimensions of a feature can be determined.

The shadowing material can either be put in a separate small tungsten boat which is connected across another pair of electrodes and evaporated by passing a heavy current in the tungsten filament or it can be in the form of a cylindrical core in one of the two carbon electrodes. Use of the latter eliminates double evaporation. The angle of shadowing is varied according to the type of structure under examination; for general purposes it is good enough

to have an angle of 30^{o}.

In order to make a rough estimate of the thickness of the (carbon + platinum) film, a drop of silicone oil is placed on the glass slide having the first-step replica before the commencement of the stage (iii) described above. The film will not be deposited on the oil drop whereas the area adjoining it is slightly tinted. When the tint becomes greyish, the carbon film is about 200^{o}A and the evaporation is stopped.

(iv) The two-step replica so formed is removed from the evaporating unit. Paraffin wax is melted in a beaker and a glass slide dipped in it to form a wax layer of 0.1 to 0.3 mm. Before it resolidifies, the replica is placed on the thin layer with carbon coated face of the replica in contact with it. Wax prevents the carbon film from disintegrating during its removal from the plastic film which is done by dissolving the latter in methyl acetate.

(v) Removal of the plastic film. The replica attached to the glass slide through wax is now soaked in methyl acetate, at room temperature, in a petri dish. The plastic film begins to swell in 3-5 minutes. The dish is placed in the oven set at 50^{o}C and the wax begins to dissolve, as does the plastic film which in fact disappears in a few minutes. The carbon replica comes off the glass slide and floats in the solvent.

(vi) The replica is transferred into another dish containing fresh methyl acetate at room temperature. The dish is placed inside the oven, which is already at 50°C. The temperature of the solvent is raised to about 45°C in 15-20 minutes. An easy way of raising the temperature is to put the dish in a slightly bigger dish half-filled with water and return it to the oven.

(vii) The replica is washed in the solvent, for five or six times or until it is free from wax, as described above. It is finally collected on to a copper grid (previously washed in alcohol and thoroughly dried). The replica is now ready for an examination in the electron microscope. Sometimes a replica may be seen folded whilst in the solvent. It can be unfolded by transferring it into a dish containing a mixture of 60% acetone and 40% distilled water. It extends flat due to surface tension. It is cleaned in distilled water and collected on to a copper grid.

3.5 Ion-bombardment or ion-thinning technique

The limiting thickness for the transmission electron-microscopy depends largely upon the atomic number of the specimen, decreasing from 2000°A for aluminium to approximately 500°A for uranium (Thomas [156]). Heidenreich [157] was the first to examine thin metallic foils directly in an electron microscope. Later on, most of the attempts to prepare thin films from bulk

materials consisted of two operations:

1) to thin the bulk material down to a few thousandths of an inch by mechanical grinding.

2) to thin it down further by

a) chemical polishing, or

b) scanning jet machining, or

c) spark-erosion, or

d) abrasion with fine particles (sand-blasting).

The exploitation of 'glow discharge' for sputtering has been quite common in recent years. Hietel and Meyerhoff[158] produced holes in silicon crystals, Shimomura et al.[159] made thin sections in NiO. Drum,[160] using a horizontal discharge tube, was able to get extremely small electron transmission sections in silicon carbide and sapphire. As a matter of fact there are some commercial ion-beam thinners available in the market, such as the ion micro-milling instrument 1MM1 developed by Commonwealth Scientific, and the ion-etcher from AEI. The ion-thinner assembled by the author for making thin sections in silicon carbide crystals, for transmission electron microscopy work, has the following advantages over the commercial ones:

1. It is simple and very economical. The specimen holder and electrodes, for instance, cost only a few pence, whereas these parts cost around £15 for a commercial one. These also need

replacements after every 200 hours or so, of continuous operation.

2. Ion-thinning is faster due to the use of a special electrode configuration and application of a transverse magnetic field exploiting ion-bombardment of high concentration.

3. No specimen holder is required. The discharge tube being vertical, a sample can be simply placed on the cathode.

3.5.1 The ion-thinner. (Fig. 3.4.)

The discharge chamber of the ion-thinner is schematically shown in Fig.3.5. Cathode (C) is machined from high purity stainless steel. It is in the form of a cylindrical cap, with edges of one end rounded off and having a small cavity to accommodate a sample. This is slipped on to a vertical copper tube which has a concentric tube inside it. These tubes are hard-soldered together in such a way that they make a water-cooling unit, with a water inlet and outlet (not shown), for the cathode. Anode (A) is a planar aluminium disc of the same diameter as C, and is attached to an aluminium rod (L). The anode can be moved in the cathode-anode axial direction. The discharge tube (D) is a quick fit Q.V.F. of 2" diameter. This sort of discharge chamber is very convenient as the specimen can be introduced and electrodes moved quite easily. Moreover, since the cathode is not completely enclosed inside the chamber, the water connections (inlet and outlet) to the cooling system need not be introduced into it. The discharge chamber is sealed by a teflon insulation clamp and a teflon plate, with a

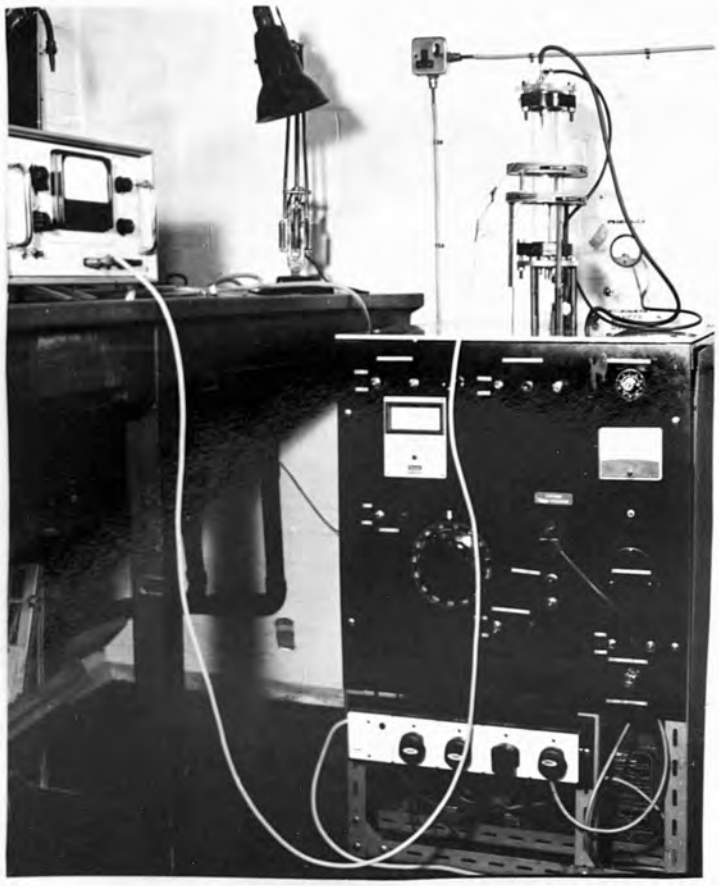

Fig.3.4. Ion-beam Thinner

recess for an O-ring, at the anode end, and aluminium clamps and 1/4" thick steel plate which also has an O-ring at the cathode end. The metallic end plate extends the effective cathode surface electrically and therefore prevents undesirable sharp field gradients at the cathode.

A rotary pump (not shown) is used to pump down to glow discharge pressures. Clean air or argon is fed through a port which is a needle valve adjusted to maintain a constant pressure inside the chamber. The cathode-anode voltage drop could be varied between 0-5 kv at 30 mA. A low impedance filtered D.C. power supply was assembled. The circuitry of the power supply is shown in Fig.3.5. The current was measured as the voltage drop across a standard 100 ohm resistance (R).

In order to confine the glow discharge, rather than letting it spread it in the entire chamber, a quartz tube (T) of diameter a little larger than that of the cathode or anode and length equal to the inside length of the chamber was held vertical and concentric to the main chamber by means of teflon rings at each end. A pair of Helmholtz coils, outside and concentric to the main discharge chamber, connected to a D.C. supply (10-15 amps.), were used to produce a 'pinching effect' on the discharge between the electrodes

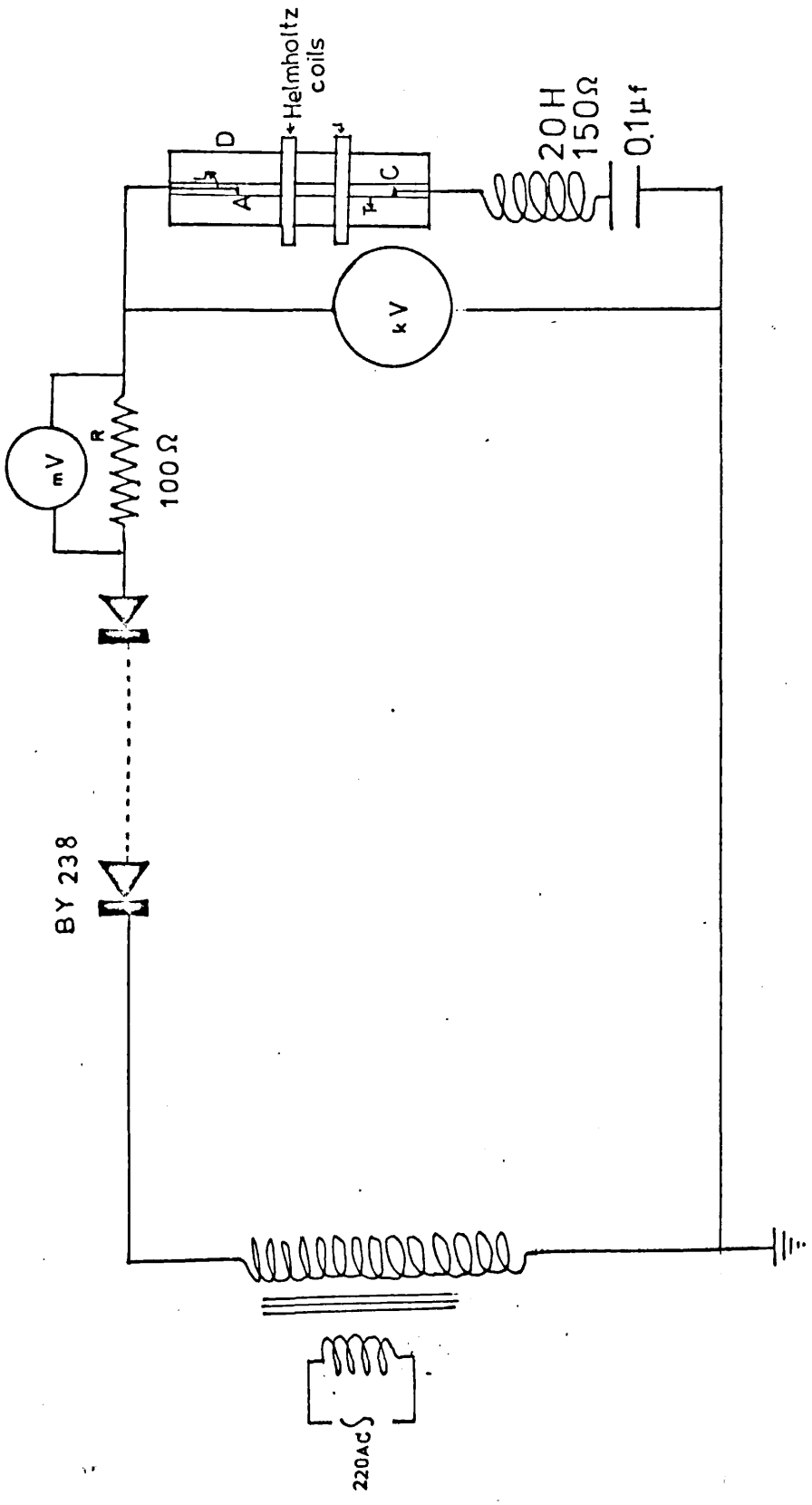

Fig. 3.5.

3.5.2 Preparation of samples for transmission electron microscopy

To produce thin sections in silicon carbide crystals, samples less than 1/100th of an inch were required. Thick samples can be mechanically ground to such values but due to the non-availability of a diamond abrasive wheel, some of the thinnest possible (as grown) crystals were acquired (thickness $\simeq 100\mu$).

The specimen to be thinned was placed in the cavity on the cathode.

The electrodes, with spacing d = 15 cms (this was found to be the optimum distance for best ion-thinning results), were enclosed inside the quartz tube and then sealed in the main discharge chamber. The gas leak was closed and the valve connecting the rotary pump to the chamber was opened. The discharge chamber was pumped down to a pressure $\sim 10^{-2}$ Torr, as indicated by the Pirani gauge. Argon was admitted through the gas leak valve which was regulated to keep an equilibrium pressure. After the pressure was steady for half-an-hour or so a high d.c. voltage was applied across the electrodes. The voltage was smoothly variable from 0 to 5 kv.

A glow discharge appeared at about 1 kv. Occasional arcing was noticed in the beginning which was probably caused by some dust particles remaining on the specimen. The discharge becomes steady in a few minutes. A longitudinal magnetic field of 300 to 400 oersteds intensity was applied to the discharge by means of the Helmholtz coils.

It was possible to produce transparent regions, in the range of 1000-3000 ^{o}A, in the form of extremely narrow perforations. Around these perforations were areas large enough to produce electron diffraction patterns.

3.6 Etching technique

Etching is a widely employed technique for investigations such as study of the structures of dislocations and determination of orientation of crystals.

The etch method for revealing dislocations is based on the assumption that there is a one to one correspondence between the pits formed by etching and the emergence of dislocation lines on the surface. It is supposed that atoms and molecules situated along dislocation lines are attacked preferentially by the etchants.

Cabrera and others[161] considered the theoretical conditions for the formation of the etch pits at dislocations. They established that stress field around a dislocation is responsible for increased activity. According to Wyon et al.[162], some impurity segregations or 'Cottrell atmosphere', in metals, are necessary before dislocations are etched. The presence of an impurity atmosphere locally increases the solubility and hence increases the etching rate. Tyapunina et al.,[164] however, showed that the presence of impurities reverses the effect of preferred etching of a crystal. Horn[172] was first to show that etch pits are formed primarily at the intersection of screw dislocations. His etching experiments, on silicon carbide crystals having growth spirals on the basal plane, showed that growth spirals are rapidly etched away and a hexagonal pit is formed which grows progressively

bigger until a hole is produced. Etching studies on some other crystals having growth spirals such as beryl, topaz, CdI, AgCl, AgBr, thynol and salol showed that hexagonal pits were formed on growth spirals. The investigations carried out by Frank,[165] Forty,[166] Vogel[167], Pfan[168], Gilman,[169] Patel[171] and others[170,173] have substantiated a connection between the etch pits and the emergence of dislocations. One to one correspondence between them has been, however, challenged by some investigators.

3.6.1 Classification of etching process

Etching of the crystalline solids is carried out using one of the following methods.

1. Chemical - the material is reacted with a molten salt, at its melting point, in a platinum or gold crucible. The salt chosen is the one which does not leave any insoluble layer on the crystal.

2. Electrolytic - the dissolution is carried out by the flow of current in a suitable electrolyte.

3. Cathodic bombardment - the material is placed on the cathode or near it, in an ion-bombardment apparatus.

4. Thermal treatment in vacuum or in an inert gas - etching is carried out at a high temperature, usually to 2/3rds of the melting point, by vapourization.

3.6.2 Etching of silicon carbide crystals

Faust Jr.[174], has reviewed the etching processes employed for silicon carbide etching. In this work the chemical etch method

was used. Borax and a mixture of Na_2CO_3 and K_2CO_3 (in the ratio of 1:3) were found to be satisfactory etchants. The temperature of reactions were 1000 C^o and 700 C^o, respectively.

3.6.3 Thermal treatment of silicon carbide crystals, (annealing at high temperatures)

The departmental Plasma Torch was used for annealing the crystals. The Plasma Torch consisted essentially of a 6MHz radio frequency generator with a coil in its tank. A quartz tube was placed vertical and concentric to the coil and had an outlet for argon. Pure argon at 1 at. was imposed into the tube with a very low or no gas velocity. An intense hot flame could be produced by passing rf power ($\simeq$ 3kw) through the coil. The hot zone had a volume of 0.1 ℓ. The temperature at various points, in the flame, could be measured by disappearing filament pyrometer and was found to vary from 1500 to 3500 C^o in the vertical direction. Crystals to be heated were placed in a carbon crucible machined from special electrographite. A travelling microscope stand was used for lowering the crucible into the flame. Heat treatment was stopped by cutting off the power input to the generator while argon was still left flowing for a few minutes. In order to avoid thermal shock, the crucible was very slowly withdrawn from the flame, until it was a few inches above it, before the power supply was switched off.

3.7 Birefringence experiment

The Vickers projection microscope was the main apparatus used in the study of birefringence patterns.

The indented specimen was placed in a holder attached to the movable stage of the microscope. This holder could be rotated about a vertical axis. The specimen, therefore, could be held at any desired angle with respect to the incident light. The source of light was a mercury lamp with a green filter. The light was polarized by a Polaroid type polarizer. The polarized light was transmitted through the specimen and collected by the objective of the microscope. It then passed through a crossed polarizer and the eye-piece of the microscope formed the final image.

The specimens chosen for this investigation were those which were free from impurities, colourless and thin (thickness approximately 200 microns). The loads used for making indentations were above 500 g .

CHAPTER IV

STRESS FIELDS BENEATH AN INDENTER

4.1 Stress distribution due to indentation

In dealing with the problems of deformation of two elastic bodies in contact, solutions have been successfully obtained by the application of Hertz contact model [175] [e.g. Willis [176]] and Hankel transform method [e.g. Elliott [177]]. In the Hertz model two curved bodies are characterised by two principal radii of curvature near the point of contact. As the area of contact is generally very small compared to the radius of curvature, one of the bodies can be replaced by an elastic semi-infinite plane. In the latter method the solution is obtained in terms of two harmonic functions. Several other independent solutions have been found, such as by Westergaard [178], Sen [179], Green and Zerna [180] and Galin [181]. These deal with two-dimensional problems of plane contact. Very little work has been reported for elastic stress distribution in three dimensions. Recently, Chen [182] and Conway et al. [183] have presented analytical results of maximum shear stress distribution in some hexagonal single crystals indented with rigid ball spheres. They used Hamilton and Goodman [186] closed-form solutions for contact problems in three dimensions. It has been shown that the maximum shear stress distribution, beneath an indenter, in an anisotropic crystal, is different from that in the isotropic.

We have computed the stress distribution under a spherical indenter, in the interior of the half-space of an anisotropic hexagonal body (silicon carbide crystal), using the Hertzian contact model and following the analyses made by Chen and Hamilton. (See Appendix I).

4.2 Hertzian contact

Stress distribution in cylindrical polar coordinates under the influence of a symmetric normal load:

The components of stress ($\sigma_{rr}, \ldots \sigma_{r\theta}$) and displacement ($U_r$, U_θ , U_z) are related to each other by the following relations:

$$\sigma_{rr} = C_{11} \frac{\delta U_r}{\delta r} + C_{12} \frac{\delta U_\theta}{r \delta \theta} + C_{13} \frac{\delta U_z}{\delta z} \qquad (4.1)$$

$$\sigma_{\theta\theta} = C_{12} \frac{\delta U_r}{\delta r} + C_{11} \frac{\delta U_\theta}{r \delta \theta} + C_{13} \frac{\delta U_z}{\delta z}$$

$$\sigma_{zz} = C_{13} \left(\frac{\delta U_r}{\delta r} + \frac{\delta U_\theta}{r \delta \theta} \right) + C_{33} \frac{\delta U_z}{\delta z}$$

$$\sigma_{\theta z} = C_{44} \left(\frac{\delta U_\theta}{\delta z} + \frac{\delta U_z}{r \delta \theta} \right)$$

$$\sigma_{r\theta} = \tfrac{1}{2} (C_{11} - C_{12}) \left(\frac{\delta U_r}{r \delta \theta} + \frac{\delta U_\theta}{\delta r} \right)$$

$C_{ij's}$ are called elastic constants. (See Fig. 4.1 for illustration of σ_{rr} etc.).

The equations of equilibrium are

$$\frac{\delta \sigma_{rr}}{\delta r} + \frac{\delta \sigma_{r\theta}}{r \delta \theta} + \frac{\delta \sigma_{rz}}{\delta z} = 0 \qquad (4.2)$$

$$\frac{\delta \sigma_{r\theta}}{\delta r} + \frac{\delta \sigma_{\theta\theta}}{r \delta \theta} + \frac{\delta \sigma_{\theta z}}{\delta z} = 0$$

$$\frac{\delta \sigma_{rz}}{\delta r} + \frac{\delta \sigma_{\theta z}}{r \delta \theta} + \frac{\delta \sigma_{zz}}{\delta z} = 0$$

Substituting equations (4.1) in the above equations, we get

$$C_{11} \frac{\delta^2 U_r}{\delta r^2} + \tfrac{1}{2} (C_{11} - C_{12}) \frac{\delta^2 U_r}{r^2 \delta \theta^2} + C_{44} \frac{\delta^2 U_r}{\delta z^2}$$

$$+ \frac{\delta}{\delta r} \left[\tfrac{1}{2} (C_{11} + C_{12}) \frac{\delta U_\theta}{r \delta \theta} + (C_{13} + C_{44}) \frac{\delta U_z}{\delta z} \right] = 0 \qquad (4.3)$$

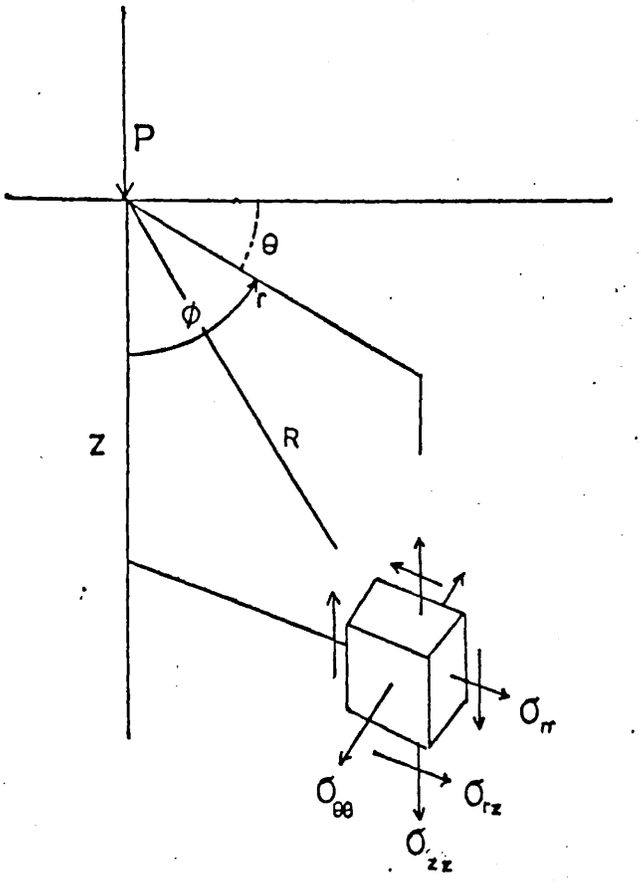

Fig. 4.1 Coordinate system for axially symmetric point loading.

$$\tfrac{1}{2}(C_{11}-C_{12})\frac{\delta^2 U_\theta}{\delta r^2} + C_{11}\frac{\delta^2 U_\theta}{r^2\,\delta\theta^2} + C_{44}\frac{\delta^2 U_\theta}{\delta z^2}$$

$$+ \frac{\delta}{r\delta\theta}\left[\tfrac{1}{2}(C_{11}+C_{12})\frac{\delta U_r}{\delta r} + (C_{13}+C_{44})\frac{\delta U_z}{\delta z}\right] = 0. \quad (4.4)$$

$$C_{44}\left(\frac{\delta^2 U_z}{\delta r^2} \quad \frac{\delta^2 U_z}{\delta r^2}\right) + C_{33}\frac{\delta^2 U_z}{\delta z^2} + (C_{13}+C_{44})\frac{\delta}{\delta z}$$

$$\left(\frac{\delta U_r}{\delta r} + \frac{\delta U_\theta}{r\delta\theta}\right) = 0. \quad (4.5)$$

The solution of these equations can be of the form

$$U_r = \frac{\delta\phi}{\delta r}, \quad U_\theta = \frac{\delta\phi}{r\,\delta\theta} \text{ and } U_z = k\,\frac{\delta\phi}{\delta z} \quad (4.6)$$

where k is a constant.

Equations (4.3) and (4.4) are satisfied if

$$C_{11}\left[\frac{\delta^2\phi}{\delta r^2} + \frac{\delta^2\phi}{r^2\delta\theta^2}\right] + \left[C_{44} + k\,(C_{13}+C_{44})\right]\frac{\delta^2\phi}{\delta z^2} = 0.$$

and equation(4.5) is satisfied if

$$(C_{13}+C_{44}+k\,C_{44})\left[\frac{\delta^2\phi}{\delta r^2} + \frac{\delta^2\phi}{r^2\,\delta\theta^2}\right] + k\,C_{33}\,\frac{\delta^2\phi}{\delta z^2} = 0.$$

For a three dimensional non-zero solution these equations should be identical, so that

$$\frac{k\,(C_{13}+C_{44})+C_{44}}{C_{11}} = \frac{k\,C_{33}}{k\,C_{44}+C_{13}+C_{44}} = V \quad (4.7)$$

This gives a quadratic equation

$$C_{11}\,C_{44}\,V^2 + \left[C_{13}\,(2\,C_{44}+C_{13}) - C_{11}\,C_{33}\right]V + C_{33}C_{44} = 0. \quad (4.8)$$

The possible functions ϕ are the solutions of

$$\left(\nabla^2 + \frac{\delta^2}{\delta z_j^2} \right) \phi \qquad (j = 1, 2)$$

where $\nabla^2 = \frac{\delta^2}{\delta r^2} + \frac{\delta^2}{r^2 \delta \theta^2}$

and $z_j = \frac{z}{\sqrt{V_j}} \qquad (j = 1, 2)$

V_1 and V_2 are the roots of equation (4. 8);the corresponding values of k are given by

$$k_j = \frac{C_{11} V_j - C_{44}}{C_{13} + C_{44}}$$

The displacement components now are

$$U_r = \frac{\delta}{\delta r} (\phi_1 + \phi_2) ,$$

$$U_\theta = \frac{\delta}{r \delta \theta} (\phi_1 + \phi_2) \quad \text{and}$$

$$U_z = \frac{\delta}{\delta z} (k_1 \phi_1 + k_2 \phi_2) .$$

The corresponding stresses are

$$\left.\begin{aligned}
\sigma_{rr} &= \left[C_{11} \frac{\delta^2}{\delta r^2} + C_{12} \left(\frac{1}{r} \frac{\delta}{\delta r} + \frac{1}{r^2} \frac{\delta}{\delta \theta^2} \right) \right] (\phi_1 + \phi_2) \\
&\qquad + C_{13} \left(k_1 \frac{\delta^2 \phi_1}{\delta r^2} + k_2 \frac{\delta^2 \phi_2}{\delta z^2} \right) \\
\sigma_{\theta\theta} &= \left[C_{12} \frac{\delta^2}{\delta r^2} + C_{11} \left(\frac{1}{r} \frac{\delta}{\delta r} + \frac{1}{r^2} \frac{\delta^2}{\delta \theta^2} \right) \right] (\phi_1 + \phi_2) \\
&\qquad + C_{13} \left(k_1 \frac{\delta^2 \phi_1}{\delta z^2} + k_2 \frac{\delta^2 \phi_2}{\delta z^2} \right) \\
\sigma_{r\theta} &= (C_{11} - C_{12}) \left[\frac{1}{r} \frac{\delta^2}{\delta r \delta \theta} - \frac{1}{r^2} \frac{\delta}{r^2 \delta \theta} \right] (\phi_1 + \phi_2)
\end{aligned}\right]$$

$$\left.\begin{aligned}
\sigma_{\theta z} &= C_{44}\left[(1 + k_1) \frac{1}{r} \frac{\delta^2 \phi_1}{\delta\theta\delta z} + (1 + k_2) \frac{1}{r} \frac{\delta^2 \phi_2}{\delta\theta\delta z} \right] \\
\sigma_{r z} &= C_{44}\left[(1 + k_1 \frac{\delta^2 \phi_1}{\delta r\, \delta z} + (1 + k_2) \frac{\delta^2 \phi_2}{\delta r\, \delta z} \right] \\
\sigma_{zz} &= (1 + k_1) \frac{\delta^2 \phi_1}{\delta z_1^2} + (1 + k_2) \frac{\delta^2 \phi_2}{\delta z_2^2}
\end{aligned}\right\} \quad (4.9)$$

Let us take the axis of symmetry of the load as the z-axis and suppose that a perfectly rigid sphere of radius r is pressed normally against the plane $z = 0$ of a semi-infinite elastic medium $z \geqslant 0$. The shearing stresses vanish at all points of boundary $z = 0$, the normal stress is zero on the remainder of the boundary. The strained surface of the medium fits the rigid body over the part between the lowest point and a circular section of radius a. We have the following boundary conditions:

$$\sigma_{rz} = 0, \quad (4.10)$$

$$\sigma_{zz} = \begin{cases} \dfrac{-P}{(a^2 - r^2)^{\frac{1}{2}}} & r < a \\ 0 & r > a \end{cases} \quad (4.11)$$

$\frac{P}{\pi a^2}$ is the maximum Hertzian pressure, denoted by p , and in terms of load W, it is given by

$$p = \frac{3W}{2\pi a^3}$$

We now define a function $\psi(r, z)$ which satisfies equation (4.11). It can be shown that:

$$\phi_1(r, z_1) = \frac{P\sqrt{V_1}}{(1 + k_1)(\sqrt{V_1} - \sqrt{V_2})} \psi(r, z_1)$$

$$\phi_2(r, z_2) = \frac{P\sqrt{V_2}}{(1 + k_2)(\sqrt{V_1} - \sqrt{V_2})} \psi(r, z_2)$$

Equations 4.11 now reduce to

$$\left(\delta^2 \frac{\psi(r, z)}{\delta z^2} \right)_{z=0} = \begin{cases} -(a^2 - r^2)^{\frac{1}{2}}, & r < a \\ 0, & r > a \end{cases}$$

The determination of the stress field then follows from Chen.(182)

Writing $t = z + i a$, and $R = (t^2 + r^2)^{\frac{1}{2}}$, the stress components are conveniently expressed in terms of imaginary parts of function

$$\psi(r, z) = \text{Imag} \left[(t^3/3 - i a t^2 - \tfrac{1}{2} r^2 z) \log (R + t) - \frac{11}{18} R^3 + \frac{5}{6} r^2 R + \frac{3 i a t p}{2} + \tfrac{1}{2} r^2 z \right]$$

The derivatives needed for finding the components of the stress field can be obtained easily from $\psi(r, z)$

$$\frac{\delta \psi(r, z)}{\delta z} = \tfrac{1}{2} \text{Imag} \left[(t^2 - 2 i a t - \tfrac{1}{2} r^2) \log (R + t) - \frac{3}{2} Rt + 2 i a p + \tfrac{1}{2} r^2 \right]$$

$$\frac{\delta \psi(r, z)}{\delta r} = \frac{r}{2} \left[-z \log (R + t) - \frac{t z}{R + t} + \frac{2 t^2}{3 (R + t)} + \frac{z}{2} + \frac{2}{3} R \right]$$

$$\frac{\delta^2 \psi(r, z)}{\delta r^2} - \frac{1}{r} \frac{\delta \psi(r, z)}{\delta r} = \text{Imag} \left[\frac{R^2 + Rt + t^2}{3 (R + t)} - \frac{i a t}{R + t} - \frac{z}{2} \right]$$

$$\frac{\delta^2 \psi(r, z)}{\delta z^2} = \text{Imag} \left[z \log (t + R) - R \right]$$

$$\frac{\delta^2 \psi\ (r,\ z)}{\delta z\ \delta r} = \frac{r}{2}\ \text{Imag}\left[-\log (R + t) + \tfrac{1}{2} \log \frac{2\,i\,a - t}{R + t} \right]$$

The principal stress σ_{zz} is given by

$$\sigma_{zz} = \frac{P}{\sqrt{V_1} - \sqrt{V_2}}\left[\sqrt{V_1}\ \frac{\delta^2 \psi(r,\ z_1)}{\delta z_1^2} - \sqrt{V_2}\ \frac{\delta^2 \psi(r,\ z_2)}{\delta z_2^2} \right] \quad \ldots(4.12)$$

and

$$\sigma_{rr} + \sigma_{\theta\theta} = \frac{2P}{\sqrt{V_1} - \sqrt{V_2}}\left[\sqrt{V_1}\left(\frac{1}{V_3(1 + k_1)} - \frac{1}{V_1} \right) \frac{\delta^2 \psi(r,\ z_1)}{\delta z_1^2} \right.$$

$$\left. - \sqrt{V_2}\ \left(\frac{1}{V_3 (1 + k_2)} - \frac{1}{V_2} \right) \frac{\delta^2 \psi(r, z_2)}{\delta z_2^2} \right] \ldots\ (4.13)$$

$$\sigma_{rr} - \sigma_{\theta\theta} = \frac{2P}{V_3(\sqrt{V_1} - \sqrt{V_2})}\left\{ \frac{\sqrt{V_1}}{1 + k_1}\left[\frac{\delta^2 \psi(r,\ z_1)}{\delta r^2} - \frac{1}{r}\ \frac{\delta \psi(r, z_1)}{\delta r} \right.\right.$$

$$\left.\left. - \frac{\sqrt{V_2}}{(1 + k_2)}\left[\frac{\delta^2 \psi(r,\ z_2)}{\delta r^2} - \frac{1}{r}\ \frac{\delta \psi(r,\ z_2)}{\delta r} \right] \right] \right\} \ldots(4.14)$$

The principal stress σ_{rr} is calculated by adding equations (4.13) and (4.14)

Therefore $\sigma_{rr} = \frac{2P}{\sqrt{V_1} - \sqrt{V_2}}\left\{ \sqrt{V_1}\left[\left(\frac{1}{V_3(1+k_1)} - \frac{1}{V_1} \right) + \frac{1}{V_3(1+k_1)} \right] \frac{\delta^2 \psi(r, z_1)}{\delta z_1^2} \right.$

$$+ \sqrt{V_2}\left[\left(\frac{1}{V_3(1 + k_2)} - \frac{1}{V_2} \right) + \frac{1}{V_3(1 + k_2)} \right] \frac{\delta^2 \psi(r,\ z_2)}{\delta z_2^2}$$

$$\left. - \left[\frac{\sqrt{V_1}}{V_3(1 + k_1)}\ \frac{\delta \psi(r,\ z_1)}{r\ \delta r} - \frac{\sqrt{V_2}}{V_3(1+k_2)} \right] \frac{\delta \psi(r, z_2)}{r\ \delta r} \right\}$$

$$\ldots\ldots\ (4.15)$$

The maximum shear stress, σ_{shear}, is found from equations (4.12) and (4.15),

$$\text{i.e.} \quad \sigma_{shear} = (\sigma_{zz} - \sigma_{rr})/2$$

4.3 Application of fracture mechanics to the cracking due to the hardness test indentation

Griffith's[185, 186] energy balance concept and criterion for crack propagation form a strong basis for modern fracture mechanics. Irwin and his co-workers[187], circa 1950, gave an impetus to the evolution of theories of fracture mechanics which could be used for a ready analysis of a wide range of crack-loading geometrics.

The crack systems found in fracture testing are quite diverse and numerous. Although there might be several factors which influence the design of a particular test, aimed at studying the nature of the fracture process, the features which differentiate one system from another are, however, geometrical. In most cases, the standard approach is to follow the response of a pre-formed crack to applied loading. The aim of this approach is to generalize the description of the crack behaviour in terms of certain parameters such as the crack extension force and stress intensity factor (denoted by G and K in this text).

4.3.1 Crack extension force G

Consider a flat crack of length 2 c introduced into an elastic body subject to a uniform tensile stress. According to Griffith[186], a condition for crack propagation is

$$\frac{d}{dc}(U + W - S) \geq 0 \qquad (4.16)$$

where U is the strain potential energy stored in the elastic medium, W is the amount of work done by the applied load and S is the total surface energy. The term (U + W) is referred to as 'the free energy!

A crack-extension force is defined by

$$G = -d(-W + U)/dc$$

per unit width of crack front. If the crack extends without any displacement (u) of the loading system

$$G = -\left(\delta U / \delta c\right)_u \qquad (4.17)$$

which defines G as the strain-energy release rate per unit crack area (or width if the thickness of plate is considered as unity so that area = δ c X 1).

The above definitions of G have been made independently i.e. without considering any fracture criterion.

It may be seen that the Griffith's energy-balance equation (4.16) and equation (4.17) are similar. It means that 'G' parameter is closely connected to the conditions of crack extension.

Stress intensity factor 'K!.

The stresses in the neighbourhood of a crack, i.e. at a distance (r) small compared to the dimensions of the crack system, in polar coordinates, can be expressed as (188)

$$\sigma_{ij} = K_i (2\pi r)^{-\frac{1}{2}} f_{ij}(\theta)$$

where K_i is the stress-intensity factor. It depends upon the applied

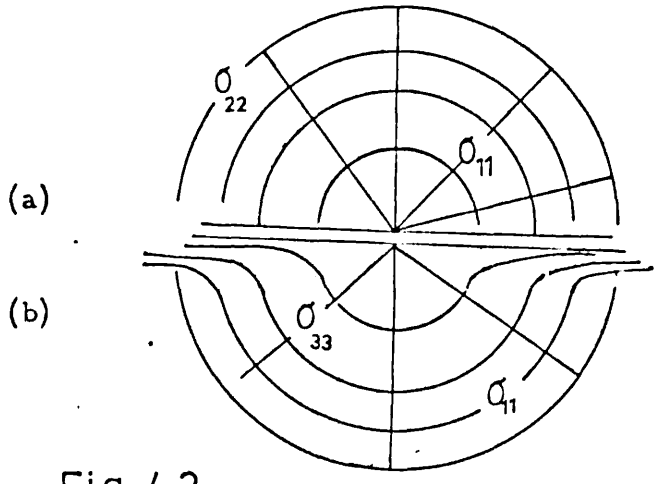

Fig. 4.2

Hertzian field. Stress trajectories:

(a) Half-surface view
(b) Side view.

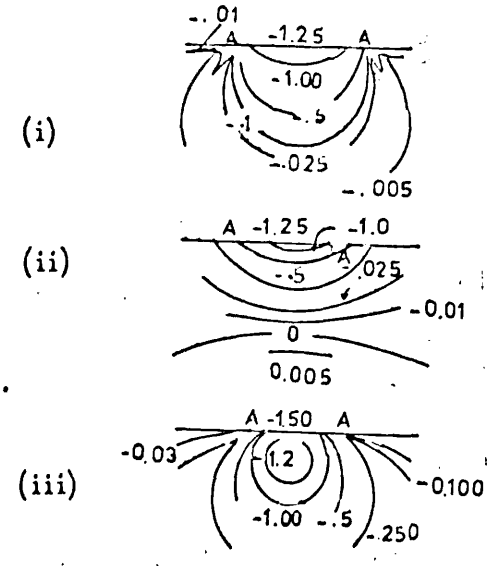

Fig. 4.3. Contours of principal normal stresses (i) σ_{11}, (ii) σ_{22}, and (iii) σ_{33}, in Hertzian field. Unit of stress is 'p', the indentation pressure, and the contact diameter is AA.

loading and crack configuration. It determines the intensity of the local field. Like G, it is also associated with the conditions of crack extension.

Irwin also defines K of the dimensions, stress x $(\text{length})^2$.

4.3.2 Fracture mechanics of microcracking

Here we analyse the mechanics of median vents in terms of Hertzian elastic field equations for point loading. The Hertzian stress fields, in single crystals with diamond structure, have been computed by Lawn[190]. Contours of principal stresses have been reproduced in Fig. 4.2 and Fig. 4.3.

Stresses σ_{11} and σ_{33} lie within the plane of symmetry, with σ_{11} everywhere tensile, σ_{33} everywhere compressive. σ_{22} is tensile within a region $\phi < 52^\circ$ beneath the indenter and compressive outside this region. A tensile component of the indentation on stress field, if sufficiently large, can sustain a brittle crack.

We now proceed to find the stress intensity factor in terms of the crack dimension c.

The mean indentation pressure 'p' under the indenter, is expressed as

$$p = \frac{P}{\pi a^2}$$

where P is the load on the indenter and 'a' is the radius of the contact zone. The radius of contact 'a' is given by

$a^3 = \frac{4k'}{3E} Pr$, where E is the Young's modulus of the material and k' a dimensionless constant, equal to unity if

the indenter and the specimen are of the same materials. If they are different, $k' = \frac{9}{16}\left[(1 - \nu_1^2) + (1 - \nu_2^2) \; E_1/E_2 \right]$, where E_1 and E_2 are the Young's moduli and ν_1 , ν_2 are the Poisson's ratios for the two materials.

For the sake of simplicity in the mathematical analysis, all the stresses are normalised in terms of the mean indentation pressure 'p' and all the lengths in terms of the radius of contact 'a'.

Two crack configurations need to be differentiated at this stage, before evaluating the stress intensity factor. The first one (C_s) is that crack which generally meets the free surface just outside the periphery of the circle of contact. The other is the internal elliptical crack. Cracking proceeds orthogonally to the greatest tensile stress σ_{11}, the trajectory σ_{22} carries the crack round in a circle about the axis and the trajectory σ_{33} is responsible for carrying it downwards, initially vertically and subsequently into a widening cone (C). (Fig. 4.4.).

According to Frank,[189] the crack path is controlled by the prior tensile stresses. It is also influenced by the prior stresses all over the previous path i.e. not by these stresses at its growing edge alone. The crack path is not exactly along the stress trajectories as explained above but still a very close relation exists between stress trajectories and ultimate crack path, at least qualitatively.

One may consider the contours of prior tensile stresses as a family of circles with a common plane θ = constant and the crack

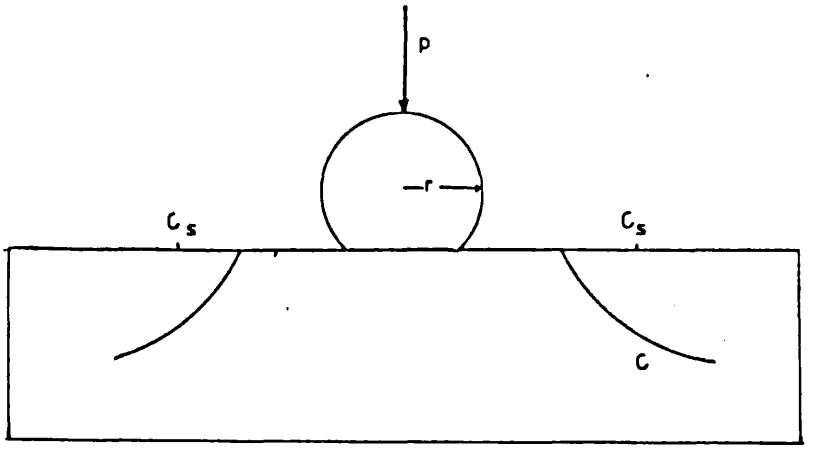

Fig. 4.4 . Hertzian contact.

(A sphere of radius 'r' is pressed against the surface of another material by a load 'W'. C_s denotes the surface ring crack and C the cone-crack.)

path to be coincident with one of these circles.

The stress intensity factor K is calculated in terms of the work to be done on the crack surfaces to bring them together. This work is expressable as an integral of prior stress multiplied by the subsequent relative displacement of corresponding points on the crack surfaces. From Lawn,[189] the stress intensity factor

$$K_i = \frac{2}{\pi} \cdot (c/a)^{\frac{1}{2}} \cdot \int_0^{c/a} \frac{\sigma_b \, db}{[(c/a)^2 - b^2]^{\frac{1}{2}}} \qquad (4.18)$$

where σ_b is the normal prior stress acting along the faces of the crack. In a Hertzian field solution, σ_b is the tensile stress $\sigma_{22}(z) = \sigma_{\theta\theta}(z)$.

From equations (4.13) and (4.14)

$$\sigma_{\theta\theta} = \frac{P}{\sqrt{V_1}-\sqrt{V}} \left\{ \left[\sqrt{V_1} \left(\frac{1}{V_3 (1 + k_1)} - \frac{1}{V_1} \frac{\delta^2 \psi (r, z_1)}{\delta z_1^2} \right) - \sqrt{V_2} \left(\frac{1}{V_3 (1 + k_2)} - \frac{1}{V_2} \frac{\delta^2 \psi (r, z_2)}{\delta z_2^2} \right) \right] \right.$$

$$\left. - \frac{1}{V_3} \left[\frac{\sqrt{V_1}}{1 + k_1} \left(\frac{\delta^2 \psi (r, z_1)}{\delta r^2} - \frac{\delta \psi (r, z_1)}{r \, \delta r} \right) - \frac{\sqrt{V_2}}{1 + k_2} \left(\frac{\delta^2 \psi (r, z)}{\delta r^2} - \frac{\delta^2 \psi (r, z_2)}{r \, \delta r} \right) \right] \right\} \qquad (4.19)$$

Irwin[187] defines K_i in terms of the crack extension force G and elastic constants (modulus of elasticity E and Poisson's ratio ν of the medium as

$$G = \frac{\pi}{E} (1 - \nu^2) K_i^2 \qquad (4.20)$$

Therefore, with the aid of eq: 4.18 , G can be written as

$$G = \frac{4(1-\nu^2)}{\pi E}\left(\frac{c}{a}\right)\left[\int_0^{c/a} \frac{\sigma_{\theta\theta}(z)\,dz}{(c/a^2 - z^2)^{\frac{1}{2}}}\right]^2 \qquad (4.21)$$

This equation can be written as

$$G = c/a \cdot \psi(c/a) \qquad (4.22)$$

The computed $\psi(\frac{c}{a})$ curves have maximum and minimum values, as shown in Fig. 5.8 .

Function $\psi(c/a)$, determined by using different crack models in diamond-structure single crystals, has been found to have a maximum at $c \simeq a/10$; a crack becomes visible at $c \simeq 3a$.

4.4 Birefringence caused by indentation.

The birefringence, or the double refraction, for silicon carbide crystals is quite small ($n_o - n_e = .049$). A strain-free crystal can, however, be made strongly birefringent by a work damage such as a surface abrasion, indentation or sandblasting. If a crystal which has been strained mechanically in this way, fractures it would tend to do so in such a manner as to relieve the mechanical strain. Thus the fragments would show less birefringence.

4.4.1 Contours of transmitted intensity.

One may assume that the crystal behaves as a doubly refracting plate around the indentation. The intensity of transmitted light, T, when a doubly refracting plate is introduced between the crossed nicol , is given by

$$T = a^2 \sin^2(2\gamma) \sin^2 \delta/2 \qquad (4.23)$$

where δ is the phase difference in two principal directions

at any point of the crystal plate, a is the amplitude of the incident plane-polarized light and 2 γ the angle between the incident light and a principal direction.

The phase angle δ is proportional to the thickness of the crystal, the birefringence Δn and inversely proportional to the wavelength of the incident radiation, i.e.

$$\delta = \left(\frac{2\pi t}{\lambda} \right) \Delta n \qquad (4.24)$$

The principal stresses, beneath a spherical indenter, in a crystal of thickness t, are given by the polar equation[191]

$$\sigma_{rr} = \frac{2 P \cos\theta}{\pi t r} \qquad (4.25)$$

The stress induced birefringence is given by

$$\Delta n = C \cdot \sigma_{rr} = \frac{2 C P}{\pi t r} \cos\theta \qquad (4.26)$$

where C is the stress-optical constant of the crystal.

As the birefringence is usually small, $\sin \delta/2$ in eq. (4.23) can be replaced by $\delta/2$. Using (4.23), (4.24) and (4.26) and noting that $2\gamma = 90 + \theta$, we get

$$T = \frac{4 a^2 C^2}{\lambda^2 r^2} \cos^2\theta \cdot \cos^2\theta \quad \text{or}$$

$$T = \frac{A^2}{r^2} \cdot \cos^4\theta \qquad (4.27)$$

where $A = \frac{2 a C P}{\lambda}$. In polar coordinates, eq. (4.27) may be written as

$$T_{(r,\,\theta)} = \frac{A^2}{r^2} \cos^4\theta \qquad (4.28)$$

The contours of constant intensities are, therefore, given by the polar equation

$$r^2 = \frac{A^2}{T} \cdot \text{Cos}^4\theta = K^2 \text{ Cos}^4\theta \qquad (4.29)$$

where $K^2 = A^2/T$.

CHAPTER V

RESULTS

5. The Hertzian contact between an indenter and a test specimen.

Sections 5.1-5.4 deal with the components of a stress field due to the Hertzian contact of a diamond ball indenter and α-SiC (type II) crystals. The Hertzian contact model considers two curved bodies characterized by their principal radii of curvature in the region of contact. But since the area of contact is smaller than the radii of curvature of the bodies in contact, we assume that one of the bodies (in the present case, a SiC crystal) is an elastic semi-infinite space.

5.1 Stress field components

The stress field components in polar coordinates, have been computed using the program STRFELD (Appendix I). The elastic constants of α-silicon carbide (type II) crystals, listed in Table 5.1, have been obtained from the survey of Chung.[192] The dimensions of stress field components and displacements (or lengths) have been normalised by assuming the maximum surface pressure 'p' exerted by the indenter, and the area of the contact between the indenter and the crystal 'a' each equal to unity.

TABLE 5.1.
Elastic constants of α-SiC (type II) and β-quartz.

C_{11}	C_{12}	C_{13}	C_{33}	C_{44}	Material
50.4	9.8	5.6	56.6	17.0	SiC (II)
11.66	1.67	3.28	11.06	3.606	β-quartz

(All constants are in units of 10^{-11} dynes. cm^{-2}.)

5.2 Dependence of stress field components on radial distance

The variation of the principal components of the stresses, σ_{rr}, $\sigma_{\theta\theta}$ and σ_{zz}, with the radial distance measured from the centre of circle of the contact, in the surface of the crystal is shown in Fig. 5.1. It is evident from this figure that the principal stresses are such that at every point $\sigma_{rr} > \sigma_{\theta\theta} > \sigma_{zz}$.

Fig. 5.2 shows the variation of the principal stresses along the axis of loading, from the surface of the crystal. Here also $\sigma_{rr} > \sigma_{\theta\theta} > \sigma_{zz}$, with σ_{zz} nearly equal to $\sigma_{\theta\theta}$ in a shallow region below the surface of the crystal. The direction of a principal stress at any point is obtained by drawing a tangent to the contours of the principal stresses at that point.

TABLE 5.2.
Computed values of principal stresses

No.	Distance below the surface	Principal stress		
		$\sigma_{\theta\theta}$	σ_{rr}	σ_{zz}
1	0.00	-0.5944	-.483	-1.00
2	0.10	-0.4191	-.338	-.991
3	0.20	-0.2888	-.222	-.964
4	0.3	-0.1985	-.132	-.923
5	0.4	-0.1396	-.063	-.873
6	0.5	-0.1038	-	-
7	0.6	-0.0838	+.029	-.759
8	0.7	-0.0744	+.059	-.752
9	0.8	-0.0717	+.092	-.620
10	0.9	-0.0731	+.100	-.590
11	1.0	-0.0769	+.113	-.551
12	1.1	-0.1272	+.125	-.502
13	1.2	-0.1513	+.134	-.461
14	1.3	-0.1621	+.140	-.424
15	1.4	-0.1676	+.146	-.390
16	1.5	-0.1676	+.159	-.359

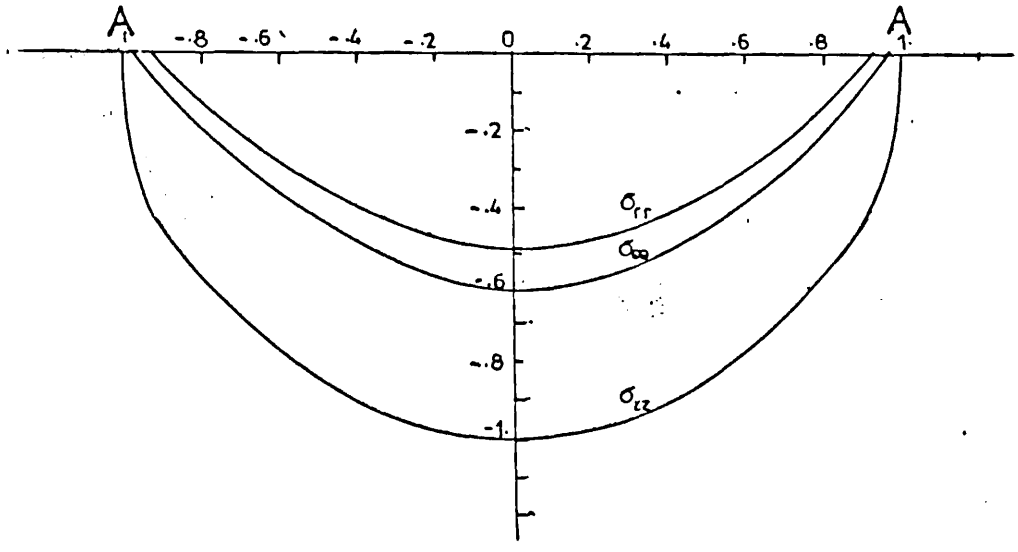

Fig. 5.1.

Variation of principal stresses in the surface of SiC in contact with a spherical indenter.

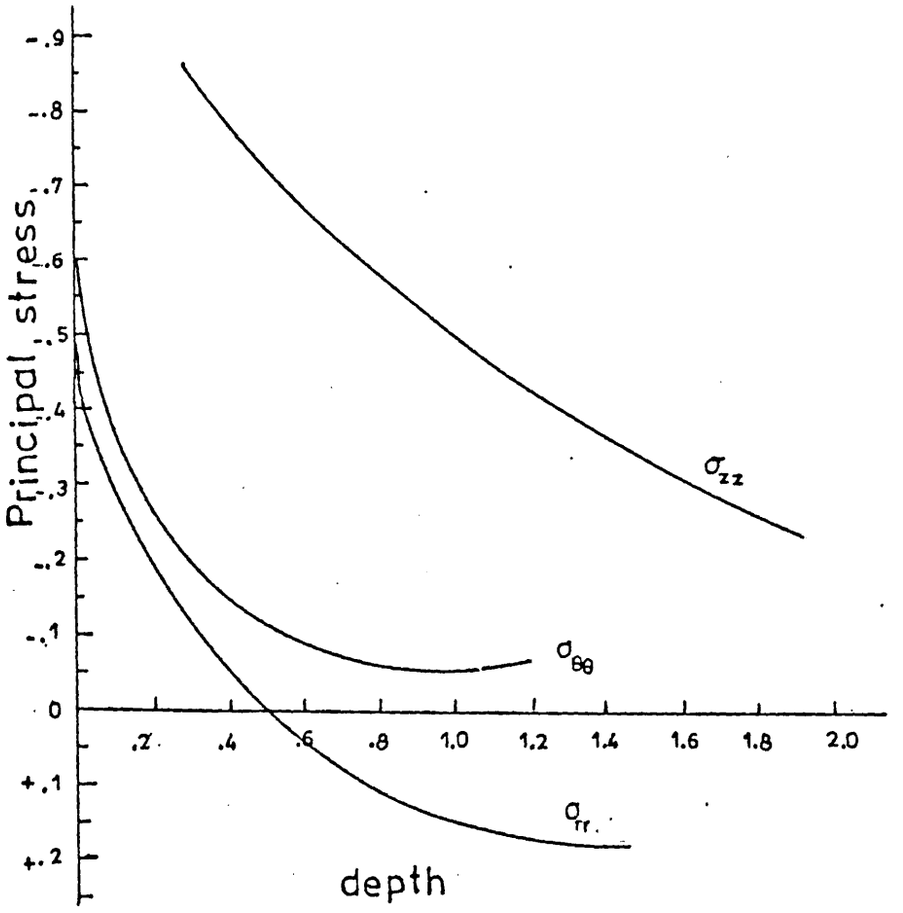

Fig. 5.2. Variation of principal stresses, along the axis of loading, below the surface.

Contours of principal stresses σ_{zz} and σ_{rr} have been plotted in Figures 5.3 and 5.4. These curves represent the polar functions obtained from equations 4.9 (Section 4.2). The stresses σ_{zz} and σ_{rr} lie within the plane of symmetry through the normal load axis. σ_{zz} is everywhere compressive while σ_{rr} is compressive in a shallow region beneath the indenter and tensile further down. The σ_{zz} contours meet the surface of the crystal orthogonally within the radius of contact. They have points of inflexions outside the circle of contact where they turn sharply and become parallel to the surface of the crystal. The σ_{rr} trajectories have inflexions at distances approximately equal to 1/4th of the radius of contact circle. They are in the shape of a hyperbola meeting the surface of the crystal asymptotically at large distances from the centre of the contact circle.

5.3 Shear Stress

Table 5.3 contains some of the results for the maximum shear stress taken from the output of the program STRFELD. The highest value of the maximum shear stress is obtained by plotting the results given in Table 5.3 . This is found to be 0.405 (with the maximum surface pressure as the units of stress), at a depth of 0.4 (the radius of the circle of contact as the unit), on a point on the axis of symmetry.

Fig 5.5 shows the variation of maximum shear stress with the distance downward from the free surface of the crystal.

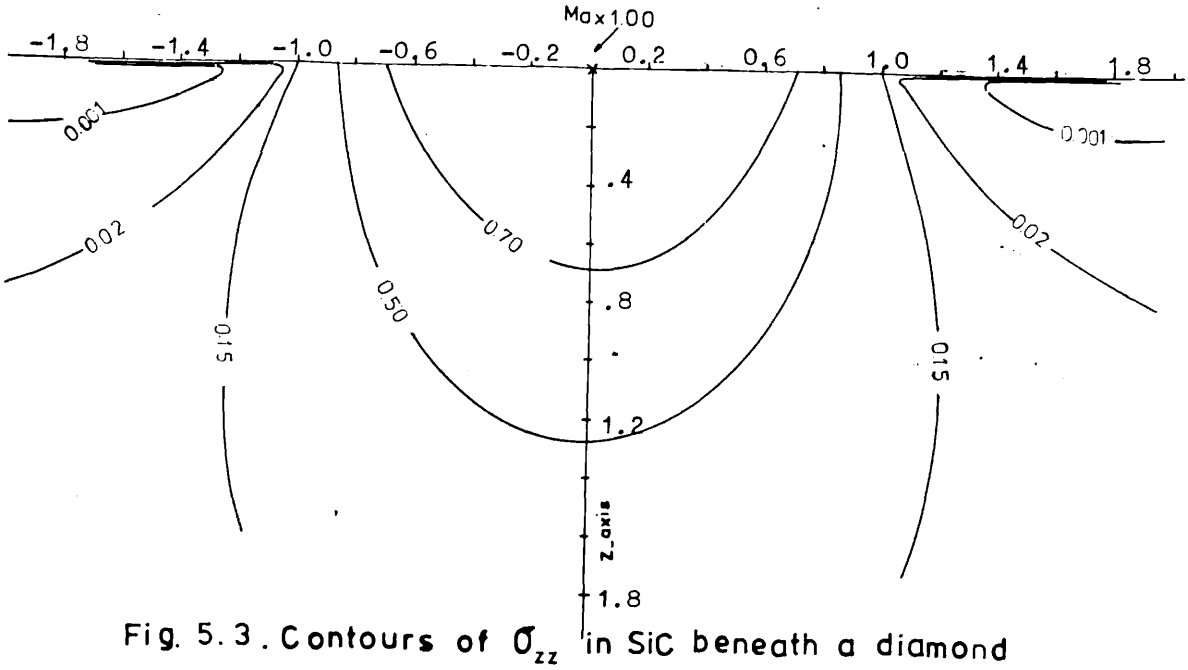

Fig. 5.3. Contours of σ_{zz} in SiC beneath a diamond ball indenter.

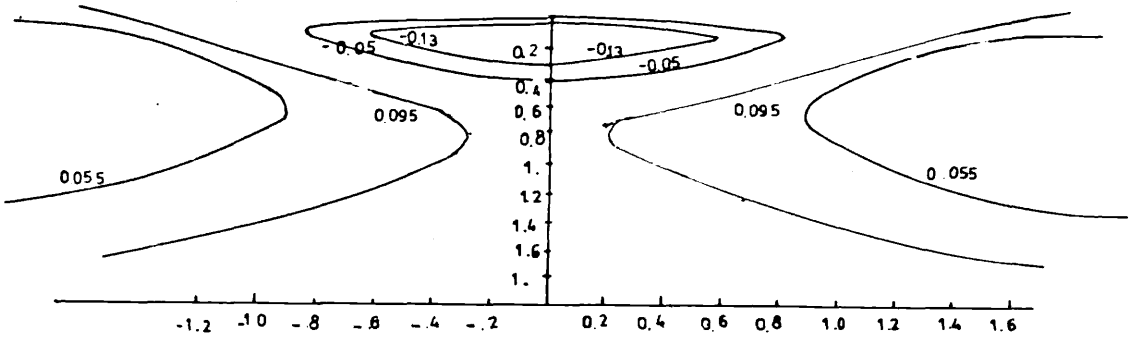

Fig. 5.4. Contours of σ_{rr} plotted for SiC.

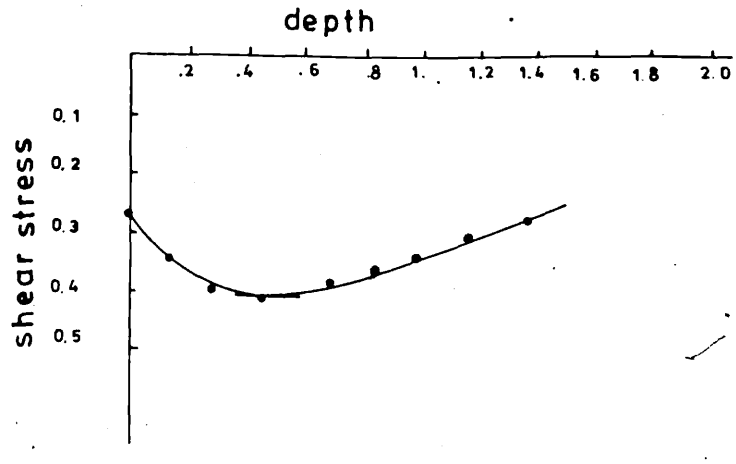

Fig. 5.5. Distribution of shear stress in indented SiC.

TABLE 5.3.

Max. shear stress distribution due to diamond ball indentation of SiC

No.	Distance below the surface of the crystal	r = 0		Max. shear stress $= (\sigma_{zz} - \sigma_{rr})/2$
		σ_{zz}	σ_{rr}	
1	0	1.0	-.483	.258
2	0.1	.991	-.338	.326
3	0.2	.996	-.222	.371
4	0.3	.923	-.132	.395
5	0.4	.873	-.063	.405
6	0.6	.759	+.029	.394
7	0.7	.702	+.059	.381
8	0.85	.620	+.092	.356
9	1.0	.551	+.113	.332
10	1.2	.461	+.134	.297
11	1.4	.390	+.146	.268
12	1.6	.332	+.153	.243
13	1.8	.284	+.158	.221
14	2.0	.245	+.162	.203

5.4. Contours of maximum shear stress

Table 5.4 has been constructed from the output of the program STRFELD. It gives the coordinates of those points for which shear stresses are equal. For example, we choose an arbitrary value 0.15 for the shear stress and read the output data and note down the distances from the surface of all those points as well as their distances from the axis of loading for which the shear stress is 0.15 ($\pm$ 0.015). Contours of equal shear stress for SiC (6H) are shown in Fig.5.6. For the purpose of comparison, the contours of equal shear stress for a nearly isotropic body, β - quartz,

using the elastic constants given in Table 5.1 , have been plotted (Fig. 5.7).

It may be seen that the maximum shear stress, (in Fig.5.6), is 0.405, and it is concentrated at a depth of 0.4 along the axis of loading. For β-quartz, the greatest value of the maximum shear stress is 0.33 and this occurs at a depth of about 0.44, also along the axis of loading. The results for β-quartz are in agreement with the computed results of Chen[182]. This agreement testifies the accuracy of our computer program STRFELD .

TABLE 5.4

Maximum shear stress	Parameters		Maximum shear stress	Parameters	
	Depth	Radius		Depth	Radius.
0.15	.6	0.95	0.35	0.2	.40
	.7	0.95		0.3	.50
	.95	0.95		0.5	.50
	1.1	0.93		0.6	.40
	1.3	0.90		0.7	.35
	1.5	0.90		0.8	.1
	2.0	0.85		0.95	0
0.20	0.0	0.85	0.375	0.2	0
	0.1	0.85		0.4	.40
	0.4	0.85		0.5	.35
	0.7	0.85		0.6	.30
	1.0	0.80		0.7	.15
	1.1	0.75		0.8	0
	1.3	0.70	0.40	0.3	0
	1.5	0.60		0.4	.1
	1.7	0.50		0.6	0
	2.0	0.20	0.405	0.4	0
0.30	0.0	0.60			
	0.2	0.60			
	0.4	0.60			
	0.5	0.60			
	0.7	0.60			
	0.8	0.50			
	0.95	0.40			
	1.1	0.20			
	1.2	0.0			

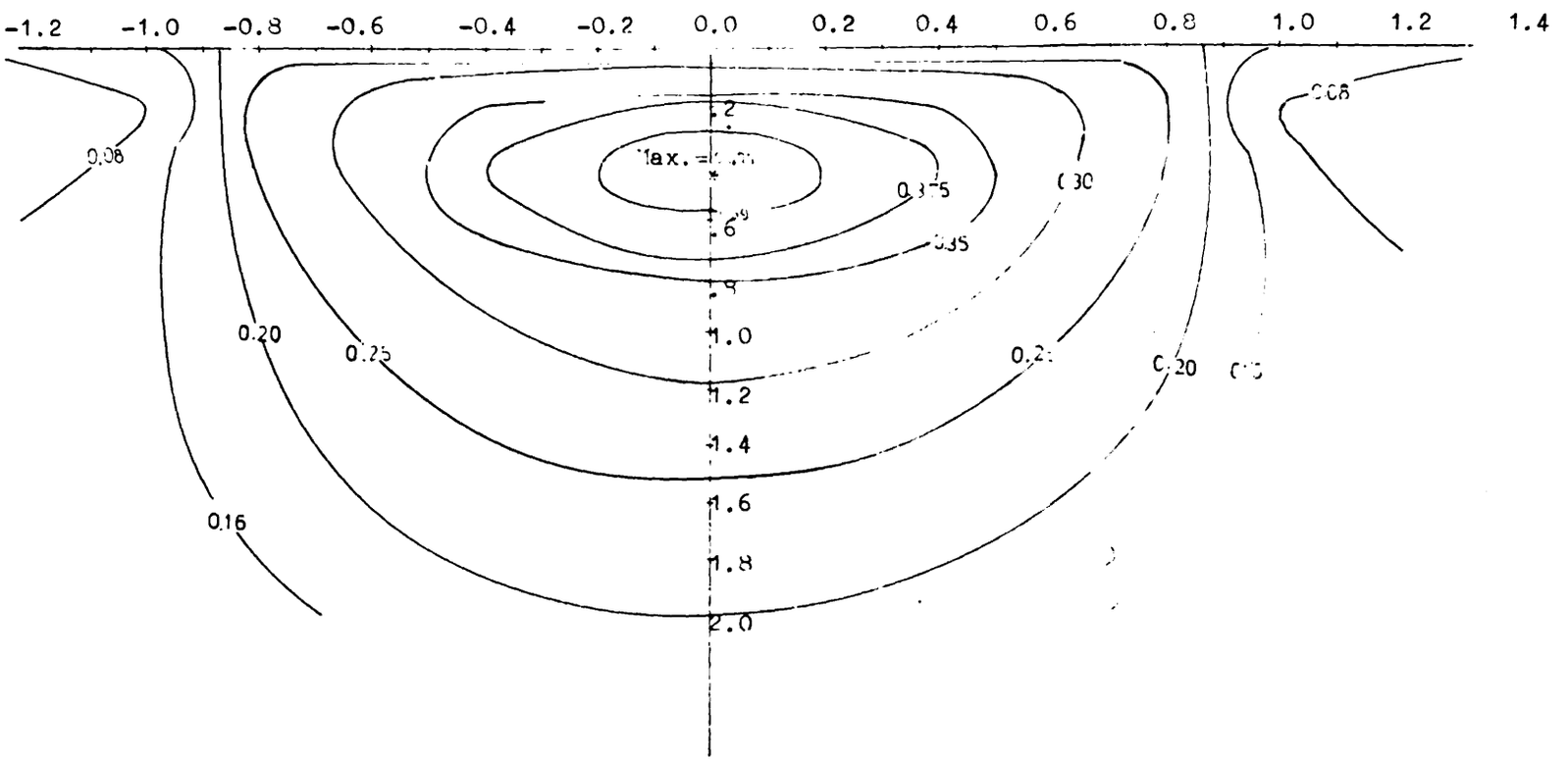

Fig. 5.6. Shear stress distribution in SiC beneath a diamond ball indenter.

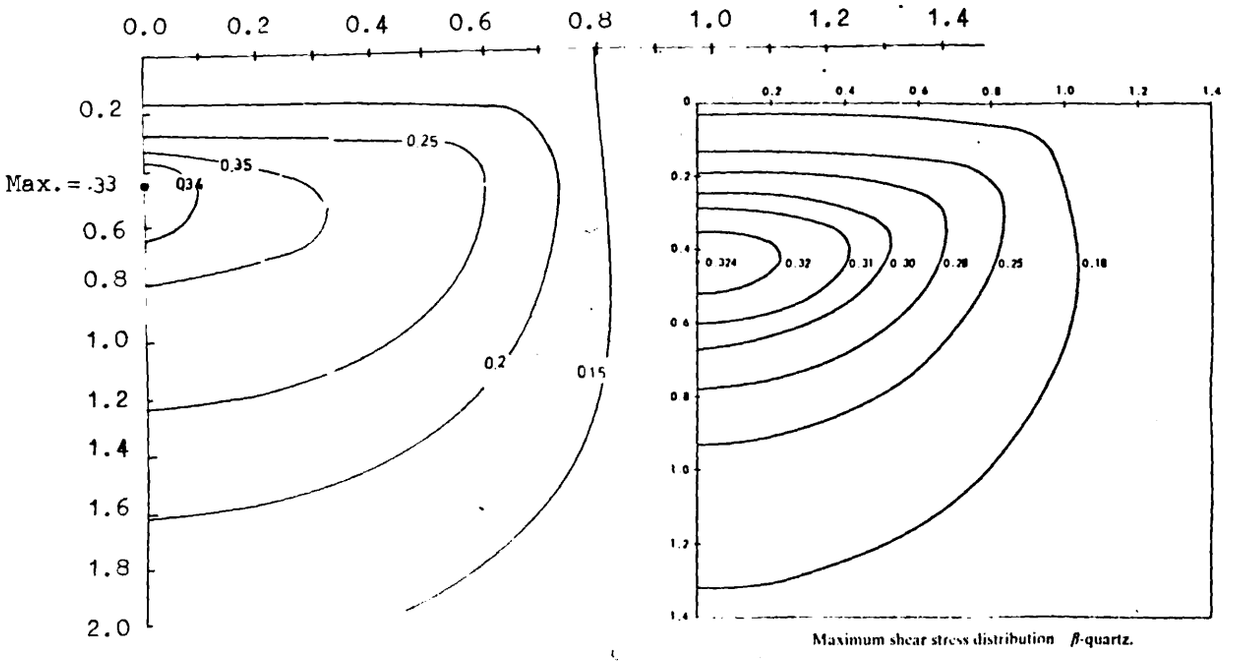

Fig. 5.7. Shear stress distribution in β-quartz.

5.5 Calculation of the crack extension force for SiC (6H) crystals

The crack extension force G is given by the equation (Section 4.3.2), as

$$G = \frac{4(1-\nu^2)}{E}\frac{c}{a}\left[\int_0^c \frac{\sigma_{\theta\theta}(z)\,dz}{(c/a^2 - z^2)^{\frac{1}{2}}}\right]^2 \qquad (5.1)$$

In practice, it is the quantity $\frac{G}{G^*}$ which is evaluated. G^* is the crack extension force corresponding to the equilibrium crack length which is determined from $\psi(c/a)$ curves.

A computer program, Ø R I Ø N (Appendix II), was written to solve the squared term of the equation (5.1). The main program solves the stress field $\sigma_{\theta\theta}$ while a subroutine is used in the main program for obtaining the integral for a given crack length. Table 5.5 gives the computed values of $\psi(c/a)$ and $\frac{G}{G^*}$.

Fig. 5.8 is a plot of $\psi(\frac{c}{a})$ vs. c. The equilibrium crack length is $\simeq$ 0.05 (in units of the radius of contact circle). Fig. 5.9 shows G/G* as a function of the crack length for SiC. The curve shown in this figure can be divided into four distinct branches viz, c_0, c_1, c_2 and c_3, as in Fig. 5.10 which has been reproduced from the work of Lawn on the crack extension forces in glass.(193) According to Lawn, c_0 and c_2 represent unstable equilibrium and c_1 and c_3 the stable equilibrium. Crack extension force G must be increased for any increase in c_0 and c_2. c_1 and c_3 increase by increasing G. The critical condition for the growth of a cone crack is found at the point of merger of c_1 and c_2. The crack is forced up the hill to

to the right side of this point of merger (Fig. 5.10), and the stable length c_2 becomes unstable till the crack again attains a stable length c_3. The crack is visible when it has reached the length c_3. From Fig. 5.9 , we find this length as approximately equal to unity (considering the radius of contact circle as the unit of length). In the case of amorphous silicates, Lawn[193] has determined this length as $\sim$3a, which is three times the length of stable crack in a silicon carbide crystal .

TABLE 5.5

(From output file of computer program ØRIØN given in Appendix II)

No	crack length (c/a)	$\psi(c/a)$	$(c/a) \times \psi(c/a)$	$\frac{G}{G^*} = \frac{c.\ \psi(c/a)}{c^*.\ \psi(c/a)^*}$
1	0.01	.53	0.0053	0
2	0.02	.28390850	567817	0.
3	0.03	41723100	1251693	0.2
4	0.04	64707100	2588284	0.42
5	0.05	125917080	6295854	1.00
6	0.06	33787450	2027247	0.32
7	0.07	61167500	4281725	0.6
8	0.08	18590850	1487268	0.8
9	0.09	153175877	13785829	2.1
10	0.10	87919790	8791979	1.4
11	0.15	22788613	3418292	0.55
12	0.20	4174060	834812	0.14
13	0.30	7393836	2218151	0.35
14	0.40	9758762	3903505	0.22
15	0.50	936452	468226	0.07
16	0.60	1319776	791866	0.12
17	0.70	894014	625810	0.1
18	0.80	2574427	2059542	0.08
19	0.90	903398	813059	0.13
20	1.00	514381	514381	0.08

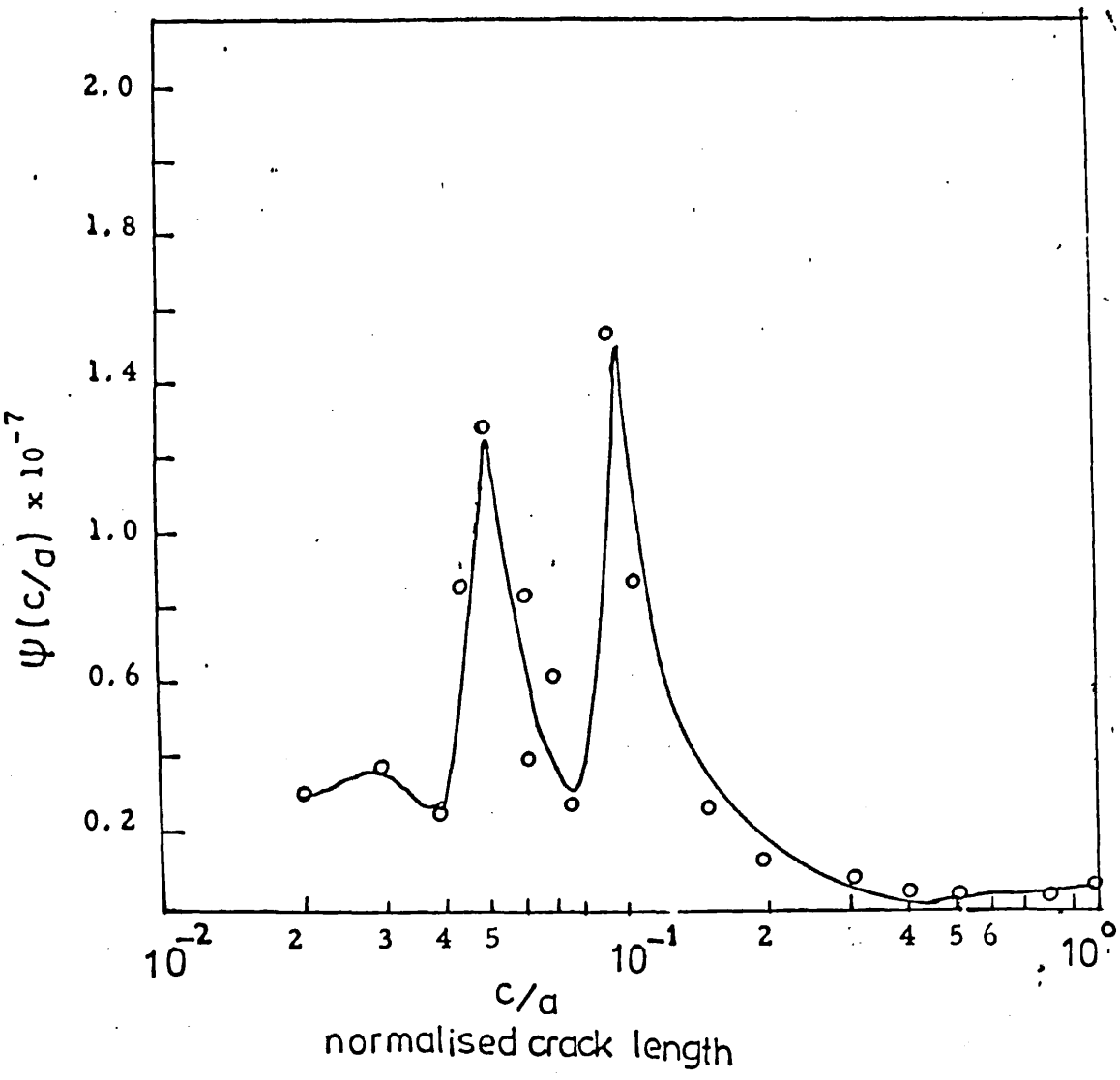

Fig.5.8. Computed curve for crack extension function ψ c/a for SiC type II.

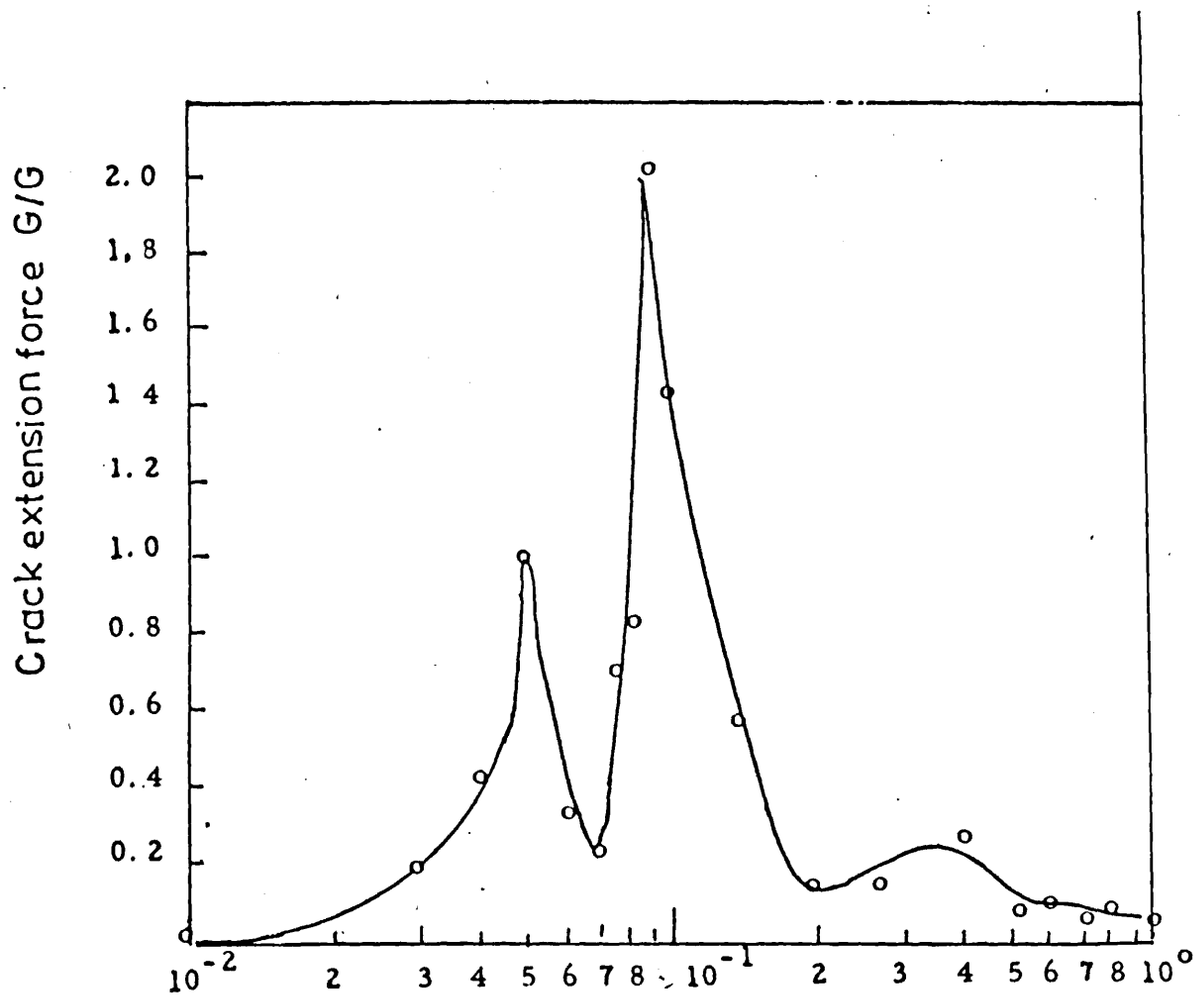

Fig. 5.9. Computed curve for SiC type II.

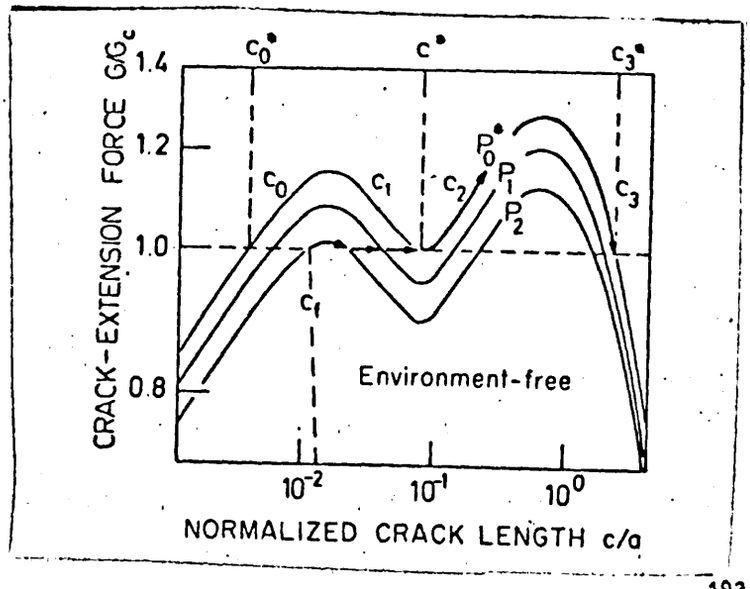

(from Lawn[193])

Fig.5.10. The stages of crack extension in glass.

a.

b.

Fig. 5.11 . Cone crack [cross-sectional profile as seen in the $(10\bar{1}0)$ plane]

5.6 Propagation of the cone crack

The cone-crack experiments were carried out on thickest available single crystals of silicon carbide and indentations on them were made with a diamond ball indenter. The indentations, systematically varying with load, were equally spaced along one of the $<1\bar{1}00>$ edge of the test sample.

Fig. 5.11 a. illustrates the side view of an indentation with 1 kg load, on the (0001) plane. A cone-crack is not yet formed. The central deformation zone can be noticed. Fig. 5.11 b. shows the profile of a cone-crack as seen in the $(10\bar{1}0)$ plane. This crack is produced by an indentation with 3 kg load.

Fig. 5.11a represents the subcritical growth between c_1 and c_2 branches of Fig. 5.10., whereas, Fig. 5.11b. corresponds to the fully developed cone-crack of length c_3.

The data collected from the cone-crack experiments are not sufficient to determine the relationship between the cone-crack length and the indentation load, due to non-availability of thick and transparent (colourless) crystals. Nevertheless, these results are believed to be adequate enough to illustrate the manner in which a surface ring crack develops into a full cone-crack.

5.7 Environmental (water adsorption) effects on microhardness

The purpose of the present investigation is to study the extent to which water adsorption affects the observed anisotropy in the microhardness. This study was limited to the (0001) planes of silicon carbide crystals, as they were the only planes well-formed in almost all the available crystals. A commercial hardness testing

apparatus: the "Tunkon" hardness tester was employed. This type of apparatus is specially convenient when indentations are to be made on a specimen placed in a liquid anhydrous agent.

Orientations of the crystals were determined from their habit faces. Indentations were made with the Vickers pyramid and the double-cone (d.c.) indenters using loads under 150 gms. Low loads were used so that the indentations were shallow enough to reveal adsorption effects of water which extend to extremely small depths from the surface of the crystals. The time of indentation for Vickers pyramid indenter was 15 seconds and that for double cone 30 seconds.

In order to obtain visible indentations at low loads and to evaluate 'unrecovered' hardness, it is essential to coat the surface of a crystal with a very thin layer of silver using a vacuum evaporation plant. At the time of indentation such a film is torn inside the indentation area and can not recover. A microscopic examination will, therefore, reveal the full area of contact which existed when the maximum pressure had been made. Grodzinski[5] showed that this is a very sensitive way for determining the 'elastic' or 'unrecovered' hardness. For studying the water absorption effect on hardness, the crystals were not, however, coated with silver in the vacuum plant. An alternative method to obtain visible indentations as suggested by Brodie and Smoluchowski[194], and

Bergsman,[195] was used in this work.

The diamond indenter was coated with a thin layer of silver in a vacuum coating plant. The indenter needed recoating after each indentation because the previous coating was left behind inside the hardness impression.

The double cone indenter was found to be more useful than the Vickers indenter to investigate the water adsorption effects. Indentations made with the Vickers indenter with loads less than 100 g were not clearly visible. The average diagonal lengths of Vickers impressions were 9.2 μ and 8.6 μ on an as-received crystal and after it was dry-dehydrated, respectively. These lengths correspond to Vickers hardness numbers 2190 $kg.mm^{-2}$ and 2506 $kg.mm^{-2}$ respectively.

5.7.1 'Dry-dehydrated' condition and 'wet' condition hardness.

Table 5.6 gives the double-cone hardness measured at various loads under the two conditions. All indentations were made parallel to each other to avoid directional anisotropy. Measurements of diagonal lengths of four indentations, for a given load and a crystallographic direction, were averaged.

It was observed that both the 'dry-condition' and 'wet-condition' hardness varied with load, as shown in Fig. 5.12. It was also noted that the difference between the two decreased with the increase of load. For instance, the increase of load from 20 g to 100 g, causes the $\%\delta H_{d.c}$ to decrease from 33.2 to 19.7.

TABLE 5.6

plane	No.	load(W) (g)	length of indent. (ℓ) mm x 100 ± (0.02)		$H_{d.c} = \frac{W}{0.361 \times \ell^3}$		$\delta H_{dc} = \frac{{}^{dry}H_{dc} - {}^{wet}H_{dc}}{{}^{dry}H_{d.c}}$ (%)
			'dry-'	'wet-'	'dry-'	'wet-'	
	1	20	2.60	3.05	2814	1952	30.6
	2	50	3.65	4.00	2843	2164	23.9
$(10\bar{1}0)$	3	100	4.70	4.95	2668	2283	14.4
	4	150	5.50	5.80	2497	2185	12.5
	5	200	6.35	6.35	2164	2164	0.0
	1	20	2.62	3.00	3071	2052	33.2
	2	50	3.55	3.95	3095	2247	27.3
(0001)	3	100	4.60	4.95	2846	2283	19.7
	4	150	5.40	4.90	2638	2366	10.3
	5	200	6.25	6.25	2269	2269	0.0

The results of Table 5.6 were used to find out the value of Meyer exponent 'n' which gives the relation between the hardness and load applied. This exponent is defined by the equation: $\log P = n \log \ell + D$ (ℓ = length of indentation). Fig. 5.13 shows the log-log plot for (0001) plane for both conditions. The slope of the two lines are:

$$n_{(\text{dry-condition})} = 2.66$$

$$n_{(\text{wet-condition})} = 3.33$$

5.7.2 Directional hardness anisotropy in 'dry-' and 'wet-' conditions

Table 5.7 gives 'unrecovered' double-cone hardness of (0001) plane, in different crystallographic directions. Indentations load was 50 g and indentations were made at 30° intervals.

The results contained in Table 5.7 indicate that the maximum hardness is along $<11\bar{2}0>$ directions. and minimum along $<01\bar{1}0>$, in both the dry and wet conditions. The results can be summarised as :

Double-cone microhardness ratio

	$<11\bar{2}0>$		$<01\bar{1}0>$
Dry-condition	1	:	0.96
Wet-condition	1	:	0.96

We note that the microhardness ratios, in the two conditions, are approximately equal. Therefore, the hardness anisotropy, in silicon carbide, does not depend on whether the crystals are in the dry condition or wet condition (as-received).

TABLE 5.7.

(Load on the indenter W=50 g)

No.	Angle of indenter from $\langle 11\bar{2}0 \rangle$, (deg.) (degrees)	Direction	(Average) Indentation length (ℓ) mmx100 ±0.02 dry-condition	wet-condition	$H_{d.c} = \frac{W}{0.361 \times \ell^3}$ (kg. mm^{-2}) dry-	wet-	$\delta H = \frac{('dry-') - ('wet-')}{('dry-')}$ (%)
1	0	$11\bar{2}0$	3.85	4.15	2427	1937	25.67
2	30	$01\bar{1}0$	3.90	4.20	2335	1869	19.95
3	60	$\bar{1}2\bar{1}0$	3.87	4.18	2390	1896	20.67
4	90	$\bar{1}100$	3.90	4.18	2335	1896	18.8
5	120	$\bar{2}110$	3.85	4.16	2427	1923	20.76
6	150	$\bar{1}010$	3.88	4.18	2371	1896	20.03
7	180	$\bar{1}\bar{1}20$	3.86	4.16	2408	1923	20.14

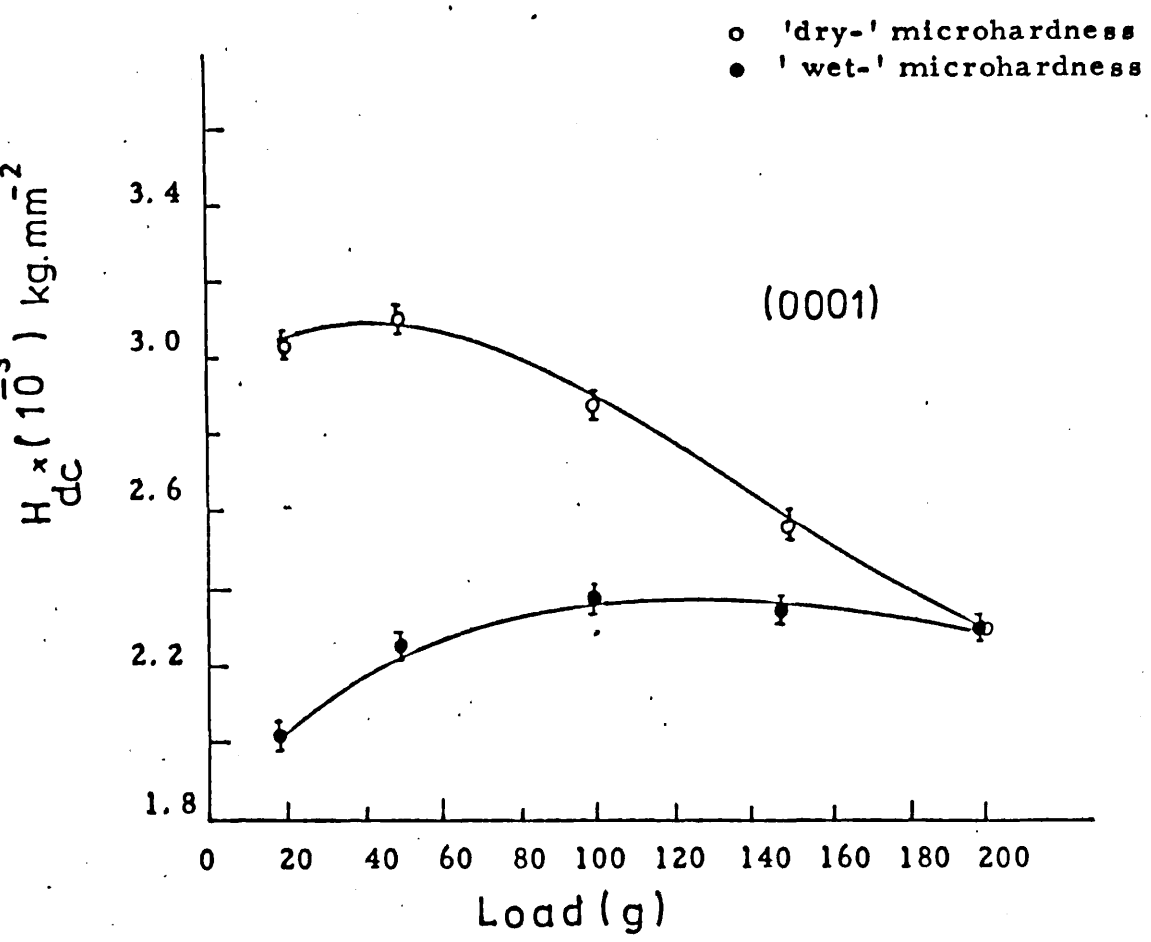

Fig .5.12

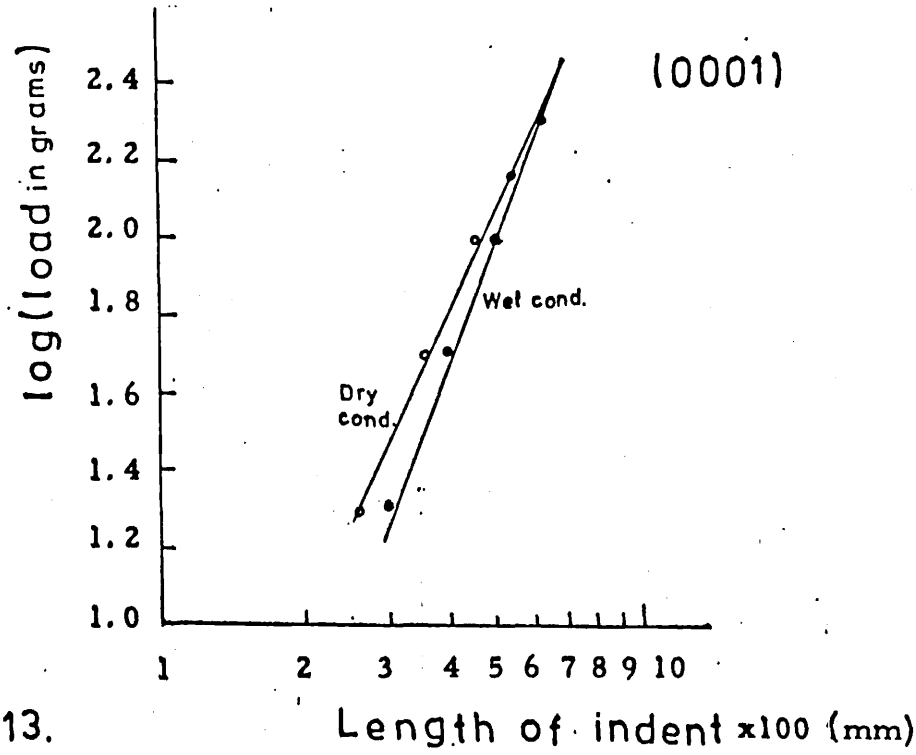

Fig. 5.13.

5.8 Hardness and annealing

The effect of annealing on the microhardness of silicon carbide crystals is hitherto unreported in the literature. Table 5.8 gives double cone hardness numbers for as-received and annealed crystals. Annealing was carried out in the departmental Plasma Torch, for fifteen minutes, prior to indentation.

TABLE 5.8

(Indenter load = 200 g. Dark green SiC crystal type II)

Indenter's orientation on (0001)	D.C Hardness of as-received crystals (kg/mm^2) $\pm$ 0.5 %	D.C. Hardness of annealed crystals(kg/mm^2) at* 2000°C	2500°C	3000°C
// to $<11\bar{2}0>$	3345	3215	3111	2922
at 45° to $<11\bar{2}0>$	3296	3111	2975	2797
to $<11\bar{2}0>$	3256	2975	2827	2679

* All temperatures were estimated, with a disappearing filament radiation pyrometer, within an accuracy of +1.0 %.

The double cone hardness of silicon carbide crystals, as seen in Table 5.8, is found to decrease with the annealing temperature. The hardness (along the $<11\bar{2}0>$ direction) falls from 3215 kg. mm^{-2} to 2922 kg. mm^{-2}, for an increase in annealing temperature of 1000°C. The anisotropy in the hardness remains constant in this range and this implies that the crystal was deforming on the $(0001)<11\bar{2}0>$ slip systems at high temperatures. If other systems come into play, at high temperatures, they would either reduce the anisotropy or even reverse it.

The double cone hardness number on a $(10\bar{1}0)$ plane, along

$<11\bar{2}0>$, changes from being 15% greater than that in the [0001] direction, at room temperature, to 11 % at 3000°C. The results suggest that the anisotropy in microhardness is being affected by the $\{10\bar{1}0\}<0001>$ slip systems at high temperatures. Evidence that this slip takes place can be seen in the numerous slip lines at 90° to the $<11\bar{2}0>$ (See Fig. 5.28).

5.9 Directional microhardness anisotropy and effective resolved shear stress (E.R.S.S.)

Directional microhardness anisotropy of silicon carbide crystals (type II) was studied using the Knoop and double cone indenters. The observed anisotropy has been explained in terms of the effective resolved shear stress, using the analysis of Daniels and Dunn. The results of the Knoop hardness tests are presented in Table 5.9. The angle θ is the angle which the long diagonal of the Knoop indenter made with the $<11\bar{2}0>$ direction. Indentations were made from 0° to 360° at 20° intervals, but, because of the presence of a symmetry plane at $\theta = 180°$, the hardness values shown in Table 5.9 are for the range from 0° to 180° only.

Fig. 5.14 shows the variation of Knoop hardness with the azimuthal angle for (0001) and $(01\bar{1}0)$ planes. On the (0001) plane, indenter's rotation produced a maximum variation of ~2%, whereas, the variation on the $(0\bar{1}10)$ plane was 17.8 %. The hardest and softest directions are found to be $<11\bar{2}0>$ and $<10\bar{1}0>$ on the (0001) plane, respectively. On the $(01\bar{1}0)$ plane, they are $<11\bar{2}0>$ and $<0001>$, respectively.

The double-cone hardness anisotropy for a $(10\bar{1}0)$ plane is shown in Fig. 5.15, a . This curve is consistent with the Knoop

TABLE 5.9

(Load W=200g)

No.	θ (deg.)	(0001) plane		($10\bar{1}0$) plane	
		length of the indent (microns) $\pm$ 0.1 = (ℓ)	Knoop hardness = $\frac{W}{0.07028 \times \ell^2}$ ($kg.mm^{-2}$)	length of the indent (microns) $\pm$ 0.1	Knoop hardness ($kg.mm^{-2}$)
1	0	31.3	2904	35.2	2290
2	10	31.3	2904	35.7	2232
3	20	31.4	2886	36.2	2171
4	30	31.5	2867	36.5	2130
5	40	31.5	2867	37.0	2078
6	50	31.4	2886	37.4	2034
7	60	31.2	2923	38.0	1970
8	70	31.3	2904	38.4	1929
9	80	31.4	2886	39.0	1870
10	90	31.4	2886	39.0	1882
11	100	31.3	2904	38.5	1919
12	110	31.3	2904	38.4	1929
13	120	31.2	2923	37.5	2023
14	130	31.4	2886	37.0	2078
15	140	31.3	2904	36.5	2136
16	150	31.3	2904	36.3	2159
17	160	31.4	2886	35.6	2118
18	170	31.5	2867	35.7	2232
19	180	31.3	2904	35.2	2296

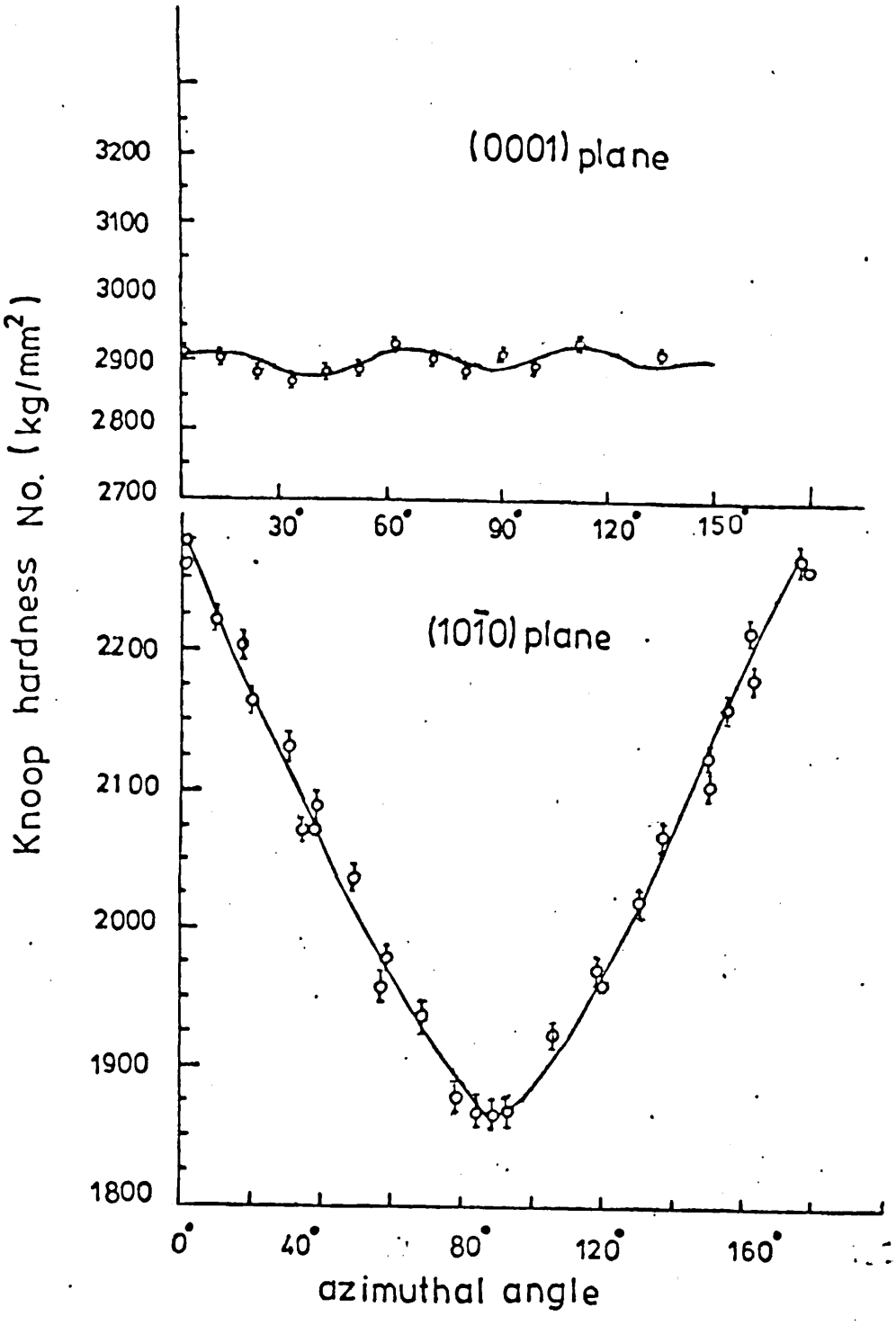

Fig. 5.14. Anisotropy in the hardness of SiC(type II) crystals.

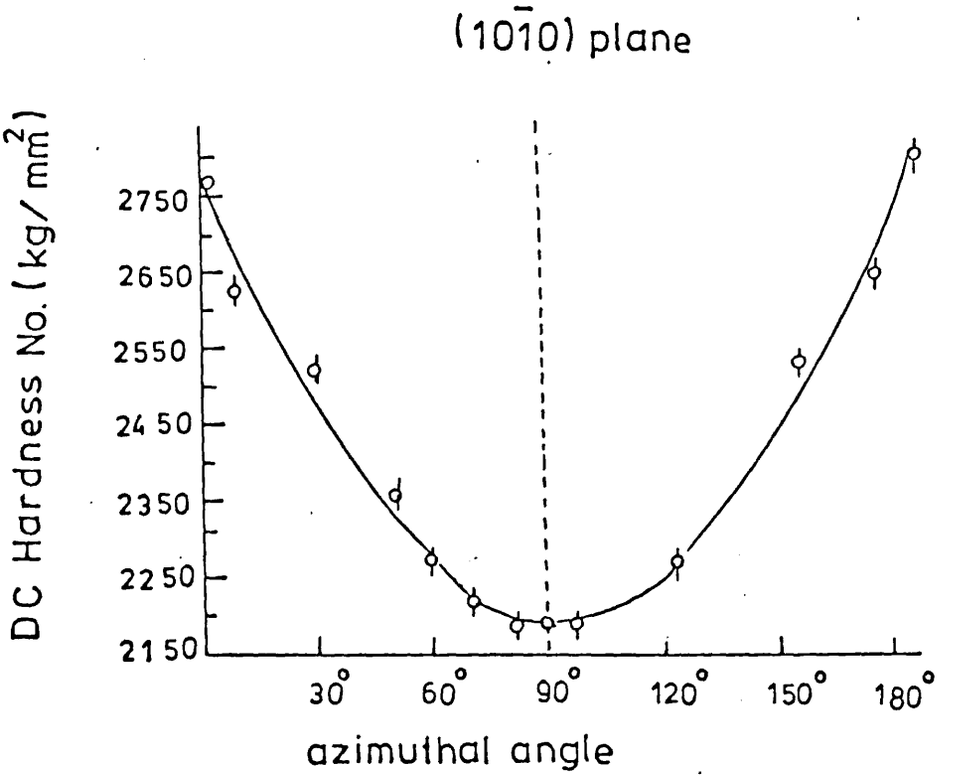
(10$\bar{1}$0) plane
DC Hardness No. (kg/mm^2)
2750
2650
2550
2450
2350
2250
2150
30°
60°
90°
120°
150°
180°
azimuthal angle

Fig. 5.15.

hardness curve of Fig. 5.14 ., except that the double-cone hardness is higher than the Knoop hardness at the same load.

The maximum effective resolved shear stress, produced by the Knoop and double-cone indenters, on the $(10\bar{1}0)$ plane for the $(10\bar{1}0)<11\bar{2}0>$ slip systems, is given in Tables 5.10 and 5.11 . The method of computation of the effective resolved shear stress for a specific slip system, on a given plane, is given in Appendix III .

TABLE 5.10

Effective resolved shear stress for $(10\bar{1}0)<11\bar{2}0>$ slip. $(10\bar{1}0)$ plane indented with the Knoop indenter.

θ (deg.) ± 1	λ (deg.) ± 1	ϕ (deg.) ± 1	$\frac{\cos\phi + \sin\gamma}{2}$	*E.R.S.S. $= \cos\phi . \cos\lambda . \frac{\cos\psi + \sin\gamma}{2}$
0	70	65	0.433	0.06
10	65	65	0.450	0.08
20	61	65	0.541	0.11
30	58	65	0.628	0.141
40	53	65	0.710	0.182
50	48	65	0.780	0.224
60	43	65	0.872	0.269
70	40	65	0.930	0.301
80	37	65	0.970	0.327
90	35	65	0.995	0.344

* Maximum values for each facet were averaged to give a resultant E.R.S.S.

TABLE 5.11

Effective resolved shear stress for $(0001)\langle 11\bar{2}0\rangle$ slip. $(10\bar{1}0)$ plane indented with the double cone indenter.

θ (deg.) ± 1	λ (deg.) ± 1	ϕ (deg.) ± 1	$\frac{\cos\phi + \sin\gamma}{2}$	E.R.S.S.
0	35	77	0.433	0.080
10	33	77	0.520	0.090
20	31	78	0.612	0.110
30	29	79	0.703	0.117
40	27	80	0.785	0.121
50	25	82	0.858	0.108
60	23	84	0.918	0.088
70	21	86	0.962	0.062
80	19	88	0.991	0.033
90	17	90	0.992	0.000

According to Daniels and Dunn's analysis of slip systems, on the basis of hardness anisotropy, maximum hardness should correspond to minimum effective resolved shear stress and vice versa. Application of the analysis, to a $(10\bar{1}0)$ plane, assuming that slip is possible on $\{10\bar{1}0\}\langle 11\bar{2}0\rangle$ systems, predicts the hardest and softest directions, on this plane, as $\langle 11\bar{2}0\rangle$ and $\langle 0001\rangle$, respectively. The hardness anisotropy for a $(10\bar{1}0)$ plane, (Fig. 5.14), is consistent with the predicted anisotropy. The computed effective resolved shear stress curves for the $(10\bar{1}0)$ plane for $(0001)\langle 11\bar{2}0\rangle$ slip systems, (Fig. 5.16), predict $\langle 11\bar{2}0\rangle$ and $\langle 0001\rangle$ directions as the softest and hardest directions, respectively, which is not true. Hence, slip on $(0001)\langle 11\bar{2}0\rangle$ does not occur.

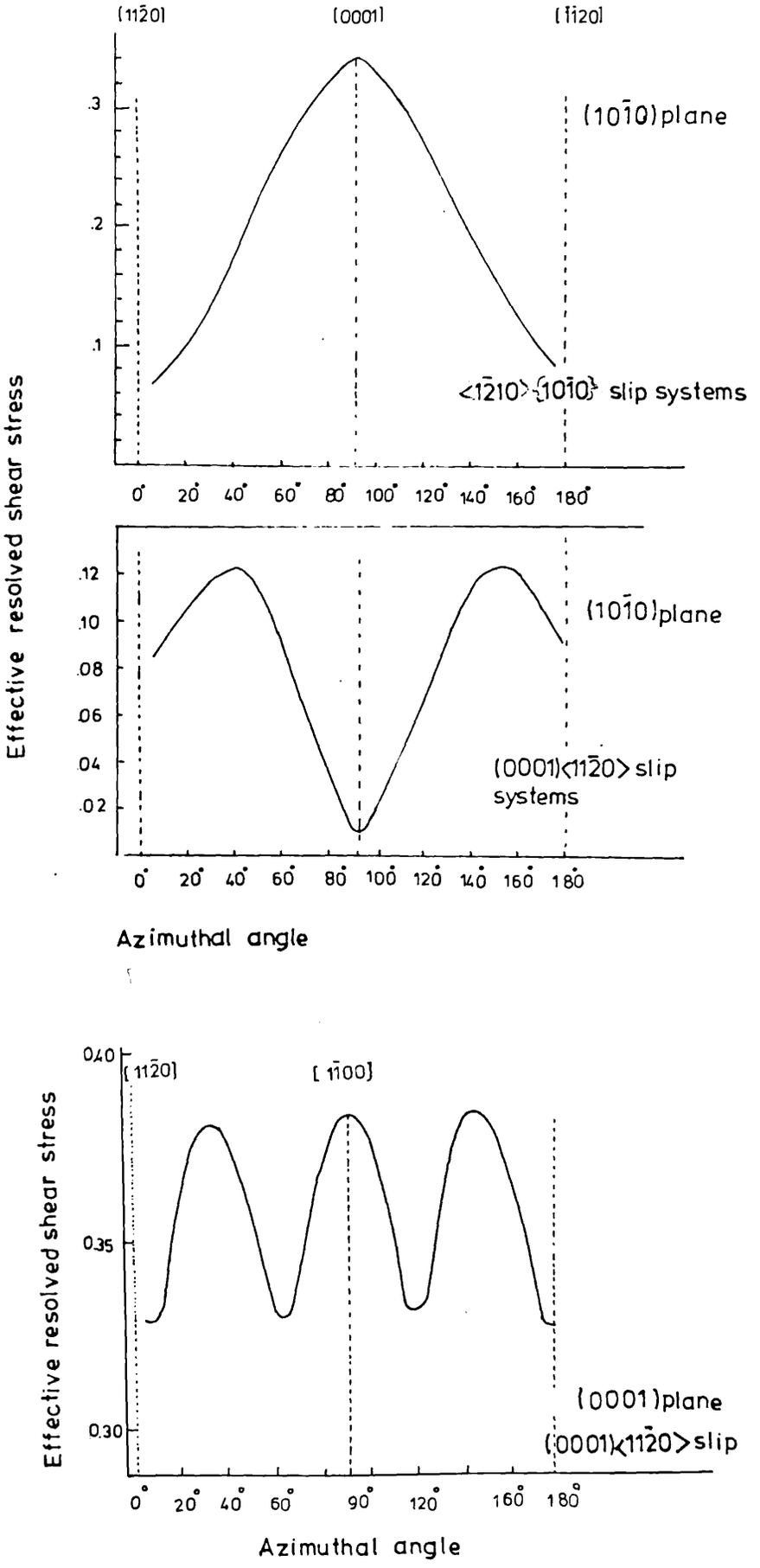
[11$\bar{2}$0]
[0001]
[$\bar{1}$$\bar{1}$20]
(10$\bar{1}$0)plane
<1$\bar{2}$10>{10$\bar{1}$0} slip systems
(10$\bar{1}$0)plane
(0001)<11$\bar{2}$0> slip systems
Effective resolved shear stress
Azimuthal angle
[11$\bar{2}$0]
[1$\bar{1}$00]
(0001)plane
(0001)<11$\bar{2}$0>slip
Effective resolved shear stress
Azimuthal angle

Fig. 5.16

The hardness curves for the $(10\bar{1}0)$ plane, in Fig. 5.14, suggest that, if Daniels and Dunn's analysis is correct, the dislocations had moved on $\{10\bar{1}0\}\langle 11\bar{2}0\rangle$ slip systems. It can be seen by comparing the hardness curves with the E.R.S.S. curves that the maxima of the hardness curves correspond with the minima of the E.R.S.S. curves. The prediction of the $\{10\bar{1}0\}\langle 11\bar{2}0\rangle$ slip systems is in agreement with the observation of slip lines, beneath the spherical and double-cone indenters, using optical and electron microscopy. It is a matter of some speculation, however, if the dislocations did in fact move, at room temperature, as a result of large indentation stresses, or whether they moved due to fracture following an indentation.

The hardness curve for (0001) plane, (Fig. 5.14), does not show well-defined maximum or minimum. Slip lines are, however, seen inside the hardness impressions on the basal plane, after annealing the specimen at a high temperature ($\sim 2000^{\circ}C$), (Fig. 5.25). It suggests that dislocations move on a secondary slip system $(0001)\langle 11\bar{2}0\rangle$. The E.R.S.S. curve for the basal plane is shown in Fig. 5.16 . According to the analysis of Daniels and Dunn, if the secondary slip system $(0001)\langle 11\bar{2}0\rangle$ is operating, the hardest direction on this plane should be $\langle 11\bar{2}0\rangle$. The results of hardness measurements on the basal plane of an annealed specimen (SiC type II), given in Table 5.8 , show that $\langle 11\bar{2}0\rangle$ is the hardest direction. In order to confirm the occurrence of the secondary system, at high temperatures, hardness tests should, however, be made on a specimen at these temperatures. It might then be possible to determine the hardness anisotropy on the basal plane and explain it on the basis of the effective resolved shear stress analysis of slip sytems .

5.10 Birefringence studies on hardness indentations

Thin, well-formed and transparent silicon carbide crystals (type II) were chosen for the birefringence experiments. Indentations were made with the Vickers indenter on the (0001) plane, with loads upto 1 kg. The Vickers projection microscope was used as an optical polariscope. Plane polarized light transmitted through the indented specimen was received by the analyzer located under the objective of the microscope. The resulting birefringence patterns were recorded on photographic plates.

Fig.5.17.a shows a birefringence pattern around a Vickers indentation with 1 kg load. The (0001) plane of the specimen is perpendicular to the beam of light. It means that the c-axis of the crystal corresponds to the optic axis.

The intensity of transmitted light, in a wing of a birefringence rosette, has been found to depend on the load with which the indentation was made. In other words, this intensity depends on the stresses causing the birefringence. An estimate of these stresses can, therefore, be made of by measuring the intensities of transmitted light. For this, the stress-optical constants for the test specimen must be known. As this information is not yet available for silicon carbide crystals, the analysis of the stresses due to indentation has been carried out from a qualitative point of view. An automatic recording microdensitometer (MK 111C) was used in this work to obtain intensity plots from the birefringence patterns. Figs.5.18 a-c show the birefringence patterns around the Vickers indentations with 500g load with the c-axis making

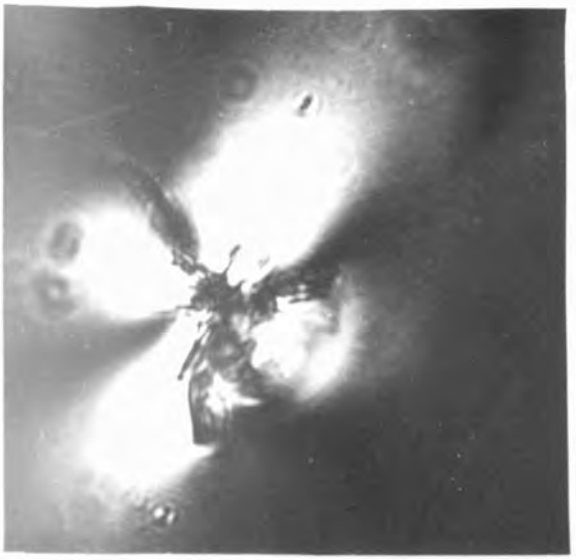

X 200

Fig. 5.17 a. Birefringence around Vickers indentations.

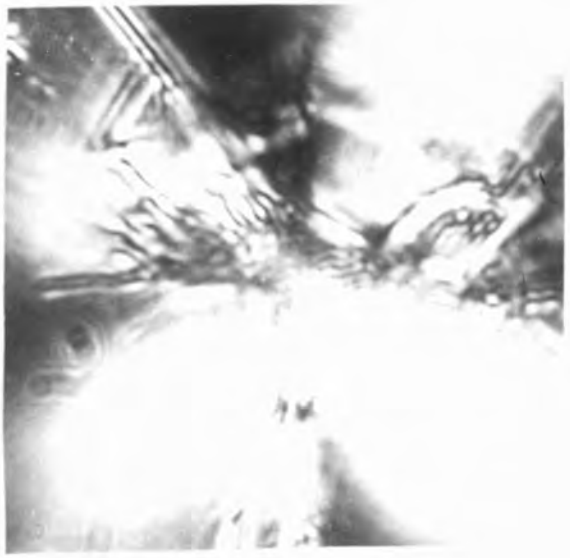

Fig. 5.17 b. Interference pattern within the birefringence rosette.

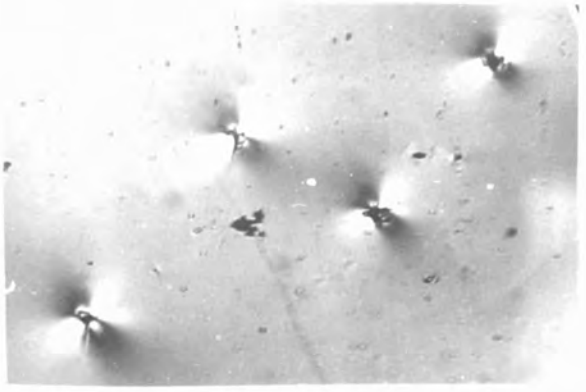

Fig 5.18 a.

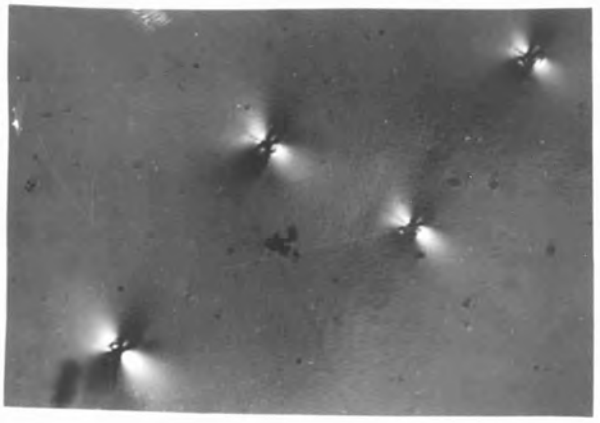

Fig.5.18 b.

Fig.5.18 c.

Birefringence around Vickers indentation
c-axis at a. b. & c. to the incident light.

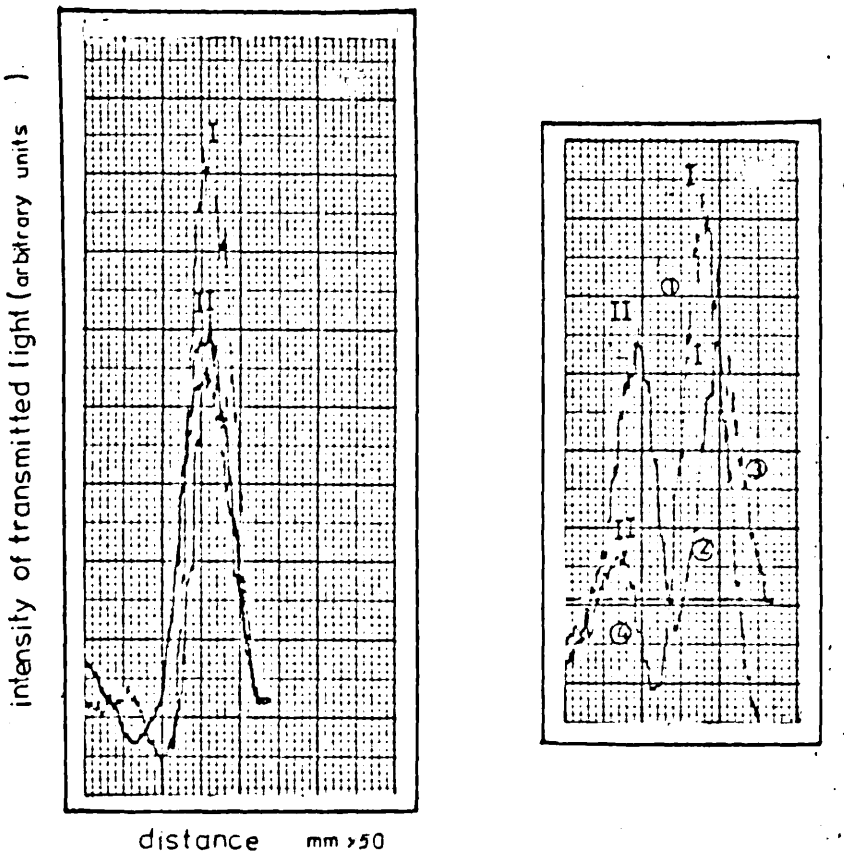

Fig.5.19 . Transmitted intensity distribution around an indentation. The (0001) plane of SiC crystal is at 0° to the crossed nicols.

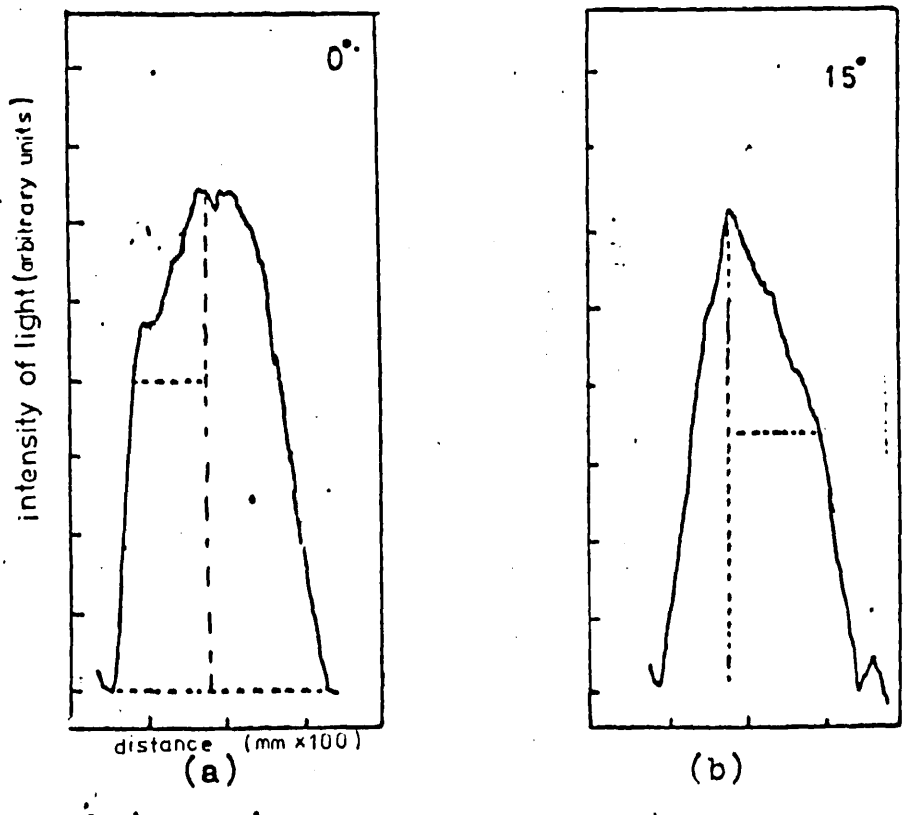

Figs. 5.20 (a-f). Intensity vs distance (mm × 100)

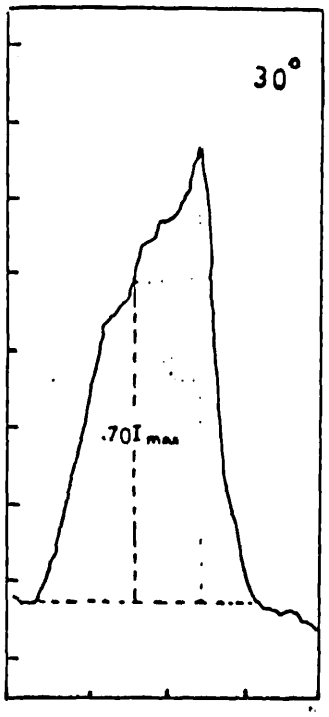

(c)

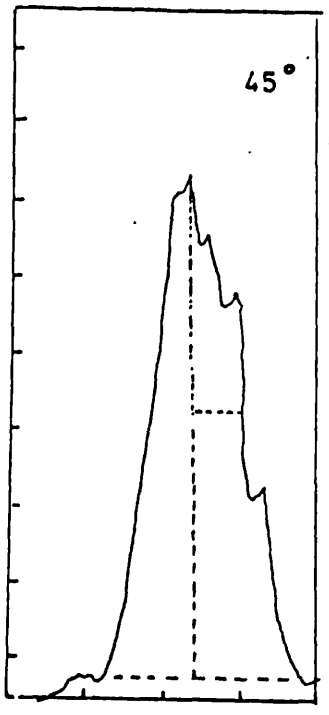

(d)

(e)

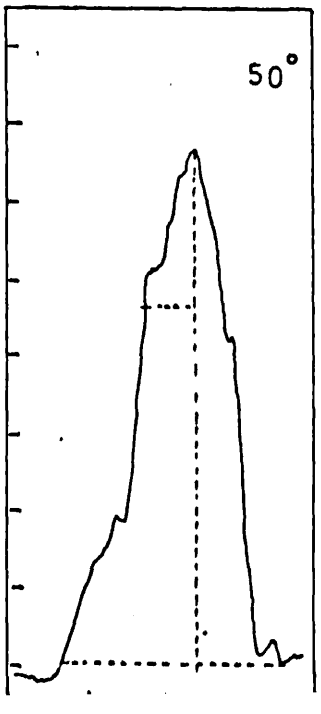

(f)

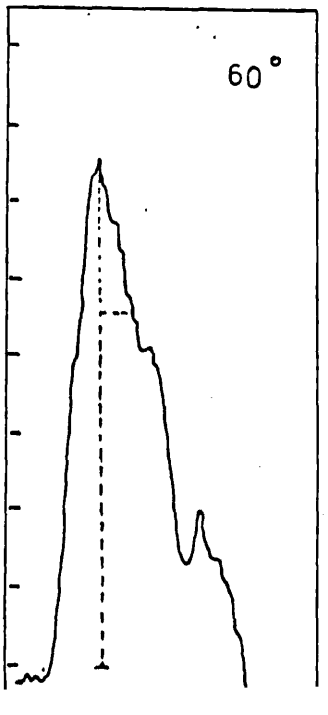

three different angles with the direction of the polarized light. Fig. 5.19 shows plots of transmitted intensities along the four wings of a birefringence rosette. Figs. 5.20 a-f show the distribution of the transmitted intensity along the diagonal axis of one of the four wings of the rosette at six different inclinations of the indented specimen with the polarized light.

A polar plot of equal transmitted intensities, as shown in Fig. 5.21 , is obtained by finding the distances between two points , along the diagonal of a wing , one at which the intensity is maximum and the other at which , say, 70 % of the maximum, and plotting these against the orientation of the c-axis with the polarized light . The dotted curve , in Fig. 5.21 , is the polar plot of equal stresses, beneath the spherical indenter , which follow the stress-optical law :

$$r^2 = K^2 . \cos^4\theta \qquad \text{(Section 4.4.1 equation 4.29)}$$

There is a good agreement between the contours of equal transmitted intensity and the stress-optical plots . This suggests that the equal intensities polar plots could be very useful in finding the distribution of principal stresses due to indentation .

5.10.1 Interference patterns inside the birefringence rosettes

It is of interest to note that the birefringence patterns , obtained by using a convergent light , are seen to contain dark and bright fringes , inside the wings , as seen in Fig. 5.17. b. When a converging beam is transmitted through a thin transparent specimen various path differences are introduced due to different rays of light. The loci of rays which have suffered a retardation of an integral number of wavelengths give rise to circular

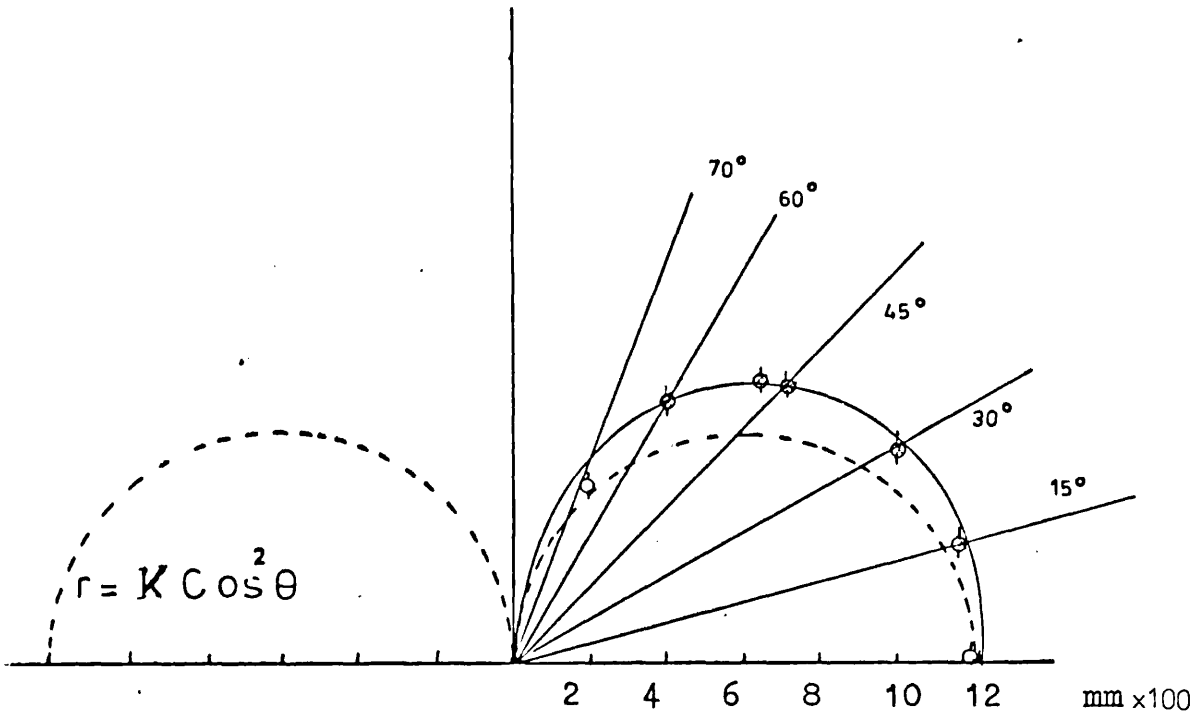

Fig. 5.21 .Polar plot of equal transmitted intensity, $(.7 * I_{max.})$ based on figs.5.20.(a) to (f).

fringes. It was noticed that the distance of a dark or bright fringe from the centre of the rosette increasesd linearly with the increase in load.

5.11 Interferometric study of the plastic flow around indentations

This section deals with the application of Tolansky's multiple-beam interferometry techniques to the study of the plastic flow around hardness indentations, particulary the indentations with the Vickers indenter.

Fizeau fringes were obtained by matching the indented area of the test specimen, after depositing a thin layer ($\sim$ 700 Å) of silver on the specimen in a vacuum evaporation plant, against a silvered optical flat (usally a thin glass slide) and using the green line of mercury (5461 Å). In order to find out whether the disturbance at a point, near an indentation, was a 'piling-up' or a 'sinking-in', fringes of equal chromatic order (F. E. C. O.) were obtained by projecting each Fizeau fringe around the indentation on the slit of a constant deviation spectrometer and replacing the monochromatic light by white light. A 'piling-up' bends the F. E. C. O. convex towards the violet whereas a 'sinking-in' bends them concave.

Fig. 5. 22 shows two-beam and Fizeau fringes around Vickers indentations with 1 kg load. These interferograms indicate that the distortion around the hardness impressions is asymmetric. There is a differential 'piling-up' along the boundary . Fig. 5. 22b shows that on one side of the impression the 'piling-up' is seven fringes and on the opposite side it is three fringes. The 'piling-up' on sides perpendicular to these two is four fringes. It is also obseved that the distortion in one direction from the top right corner of the Vickers impression extends to a distance more than the diagonal of the impression.

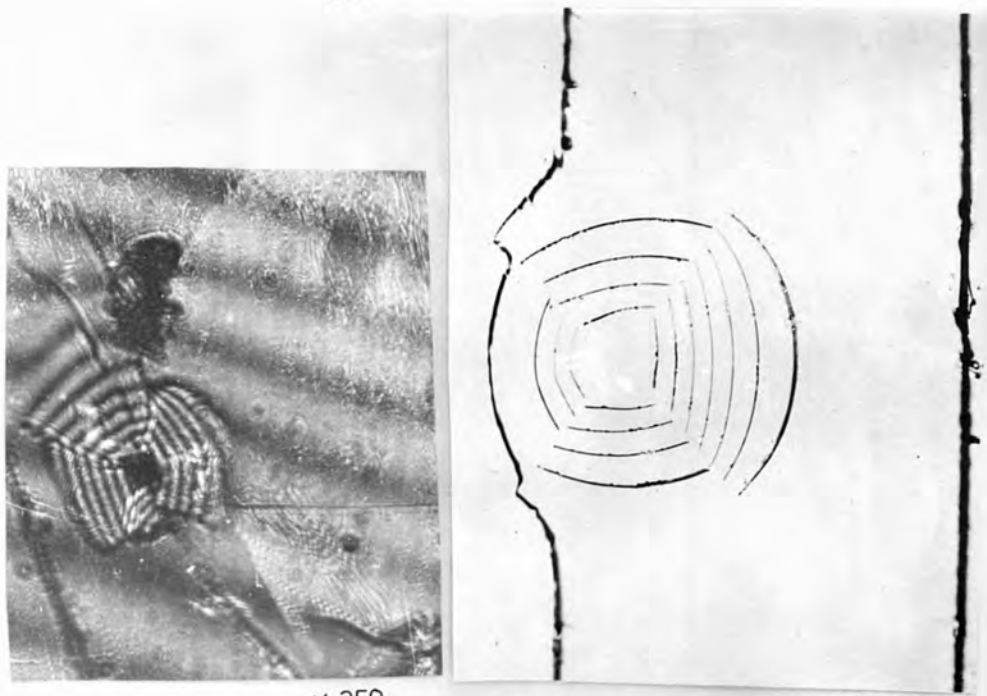

Fig. 5.22 . Interference fringes pattern around Vickers indentation
a) two beam fringes , b) Fizeau fringes.

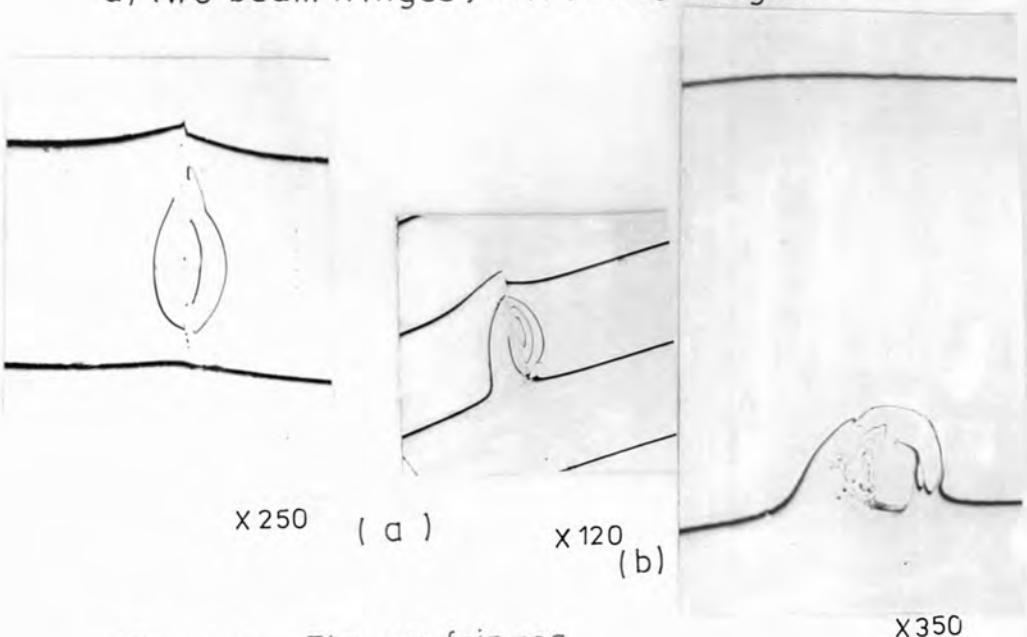

Fig . 5.23 . Fizeau fringes
a) around double cone indentation, b) around spherical indentation.

The indentations with double-cone and spherical indenters also produce an asymmetrical plastic flow as shown in Fig 5.23. . The distortion due to these indenters does not extend very far from the impressions. In the case of the double-cone indenter, the 'piling-up' extends to a distance less than the diagonal of the impression irrespective of its orientation on the surface of the specimen. The fringes around the double - cone impression bend inward as they approach its edges. This shows the way in which the flow rises and falls.

Fig. 5.24 shows the Fizeau fringes around a Vickers impression surrounded by F. E. C. O. interferograms. Such interferograms were obtained only for the curved Fizeau fringes which lie on the 'piling-up' or 'sinking-in' regions. The interferograms X_1Y_1 and X_3Y_3 show F. E. C. O. of the first and third Fizeau fringes, from right to left, respectively. Top first and second fringes, above the hardness impression, give rise to interferograms Y_1Z_1 and Y_2Z_2. The third fringe below the impression produces interferogram $Y'_1Z'_1$.

The fringes in interferograms X_1Y_1 , X_3Y_3 , Y_1Z_1 and Y_2Z_2 are convex towards violet end of the spectrum. The Fizeau fringes responsible for these, therefore, lie on the 'piling-up'. $X'_1Y'_1$, $X'_2Y'_2$ and $Y'_1Z'_1$ indicate the 'sinking-in', because the F. E. C. O. are concave towards violet.

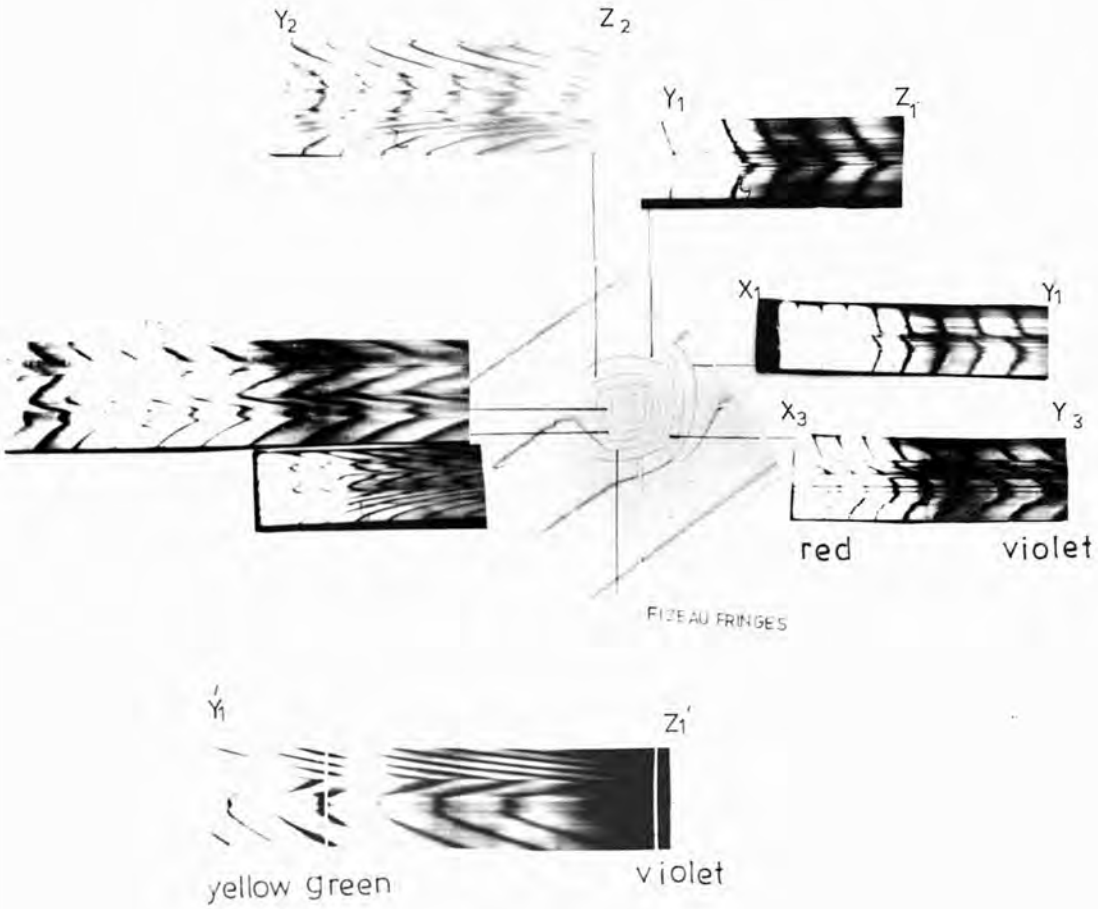

Fig. 5.24 Fringes (E.C.O) around a Vickers indentation, using white light.

5.12 Optical studies on plastic distortions due to hardness indentations

Steady pressures were applied to the basal plane (0001) and prismatic planes $(01\bar{1}0)$ of a test specimen using a spherical indenter with loads between 100g to 2 kg.

5.12.1 Observations on the basal plane of silicon carbide type II

Fig. 5.25 shows the microstructure inside an impression made with 1 kg load after annealing the test specimen at 2000°C for 30 minutes. Traces of slip lines are seen inside the impressions. These traces are along the $<11\bar{2}0>$ directions which happen to be the hardest directions. Their appearance is believed to be due to slip occuring on $(0001)<11\bar{2}0>$ systems. At higher loads, radial cracks also begin to appear as shown in Fig.5.26 and their number and length increases with load.

5.12.2 Observations on the prismatic plane $(10\bar{1}0)$

Fig.5.27 shows a hardness test indentation with 1 kg load on the spherical indenter. There are no radial cracks associated with the indentation. Parallel slip markings are seen inside the indentation. These are along the $<11\bar{2}0>$ directions. The effective resolved shear stress analysis of indentations on $(10\bar{1}0)$ plane shows that the operating slip system is $(\bar{1}010)<11\bar{2}0>$. The markings seen in Fig.5.27 are, therefore, believed to be due to slip taking place on the $\{10\bar{1}0\}$ planes, with $<11\bar{2}0>$ as a slip direction.

Fig.5.28 shows two hardness impressions with 1 kg load separated by 0.085 mm. Both contain slip markings in the $<11\bar{2}0>$ directions. A broad band of slip lines between them, in the $<0001>$ direction, was revealed by annealing at 2000°C. The appearance of slip lines, after annealing, suggests that a secondary slip system operates

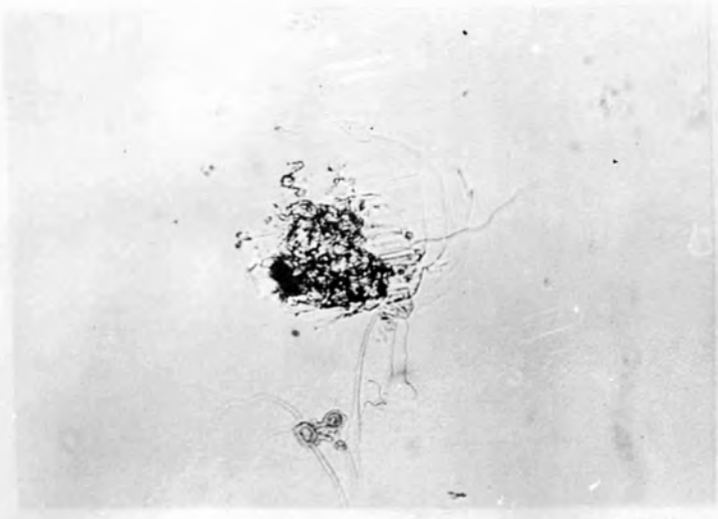

X 1100

Fig. 5.25 . Slip lines inside an indentation. (Load 1 kg on the spherical indenter.)

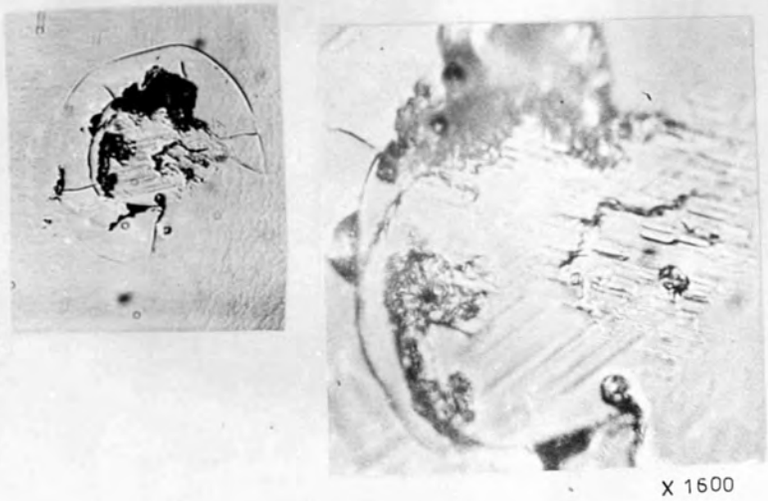

X 1600

Fig. 5.26. Slip lines inside an indentation obtained with 2 kg load on the spherical indenter.

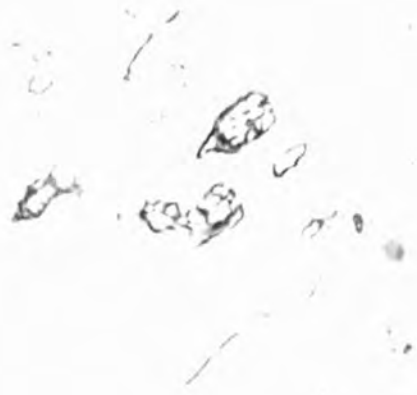

X1600

Fig. 5.27 .Microstructure inside an indentation with a spherical indenter. 1 kg load.

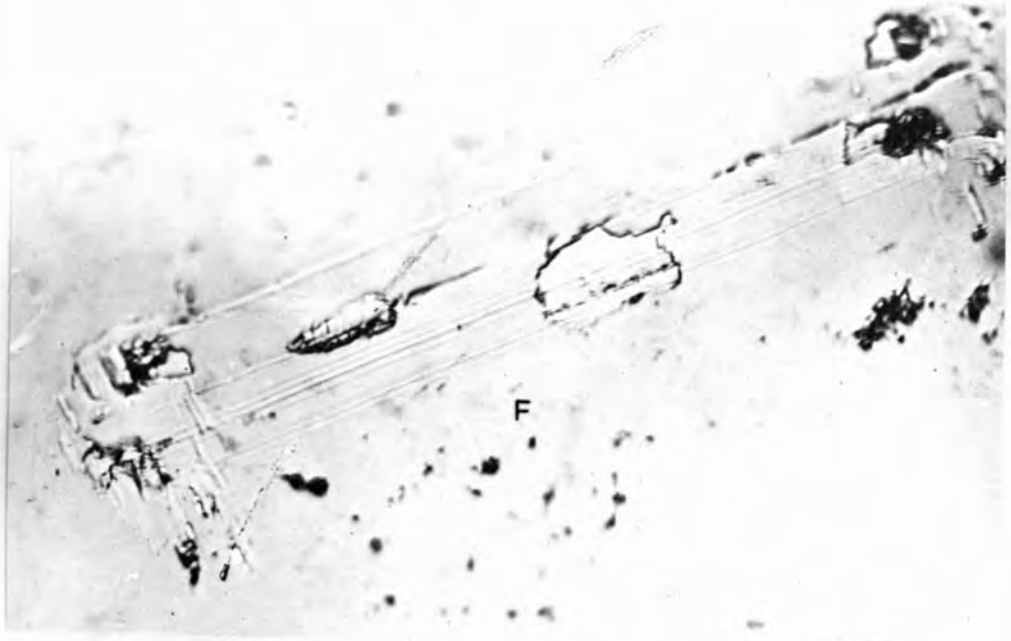

X1350

Fig. 5.28 . Slip lines on the $(10\bar{1}0)$ plane due to spherical indentations.

at high temperatures. This secondary slip system is believed to be $\{0001\}\langle 11\bar{2}0\rangle$. If this system is operating, then according to the E.R.S.S. curves for indentations on the prismatic planes, Fig. 5.16, the hardest direction is $[0001]$. The hardness anisotropy curves, Fig. 5.14, however, suggest that for the prismatic planes the hardest directions are along $\langle 11\bar{2}0\rangle$. It follows that the hardness anisotropy is reversed at high temperatures. This point needs further research by performing hot indentation tests.

The feature marked F, in Fig. 5.28, has a vertical axis of three-fold symmetry. The etching figures on a prismatic plane developed by fused borax on silicon carbide type II crystals are very much similar in general appearance to this feature. Its presence is significant from one point of view that it supports the goniometric finding of the test plane being a prismatic plane $(10\bar{1}0)$.

5.12.3 Observations on the pyramid plane $(10\bar{1}1)$ of SiC type I

Indentation studies were made on the pyramid faces of a rhombohedral crystal belonging to the space group $R\bar{3}m$. This was the only rhombohedral crystal available to us. This crystal had six well-developed pyramid faces $\{10\bar{1}0\}$ and two poorly formed pinacoid faces $\{0001\}$. This is a rare growth in silicon carbide type I crystals, as such a structure has not been reported in the literature on this material.

Fig. 5.29 shows slip lines around an indentation made with the spherical indenter, on the pyramid plane $(10\bar{1}1)$. Three sets of slip lines are clearly visible. There is a preference for 90°, 45° and 45° angles. The density of slip lines and thus the number

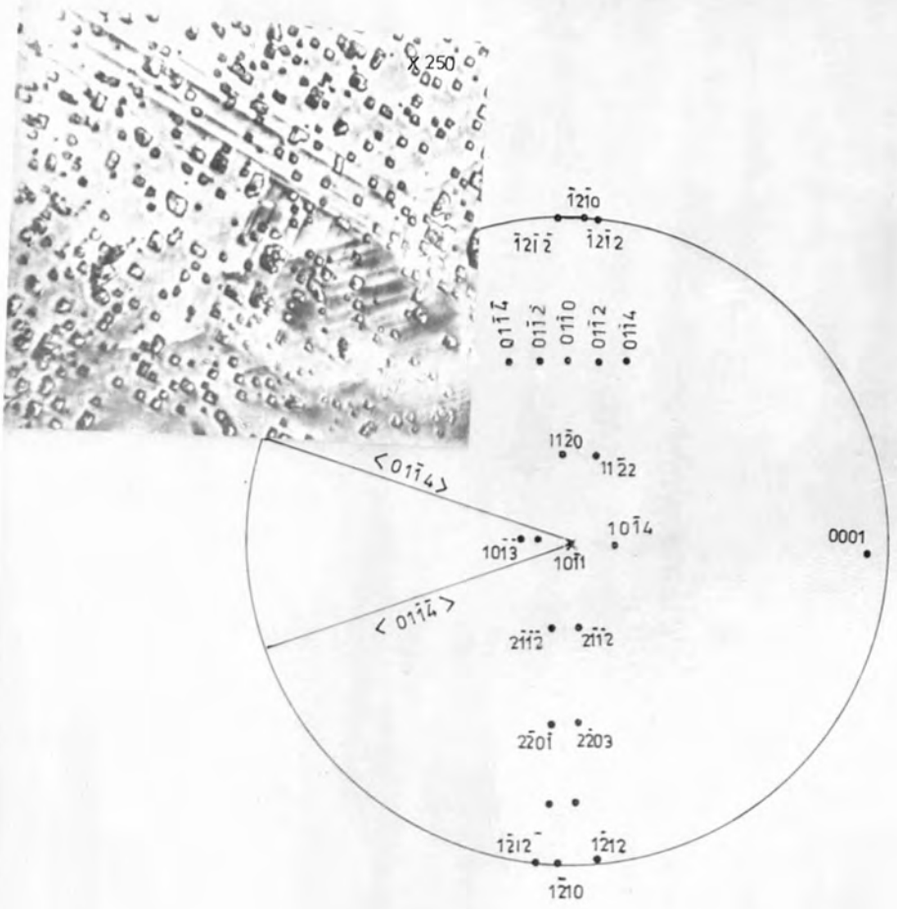

Fig.5.29 . Photomicrograph and stereographic projection of slip traces observed on $(10\bar{1}1)$ plane indented with a spherical indenter.

of active planes, which are found to be $(01\bar{1}4)$ planes, was found to increase with increase in load on the indenter.

The slip directions were determined from the analysis of the stereographic projection for the $(10\bar{1}1)$ plane. Slip systems found are the $(10\bar{1}1)<01\bar{1}4>$ systems.

5.13 Electron microscopic studies on indentations

Electron microscopy, using carbon replica technique, was applied to the studies of the microstructure, both inside and just outside the hardness test indentations. The microstructures inside the indentations are quite distinct from those outside the indentations. This is due to the fact that the stresses responsible for them are of different nature. The stresses beneath an indenter are predominantly compressive and outside the indentations they are mainly components of tensile stresses. The two kinds of microstructures have been described, separately, in the next sections.

5.13.1 Microstructure inside a Vickers indentation

Optical microscopy of hardness indentations with the spherical indenter revealed a characteristic slip pattern as described in Section 5.12 . The same examination, however, did not show slip associated with Vickers indentations. Careful preparation of carbon replicas of the hardness indentations and their examination in the electron microscope revealed faint discontinuous markings believed to be the slip lines. Such markings are visible on the basal plane only after annealing the specimen at high temperatures (above 1800°C).

Fig. 5.30 is a Vickers hardness impression obtained with 200 g load., on the basal plane. The microstructure consists of surface cracks. No evidence of plastic deformation is found. Figs. 5.31 and 5.32 show the microstructure inside an indentation with 200 g load after annealing the test specimen at 2000°C in the Plasma Torch for fifteen minutes. By analogy with the optical examination results of the spherical indenter's impressions, it follows that the lines seen in the electron micrograph (Fig.5.31), are along one of the slip directions $<11\bar{2}0>$. The hydrostatic stress produced by the Vickers indentation encourages slip, but for the slip to be visible on the basal plane a crystal has to be heated at a high temperature. This is because the dislocations in silicon carbide crystals are believed to move on the secondary slip systems at high temperatures.

5.13.2 Observations outside the Vickers indentations

Efforts to observe noticeable plastic deformation outside the Vickers indentations were not very successful. Of approximately one hundred indentations on different SiC type II crystals, using loads from 200 g to 1 kg, investigated by electron microscopy, none showed permanent deformation by slip.

Vickers indentations on one silicon carbide crystal, however, produced well-defined slip pattern on the basal plane. Scanning electron micrographs of the slip patterns, around a Vickers indentation with 1 kg , are shown in Fig.5.33 . Two sets of slip lines are observed on the (0001) plane which are inclind to each other at 60°. The slip lines are believed to belong to the secondary slip systems $\{0001\}<11\bar{2}0>$. Fig.5.34 is a scanning electron micrograph of the slip

3μ

Fig.5.30 . Electronmicrograph of Vickers indentation (Indentation load= 200 g.)

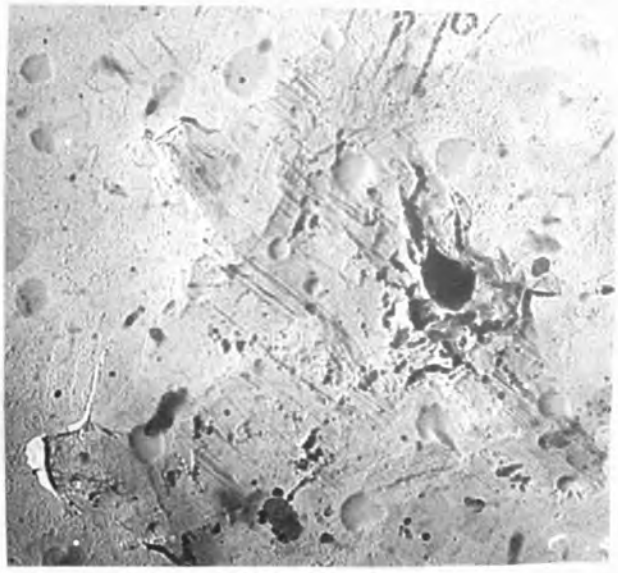

1.5μ

Fig.5.31 . Microstructure produced by the Vickers indenter Specimen annealed after indentation.

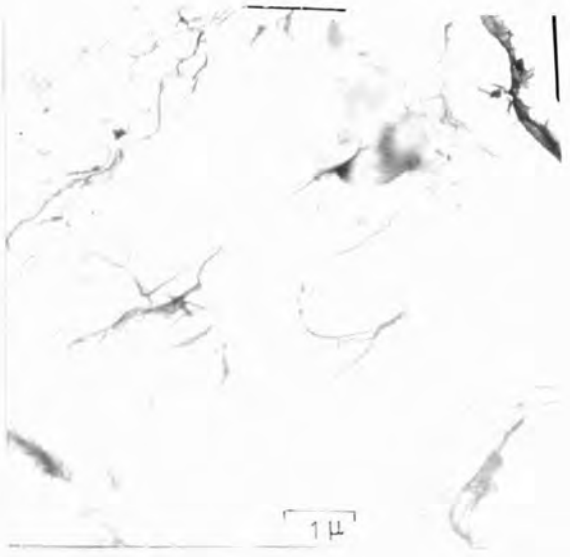

Fig.5.32 . Microstructure on the basal plane, inside the contact area between the crystal & the Vickers indenter (carbon replica).

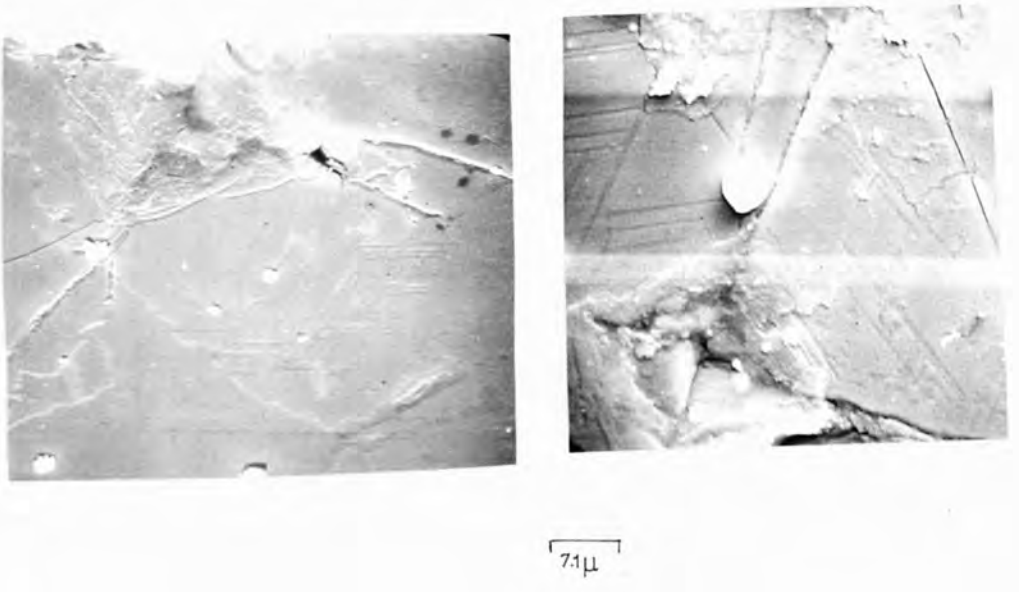

Fig.5.33 . Scanning electronmicrograph of slip around a Vickers indentation. (Load = 1kg)

patterns around a Vickers indentation on the same crystal , after annealing it in the Plasma Torch, for 15 minutes at 2000°C . The etch pits seen in this electron micrograph, which were not present before the heat treatment, are triangular , indicating a rhombohedral intergrowth . Fig. 5.35 is a stereographic projection of the crystal on the (0001) plane with the slip pattern inset . According to this projection, the slip lines are along $<11\bar{2}0>$.

The X-ray energy dispersive technique of scanning electron microscopy was applied to examine the compositional homgeneity in the crystal showing the slip pattern around the indentations. For this, a number of silicon and carbon images of the indented plane , from areas inside and outside the indentations , were compared . Fig. 5.36.a. shows silicon image scan of the test plane. No surface contamination or inclusions are seen in this scan . Fig. 5.36.b. is also a silicon image photograph , from an area containing a Vickers indentation. This area is also free from any bulk impurity. The differential contrast, in the scan , is believed to be due to the silicon rich area due to the 'piling-up'.

The X-ray diffraction analysis, by taking a Laue transmission photograph, (Fig. 3. Appendix IV), however, showed that the crystal has a strong component of SiC type I. This is evident from the three-fold symmetry in the diffraction pattern.

The appearance of slip lines, outside the hardness indentations, indicates that the plastic deformation zone , which is localized beneath the indenter in other specimens of silicon carbide, extends beyond the contact area in this test sample. The intergrowth of type I structure in type II, therefore, appears to modify the deformation characteristics of the latter.

Fig.5.34 . Slip lines and etch pits revealed by thermal etching in the plasma torch

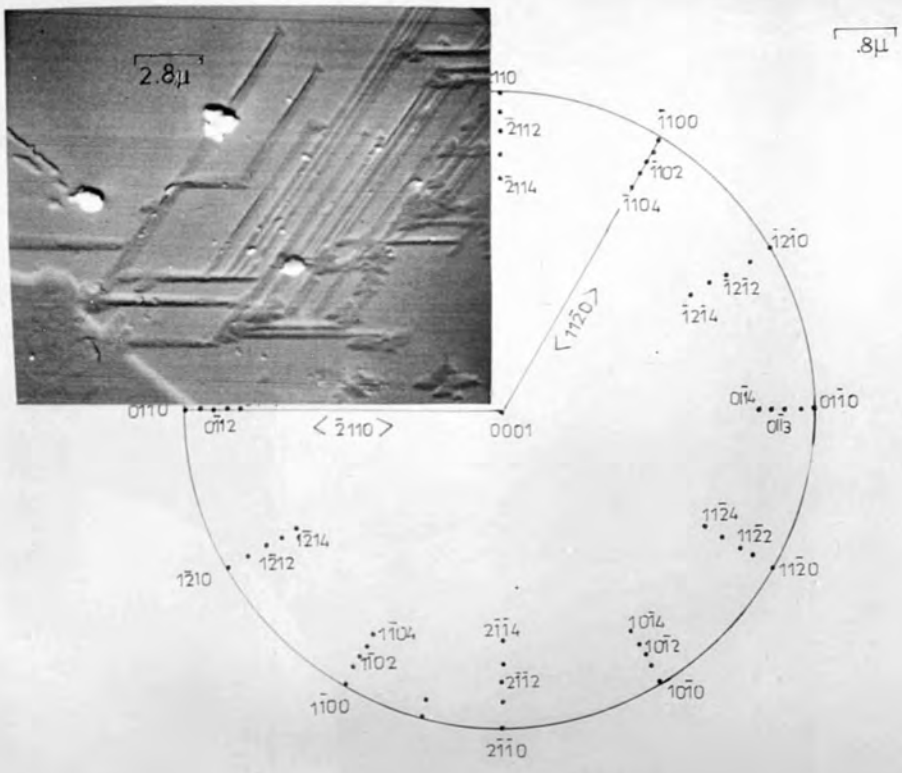

Fig. 5.35 . Stereographic projection [on (0001) plane for SiC (15 R)] & scanning electronmicrograph showing slip lines around a Vickers indentation.

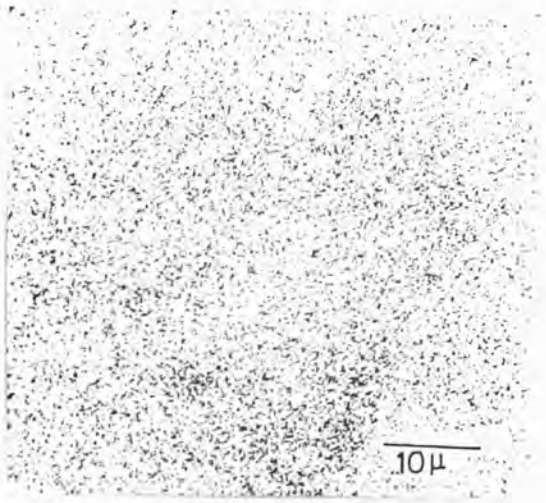

Fig.536(a) Silicon image of 0001 plane

Fig. 536(b) Silicon image of area around the Vickers indentation.

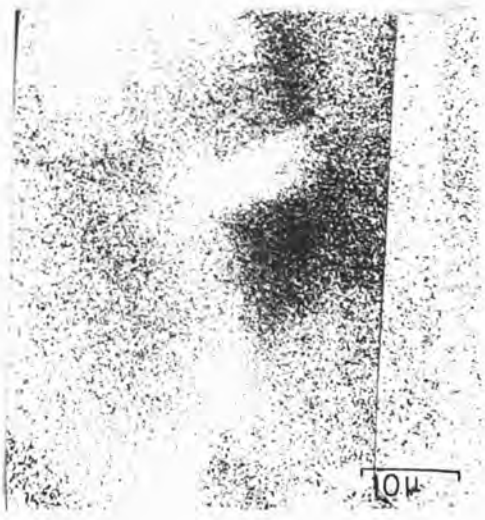

5.13.3 Microstructure inside the double-cone indentations on the basal and prismatic planes of silicon carbide crystals type II

Basal plane. Whereas, cracking is a dominant factor in Vickers indentations, it is not quite so in double-cone indentations. Double-cone indentations, without cracks, can be made using low loads. The incipient cracking is visible at about 200 g load by scanning electron microscopy. Fig. 5.37 shows optical and scanning electron micrographs of the double-cone indentations with 500 g load. The microstructure inside the indentation is mostly the debris due to surface damage by the indentation. Fig. 5.38 is an electron micrograph of the carbon replica of a double-cone indentation with 500 g load. There is no evidence of plastic deformation.

Prismatic plane. Features resembling slip lines were commonly seen in the electron micrographs of the double-cone indentations. Figs. 5.39 and 5.40 show the slip activity inside the indentations on two different crystals. There is, thus, a strong evidence of the plastic deformation of silicon carbide at room temperature. From the directions of the slip lines, it is appears that the slip occurs on the $\{10\bar{1}0\}\langle 11\bar{2}0\rangle$ slip systems.

5.13.4 Microstructure inside the d. c indentations on the (0001) plane of silicon carbide type I

Electron micrograph of a double-cone indentation with 300 g load is shown in Fig. 5.41. The microstructure, inside the indentation, was revealed by annealing the crystal and was not seen before it. It contains traces of slip and microcracks.

Fig. 5.42 shows a growth feature on the indented plane.

It has six sides with three longer sides alternating with three shorter sides. Similar features were observed by Espig[196] on the basal pinacoids of silicon carbide type I crystals after etching the crystals with a melt of K_2CO_3 and KNO_3 (2:1). In appearance the test specimen is like a hexagonal crystal, but this feature, and the shape of the etch pits seen after etching it, classify it as a rhombohedral crystal.

5.14 Optical and electron microscopic studies on indentation induced microcracking.

In order to fully explore the general characteristics of crack formation, it was considered important to study the microcracking induced by indenters of different shapes, by both optical and electron microscopy techniques.

5.14.1 Optical studies on ring cracks due to spherical indentations.

Surface cracking due to spherical indentations, in diamond [Tolansky[45]], germanium [Pugh[57]; Johnson[58]] or in some crystals with zincblende structure [Allen[197]], are in the form of near-polygonal surface traces. These traces are commonly known as the ring cracks.

Fig. 5.43 shows a ring crack around a spherical indentation with 200 g load, on the (0001) plane of a SiC type II crystal. It was revealed by etching the crystal with borax at 1000°C. Fig. 5.44 shows a hardness indentation with the spherical indenter at 1 kg load. The ring cracks follow a path somewhat eccentric to the contact circle. The crack starts at a point near the contact circle and runs around to complete itself on the opposite side. If the load on the indenter is increased further, the crack starts propagating downward as explained in Section 4.3.2 (Fig. 4.4).

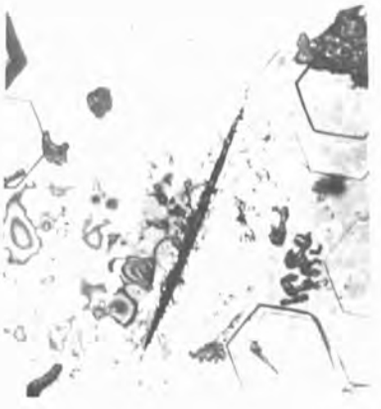

X 650

X 3500

Fig. 5.37

Optical & scanning electron micrographs of double cone indentations.

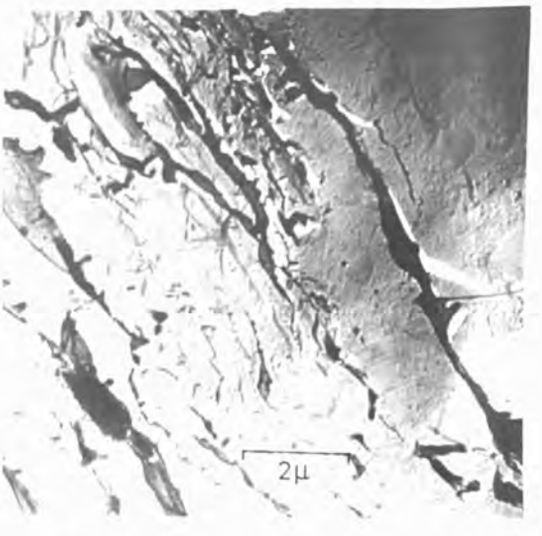

Load ½ kg

Fig. 5.38 . Electronmicrograph of a double cone indentation (carbon replica).

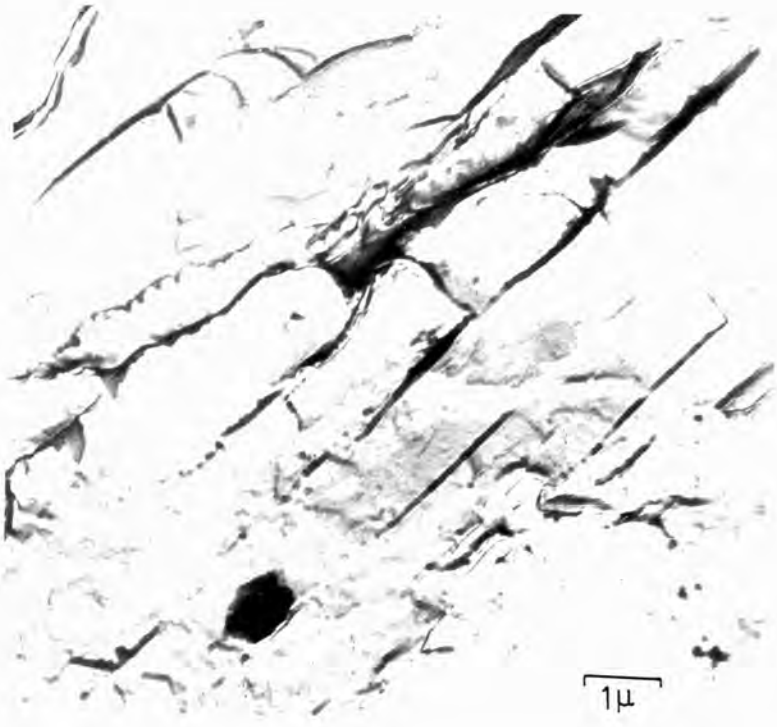

Fig.5.39 .Electronmicrograph of a double cone indentation.

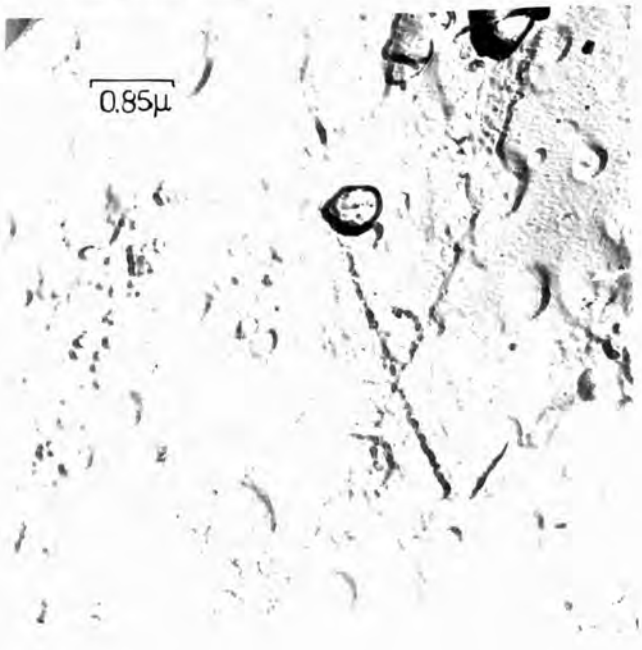

Fig. 5.40 . Trace of slip lines inside a double cone indentation.

Fig. 5.41 . River_like slip pattern on (0001) inside a double-cone indentation.

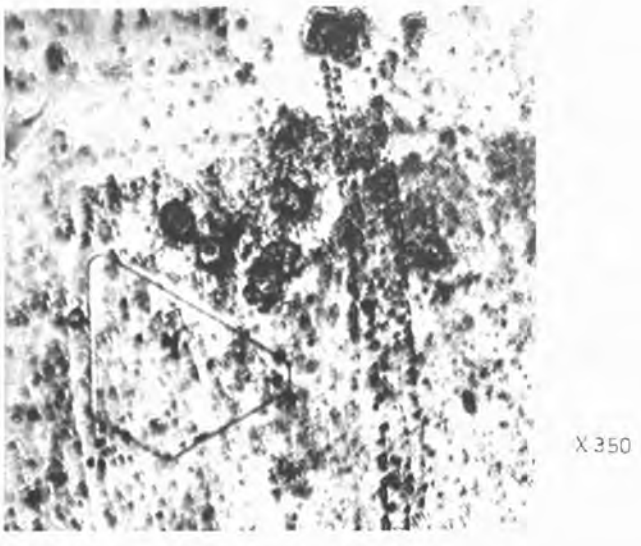

Fig. 5.42 . Growth feature on 0001 plane of SiC (15R).

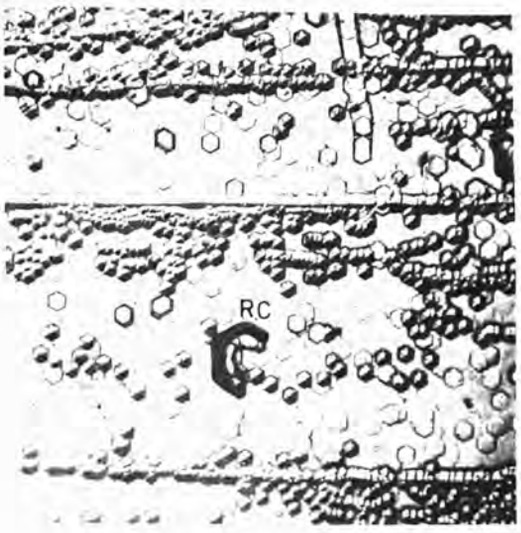

Fig. 5.43 .Ring crack around a spherical indentation made with 200g load, revealed by etching.

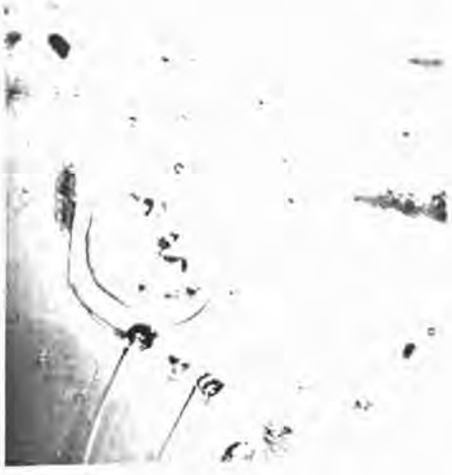

Fig.5.44 . Ring crack around a spherical indentation. (Indenter load = 1kg.)

5.14.2 Cracks around Vickers indentations

Cracks extending radially outward from corners of Vickers indentations are readily observable using a metallurgical microscope. An optical examination of the indentations shows that the number as well as the length of the radial cracks increases with increase in load on the indenter. These cracks have been termed as the median vents in the literature.

In addition to the median vents, cracks also appear along the sides of the hardness impressions. These additional cracks are commonly known as the lateral vents. (The formation of median and lateral vents has been explained in Appendix V .) The lateral vents are not easily observable in an optical microscope. The method of selective etching and electron microscopy have been found to be successful in revealing the lateral vents associated with indentations even at low loads.

A silicon carbide crystal type II was indented with 200 g, 500 g, and 1kg loads. No lateral vents were seen when the test sample was examined in an optical microscope. The crystal was etched with KNO_3 at 700°C for three minutes and re-examined in the microscope. Lateral vents around the indentations become visible at low magnifications. Figs. 5.45a-c show the lateral vents which look like lobes around three different Vickers indentations. made with 200 g, 500 g, 1 kg loads respectively.

Fig. .a. 200g load.

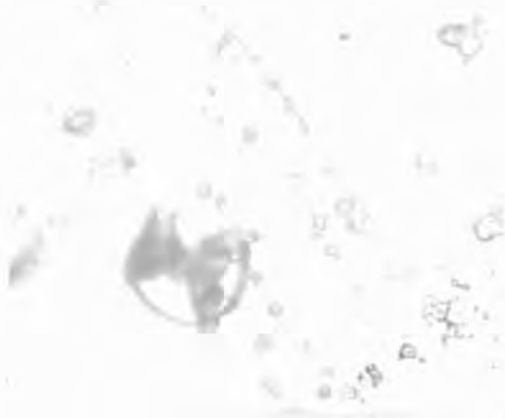

X100

Fig. .b. 500g load.

X100

Fig. .c. 1kg load.

X100

Fig. 5.45

Lateral vents around Vickers indentations, revealed by etching.

Fig. 5.47. Lateral vents around Vickers indentation. (Carbon replica)

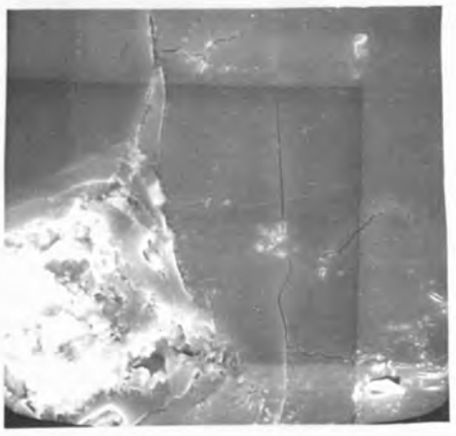

Fig. 5.48. Scanning electronmicrograph of a lateral vent around a Vickers indentation.

Both carbon replica electron microscopy and scanning electron microscopy revealed the lateral vents associated with Vickers indentations which were undetected by optical microscopy unless the crystals were etched after the indentation.

Fig. 5.46 shows the lateral vents around a corner of a Vickers indentation. The number of the lateral vents was found to increase with load on the indenter. Fig.5.47 is a scanning electron micrograph showing the lateral vents around a Vickers indentation, with 1 kg load.

5.14.3 Lateral vents around double-cone indentation

One notable difference between the lateral vents associated with double-cone indentations and Vickers indentations was found to be that of shape and dimensions. The lateral vents around the double-cone indentations are wider and longer than those around the Vickers indentations.

Fig. 5.48 shows two electron micrographs of two double-cone indentations with 1 kg load. The vents form fully developed lobes around the hardness impressions.

It was found that the interfacial separation in the lateral vents of the double cone indentations was wider than in the lateral vents of the Vickers indentations. The incidence of the lateral vents of these two types of indentations was not much different.

Fig. 5.48 .Electronmicrographs of fully developed lateral vents around double-cone indentations.

Fig. 5.48 shows asymmetry in the lateral crack pattern which is believed to be due to inclined or skew indentation. This happens when the load axis is not perpendicular to the plane of the test specimen. The lateral vents were seen to extend when indentations were made with bigger loads. They look like lobes around the hardness indentations as shown in this figure.

5.15 Cracks due to slight sliding movement of the indenter

A slight disturbance in the shear stresses beneath an indenter, such as due to a small movement of a loaded indenter against the surface of the test sample, was noticed to produce cleavage, slip, and wear track . Fig. 5.49 shows the microstructure produced by sliding a diamond ball indenter along a $<11\bar{2}0>$ direction on a $(10\bar{1}0)$ plane of a SiC type II crystal. It consists of slip lines, along the direction of motion of the indenter (left to right and parallel to $<11\bar{2}0>$), and cleavage cracks. The cleavage cracks intersect the track and the slip lines at 30° degrees. The relative orientation of the slip and /or cleavage planes to the wear track can play a significant role in determining the nature of the associated deformation. The results of this work are insufficient to formulate a theory of deformation. A more detailed investigation must be carried out in which the shape of the indenter, in particular among other things, is taken into consideration.

Fig. 5.50 is an electron micrograph showing etch figures (etching carried out with K_2CO_3 at $750^{\circ}C$) of the cleavage cracks produced by sliding. These figures have certain preferred crystallographic tendencies.

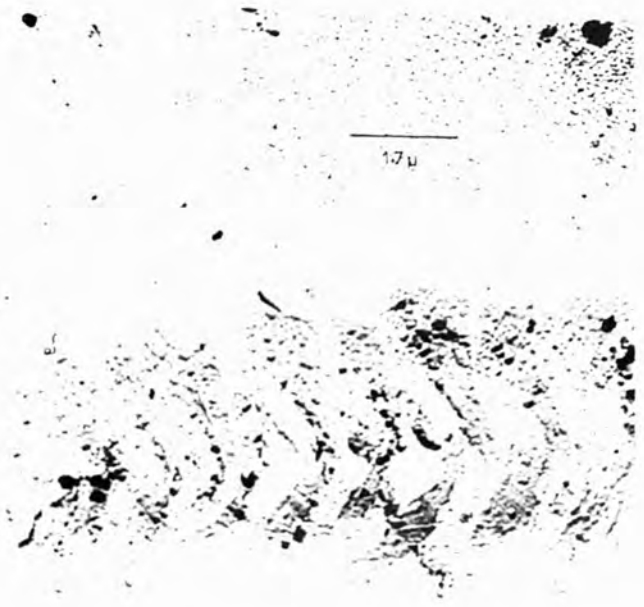

Fig. 5.49 . Electronmicrograph of etched surface showing cleavage cracks produced by sliding the spherical indenter.

Fig. 5.50 . Slip lines & cleavage cracks produced by sliding the spherical indenter in contact with the (0001) plane .

CHAPTER VI

DISCUSSION AND CONCLUSIONS

6.1 Directional hardness anisotropy

Most metallic and non-metallic single crystals exhibit directional hardness anisotropy. Different explanations, for example, twinning, cleavage, piling-up and dislocation motion, have been put forward, to interpret this anisotropy, but in some cases none of these has been able to completely account for the anisotropy.

Previous studies [Winchell[93]; Kohn[198]; Stern[199]; Shriramurty[101]; Shaffer[78]] have shown that silicon carbide crystals possess directional hardness anisotropy. Shaffer, on the basis of hardness determination in only two directions viz. $<10\bar{1}0>$ and $<11\bar{2}0>$, on the basal plane, concluded that the softest direction was parallel to the cleavage plane $(10\bar{1}0)$. The fact that cleavage in SiC has also been noted along $(11\bar{2}0)$ faces by Keyes[200], though less frequent than along the $(10\bar{1}0)$ planes, makes it impossible to correlate cleavage with hardness.

As the hardness anisotropy cannot be accounted for by cleavage, it means that other factors are responsible for it. It is suggested, because of similarity in hardness curves and slip systems for h. c. p crystal structures, such as Al_2O_3, that plastic flow within the crystal controls the anisotropy. The validity of this statement can be checked by Daniels and Dunn's analysis to this problem.

Before attempting to account for the hardness anisotropy in SiC, on the basis of Daniels and Dunn's analysis, it was considered essential to determine it with better experimental techniques, because hardness numbers reported in literature show a

large divergence. Shaffer[78] has reported anisotropy of only 1.2% for the basal planes. Shriramurty[101] determined this anisotropy as 39.8%. The present experiment was designed to find out whether the technique of measurement, of the diagonal lengths of the hardness impressions was responsible for the wide variation in hardness. In one hardness test, the diagonal length of a double-cone indentation with 200 g load, was found to be 56μ, using a 70x oil immersion objective. The length of the same indentation from a scanning electron micrograph of this indentation was 57μ. If the latter is regarded as the correct length, the difference between the two would alone be responsible for a hardness difference of ~6%.

We determined the hardness anisotropies using low loads, to avoid large cracking at the corners of the indentations, and measured the lengths of the hardness impressions from the scanning electron micrographs.

6.2 Correlation between observed anisotropy in hardness and the effective resolved shear stress E.R.S.S.

There are generally two slip systems which can operate in h.c.p. crystals. i.e. the systems $\{10\bar{1}0\}<11\bar{2}0>$ and $\{0001\}<11\bar{2}0>$. The system that operates, in a particular crystal, depends upon whether c_o/a_o ratio is less than or greater than the critical value 1.63, of the close packing of spheres. Table 6.1 gives examples of both the systems operating. The basal planes of all the crystals listed, in this table, show very small hardness anisotropy. It may also be noted that for the crystals deforming on the $\{0001\}<11\bar{2}0>$ slip systems the hardest direction on the $(10\bar{1}0)$ planes is $<0001>$, whereas those deforming on the $\{10\bar{1}0\}<11\bar{2}0>$ slip systems, the hardest direction

TABLE 6.1

Crystal	c_o / a_o	Knoop hardness number ($kg.mm^{-2}$)						Slip systems controlling hardness at room temp.	Reference
		(0001)		($10\bar{1}0$)		($11\bar{2}0$)			
		$<10\bar{1}0>$	$<11\bar{2}0>$	$<0001>$	$<11\bar{2}0>$	$<0001>$	$<10\bar{1}0>$		
Ti	1.587	117	117	56	131	-	-	$(10\bar{1}0)\ <11\bar{2}0>$	(201) Feng & Elbaum
Mg	1.623	28	24	36	15	-	-	$(0001)\ <11\bar{2}0>$	(202) Partridge et al
Zn	1.856	18	15	44	24	-	-	"	(94) Daniels and Dunn
SiC II	4.908	2917	2954	2027	2700	2321	2755	$(10\bar{1}0)\ <11\bar{2}0>$	Shaffer (78)
SiC II		2886	2904	1870	2290	-	-	"	Present work
Mo_2C	1.573	1580	1540	-	-	-	-	$(0001)\ <11\bar{2}0>$	(203) Vahldiek and Mersol

is along $<11\bar{2}0>$. The microhardness anisotropy on the (0001) plane of silicon carbide type II crystals is very small (~3.8%), and it has been found to remain unchanged if the slip system changes. The hardest direction, on the basal plane, is always the close packed $<11\bar{2}0>$ direction. Optical examination of the crystals, indented at room temperature, did not reveal any slip activity, whether inside or outside the hardness test indentations. This could either mean no dislocation motion at all or dislocation motion parallel to the indented surface, with a Bullough-Gilman type interaction.[204] (See Fig. 6.1). If the latter was correct, there would have been a conchoidal fracture around almost all the indentations. This type of fracture was not observed around any of the indentations.

It may be seen, by comparing the E.R.S.S. curves for $\{10\bar{1}0\}<11\bar{2}0>$ and $\{0001\}<11\bar{2}0>$ slip systems, for the $(10\bar{1}0)$ plane, (Fig. 5.16), that converse anisotropies are predicted depending on which slip system works. The highest Knoop (or double-cone) hardness number corresponds to the lowest E.R.S.S. for slip on $\{10\bar{1}0\}<11\bar{2}0>$ systems.

6.3 Effect of annealing on microhardness

It is obvious that the irregularities, in the structure of the material under a test, would affect its hardness, because they tend to resist the deformation of the material. Two kinds of structural irregularities, in the crystalline matter, are common, viz., the point defects and dislocations. In covalent crystals, such as germanium, silicon, silicon carbide etc., the dislocations have been found to have some effect on the microhardness of these crystals. Dale and Price[205] found a big difference in the microhardness between dislocation free

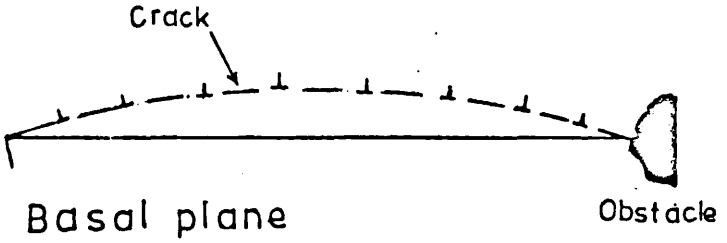

Fracture initiated by a queue of dislocations

Fig. 6.1.

germanium (500 kg. mm^{-2}) and germanium with various dislocation densities; for instance, germanium which contained approximately 10^3 cm^{-2} dislocations had a hardness number 600 kg. mm^{-2}, while one having 10^6 cm^{-2} dislocation density showed a hardness number 700 kg. mm^{-2}. Mil'vidskii et al.(206) found an increase of dislocation density in silicon crystals by one order of magnitude (from 10^3 to 2×10^4 cm^{-2}) resulted in increase of hardness from 830 to 1250 kg. mm^{-2}.

Heating a crystalline solid to a high temperature can modify those properties which are related to dislocations. At high temperatures, dislocations will move inside it, so as to redistribute the stored elastic energy or relieve any strain hardening. It seems that the observed decrease of hardness (or of the internal hardening stresses = $d\rho$) is, $\frac{d\rho}{dt} = -\text{const.} \times \frac{v}{d}$,

where v is the climb velocity of dislocations, d is the distance they have to move in order to be eliminated and t is the anneal time. Since $\frac{v}{d}$ increases with temperature, therefore, during a given course of time, the hardness should decrease with increase in temperature.

Considering the climb of dislocations, it has been shown(207) that the reduction in hardness or in internal hardening stresses is given by,

$$\frac{d\rho}{dt} = -\text{const.} \times \frac{\rho^3}{kT} \exp -U/kT$$

where U is the activation energy of self diffusion and is equal to the sum of the energy required to create a vacancy and the energy necessary to make it jump. Integration of this equation leads to

$$\frac{1}{\rho^2} = A - Bt ,$$

where A and B are constants. Long annealing times should, therefore, result in reductions in hardness values.

Cross slip can also reduce the internal hardening stresses, but this usually occurs in low temperature anneals of certain face centred cubic metals and hexagonal packed polycrystals.

The point of view developed in the preceding paragraphs is now applied to the particular case of silicon carbide crystals. The density of dislocations in silicon carbide (typeII or 6H) crystals is generally very low (1 - 100 cm^{-2}) but it may be as large as 10^4 cm^{-2} due to plastic deformation. Dislocations introduced into a crystal during deformation can harden the crystal by increasing the internal stresses. The hardening expected from this process is related to the average dislocation density and falls fairly easily as a result of annealing.

It is admitted that this is only an oversimplified approach, because a detailed description of the processes involved is still uncertain. The present results, therefore, only qualitatively characterize the effect of annealing on the hardness. It is finally exphasized that for a true hardness value from the indentations on a given crystal, specially the one prepared by grinding and polishing, the test sample should be annealed to a high temperature to eliminate the dislocations.

6.4 Plasticity of SiC

The appearance of slip inside the double-cone indentations, on the prismatic planes, without visible fracture,(Figs. 5.39 and 5.40), strongly suggest the possibility of plastic deformation of silicon carbide type II crystals at room temperature .

Previous investigators,[199] (Stern and Shaffer[78]), who made hardness tests on these planes have not reported signs of slipping. It is probably due to their specific interest, which was to find the hardness number only. Moreover, the slip lines are not very pronounced in low load indentations and cannot be seen using optical microscopy. As these investigators used conventional microscopy, it seems that these features must have remained unnoticed.

The plasticity of SiC crystals, which we have found on the basis of the slip lines inside hardness impressions, does not appear when standard compression of flexion tests are used. Hasselman and Batha[208] attempted to deform single crystal platelets, by high temperature creep in three-point bending at 1750°C. They did not observe any bulk deformation. The plasticity of some monocarbides in GroupIV and V with NaCl structure, viz., TiC, ZrC and NbC was observed by Williams[209], at temperatures above 1000°C. The poor plasticity of these compounds has been attributed to the fact that they have bonds of covalent type as in germanium and silicon, which become plastic at high temperatures. The Si-C bond is mainly covalent. The mobility of dislocations in covalent crystals is governed by the presence of extremely intense Peierls - Nabarro forces. These forces can be overcome by the application of large shear stresses. It is known (Bowden et al.[210]) that large pressures and shear stresses are produced locally beneath indenters. Recently, Carroll and Tanaka[63] have demonstrated the room temperature plasticity of germanium by Knoop indentations.

6.5 Slip lines and slip directions

In both the structures SiC type I and SiC type II the most compact plane is (0001), (see Table 6.2). The slip system which is very probable in the compact hexagonal structures is either $\{0001\}\langle 11\bar{2}0\rangle$ or $\{10\bar{1}0\}\langle 11\bar{2}0\rangle$. In SiC, $\langle 11\bar{2}0\rangle$ is parallel to the closest packed row of atoms. The flow should take place along the $\langle 11\bar{2}0\rangle$ vector, because it describes the smallest displacement that each atom needs to undergo to restore the normal structure. (Fig. 6.2).

TABLE 6.2

Plane	Density (at / Å)		
		type I	type II
Basal (0001)	$\frac{2}{\sqrt{3}}\, a_o^{-2} =$	0.1217	0.1217
Prismatic $(10\bar{1}0)$	$\frac{1}{a_o c_o} =$	0.0086	0.0214
Prismatic $(11\bar{2}0)$	$\frac{2}{\sqrt{3}\, a_o c_o} =$	0.010	0.0248

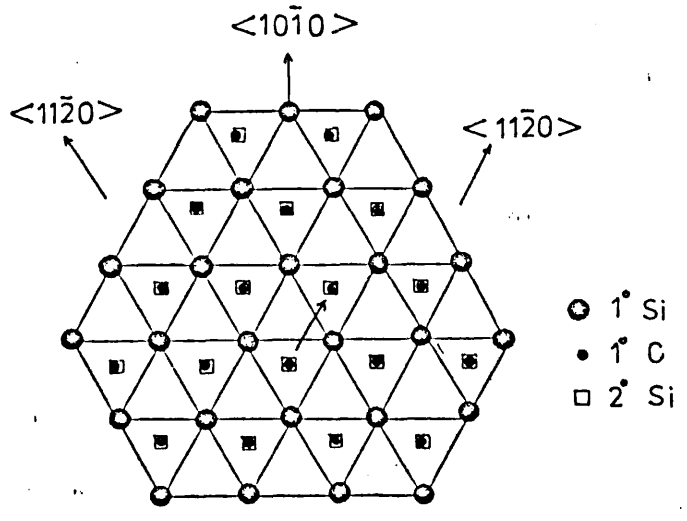

Fig. 6.2.

The hardness test indentations made at room temperaure, on the basal planes of silicon carbide type II crystals, do not contain the slip lines which one might expect due to the compact structure of the basal plane. These indentations, however, show traces of slip lines after the indented crystals have been annealed at very high temperatures. From their directions, i.e the $<11\bar{2}0>$ directions, it appears that the dislocations move on the $\{0001\}<11\bar{2}0>$ slip systems, at high temperatures.

Probable slip directions, on the prismatic planes, are $<0001>$ and $<11\bar{2}0>$. According to dislocation theory, the self-energy of a dislocation is proportional to the square of its Burgers vector, B. It means, that slip on a given plane should be in the direction of that dislocation which has the shortest possible Burgers vector. Since, the Burgers vector of total dislocations, on the $(10\bar{1}0)$ planes, are both vectors $c_o = 15.117$ Å and $a_o = 3.08$ Å, for $<0001>$ and $<11\bar{2}0>$ slip directions, respectively, then on the basis of the B^2-criterion for self-energy, slip along $<11\bar{2}0>$ should be favoured by a factor of 24 over the one for flow along $<0001>$. Thus, it is possible to anticipate a slip system $\{10\bar{1}0\}<11\bar{2}0>$ in silicon carbide type II crystals.

Silicon carbide type I crystals showed signs of slipping upon annealing the indented crystals. Slip lines on the $\{10\bar{1}1\}$ planes, around the diamond ball indentations with 500 g load, were found to be along the $[0\bar{1}14]$ directions, by the stereographic projection analysis. It is, again, a matter of speculation, if the dislocations moved as a result of the plastic deformation due to indentation or due to the release of the fracture energy after the indentation. As a conjecture, we are able to say that the slip system which

operates in the rare structure of SiC type I, at very high temperatures, is $\{10\bar{1}1\}\ <10\bar{1}4>$. Dislocations on the pyramid planes $\{10\bar{1}1\}$, with Burgers vector parallel to $<10\bar{1}1>$ have been observed in α-Al_2O_3 by Hockey[66], in a transmission electron microscope.

6.6 Fracture due to indentation

The manner in which an indentation induced crack travels downward from the surface of the crystal appears to be similar to that in highly brittle solids in general. The graph of 'crack extension force' vs 'crack length', in silicon carbide, shows the same four stages, viz., c_0, c_1, c_2 and c_3 in the crack propagation as found in amorphous silicates.

In Section 4.3, we have seen how a Hertzian crack propagates as the load on the indenter increases. We also noted that at loads less than the critical load P_o, a shallow ring crack of depth c_1 is formed. If applied load exceeds the minimum necessary to make a cone crack, a secondary ring crack is created outside the primary crack. This secondary crack does not give rise to an additional cone crack but it may join the primary and eject some material around the neck of the cone.

With the help of Equation 4.21, i.e.,

$$G = \frac{4(1-\nu^2)}{\pi E}\,(c/a)\left[\int_0^{c/a} \frac{\sigma_{\theta\theta}\,dz}{(c/a - z)^{\frac{1}{2}}}\right]^2$$ and Eq. 6.1, below,

one can predict the depth of fracture damage in the scale of the circle of contact if the applied load is known. It also provides a means of estimating the fracture surface energy. It is shown that the driving force for the crack, under equilibrium conditions, is just balanced by the resisting force; that is

$$G = 2 \cdot \Gamma \qquad \ldots \qquad \ldots \qquad (6.1)$$

where Γ is the fracture surface energy. Such information is of great

importance in the evaluation of surface fragmentation microfractures in silicon carbide cutting wheels.

The information provided by the fracture mechanics analysis, in Section 4.3.2, relates only to the median cracks and not the vents formed during unloading; to understand their mechanics one would need to know the residual stress field exerted by the relaxing deformation zone on unloading. This would, in turn, require a comprehensive description of the mechanics of deformation zone. This aspect of the indentation problem is still unanswered and needs a great deal of research. Our studies on the lateral vents bear on the degree of the cracking only. The lateral vent patterns around hardness impressions using different indenters all show similar geometrical features. Crystallographic trends were noted in the lateral vents. These trends are believed to be due to the effect that cleavage tendencies would have on the indentation induced crack geometry. The present results also show the tendency of basal cleavage and surface chipping due to the lateral vents. The practical significance of the manifestation of a certain crystallographic preference found in these features, is that the micro-fracture pattern in silicon carbide, and hence in other brittle materials, can be controlled. For example, the chipping process which occurs in the abrasion (which may be regarded as point indentation) of diamond can be controlled by changing the abrasion direction.

CONCLUSIONS

&

SUGGESTIONS FOR FUTURE WORK

6.7 Microhardness anisotropy

It has been established that anisotropy in hardness of silicon carbide crystals can be explained in terms of dislocation motion on slip sytems by considering the distribution of effective resolved shear stresses.

6.7.1 'Wet' and 'Dry' hardness

Our studies have shown that the microhardness of a material is affected by the surface conditions. Some specific points are made.

1. Microhardness of silicon carbide crystals is found to be significantly lowered by water absorbed from the air.

2. Upon heating the crystals, in the high temperature range 1500-2000^{o}C for few minutes, the crystals can be dry-desorbed. The hardness number determined after dry-desorbing is the correct one and reproducible. If hardness is to be used as an identification criterion for minerals, it is necessary to obtain the hardness number in the anhydrous condition.

6.7.2 Annealing

Decrease in hardness on annealing silicon carbide crystals (type II) at high temperatures is in agreement with the annealing results of Vahldiek[203] et al. and Williams[209] et al. on Mo_2C and TiC, respectively. A fall in hardness of these materials was noted after a heat treatment.

Silicon carbide crystals containing dislocations, in the range 10^3 - 10^4 cm^{-2}, are sensitive to heat treatment as far as their hardness is concerned. Crystals containing dislocation less than 100 cm^{-2} are not affected by the heat treatment.

6.7.2 Microplasticity of silicon carbide

Silicon carbide is brittle at room temperature. Evidence is produced in favour of its localised deformation are summed up here.

(i) The very fact that a diamond hardness impression can be made on silicon carbide crystals is indicative of its plastic deformation.

(ii) Prominent slip lines are seen inside many indentations, without cracking.

(iii) The Knoop hardness anisotropy of crystals can be related to the operative slip systems by the analysis of Daniels and Dunn. On the prismatic planes $\{10\bar{1}0\}$, maximum hardness was noted along $<11\bar{2}0>$ and a minimum effective resolved shear stress along this direction. It is concluded that the primary slip system is $(10\bar{1}0)<11\bar{2}0>$.

(iv) Another evidence of plastic deformation is provided by the stress birefringence around the indentations. On removing the hardness impressions by repeated etching of the crystal and on changing the geometry of the test sample, for example, thinning it by the ion-bombardment apparatus, the birefringence did not disappear. This is a case of plastic strain.

The small amount of microplasticity inside contact areas of the indenter on the crystal suggests a very high Peierls stress. As regards the observed plasticity around some indentations, it is believed that it might be due to dislocation motion following fracture. At room temperature a very high stress is required to produce an appreciable velocity. Before the applied stress even gets high enough to move the dislocations, the competing process of fracture comes into force. The large energy release at the tips of the fracture then brings about further plastic deformation.

6.7.3 Fracture

(i) Surface cracking which accompanys the diamond indentation is near-polygonal surface trace. The crack strarts at a point near the circle of contact and runs around to complete itself on the opposite side. If the load on the indenter is further increased, the crack starts propagating downward.

The crack formation may be treated as a combination of two stages. The surface crack is formed due to shallow stress domain near the surface where the tensile stresses are maximum. The surface crack is thus related to the tensile stresses σ_{rr}. The downward propagation of the crack is related to the second stress domain beyond the shallow surface region where the crack follows the σ_{zz} stress trajectories.

(ii) Previous calculations of Frank and Lawn[189] relating to stable crack dimensions in glass afford a means of computing these lengths in silicon carbide. The equlibrium crack length, from the $\psi(c/a)$ curves, is approximately equal to 0.05 which is nearly half of that in glass as estimated by Lawn.

(iii) The vent-crack systems in silicon carbide crystals are similar to those observed in glass. Median cracks are formed during loading and the lateral vents during unloading. They are visible around a hardness impression after their breakthrough to the surface.

6.8 Suggestions for future work

The role that friction plays in the hardness test needs to be studied. By making indentations on heated samples, possibility of new slip systems operating at high temperatures could be investigated.

Dislocation motion, dissociation, twinning, cross slip and work hardening can affect the magnitude of hardness anisotropy. The quantitative effects of these need study to obtain a complete understanding of the anisotropy. It may be worthwhile to see if there is any relationship between the critical resolved shear stress and the hardness anisotropy in very hard hexagonal crystals which have the same slip systems, i.e. the prismatic slip systems $\{10\bar{1}0\}<11\bar{2}0>$, as silicon carbide, e.g. TiB_2 (hardness 3400 kg.mm^{-2}) and Mo_2C (hardness 1800 kg.mm^{-2}). If such a relationship could be established, it might be possible to modify the Daniels and Dunn model to get a more correct hardness number.

For a complete description of the cone crack formation by the ball indentation of silicon carbide, further experimental studies of the crack extension force 'G' and function ψ (c/a) are required. The irreversible deformation zone within the test material, beneath the indenter, needs study. The process by which vent cracks are initiated is not yet known. The role of such variables as dislocation mobility, nature of environment, loading rate etc., in the crack nucleation, should be investigated. The process of healing of indentation induced cracks and the

environmental effects on healing need consideration.

A detailed investigation of the fracture interfaces, using transmission electron microscopy, would be useful for the study of strength degradation due to particle-surface contact.

APPENDICES

APPENDIX I.

Computer program STREFLD to solve the stress field components σ_{rr} (SI), σ_{zz} (XI), $\sigma_{\theta\theta}$ (YZB) and shear stress (SHST).

(Note. S11, ..., S44 denote the elastic compliances, and C11, ..., C44 the elastic constants of the indented material.)

```
      PROGRAM STREFLD (INPUT, OUTPUT, TAPE 5=INPUT, TAPE6=
     OUTPUT)
      COMPLEX T1, T2, T3, RØ1, RØ2, P1, P2, E1, E2, Q1, Q2, F1, F2,
     YU, YV
      DIMENSION DEL(50), R(50), Q(50)
      M=20
      READ (5, 10) (DEL(J), J=1, M)
   10 FORMAT (20F4.2)
      N=20
      READ (5, 1) (R(I), I=1, N)
    1 FORMAT (20F4.2)
      S11= 0.02077
      S12= -0.003965
      S13= -0.00167
      S33= 0.018
      S44= 0.0582
      SS = (S11+ S12)-2.*(S13**2)
      AA = S33/SS
      BB= 1./(S11-S12)
      C11=(AA+BB)/2.
      C12= (AA-BB)/2.
      C13= -S13/SS
      C44= 1./S44
      C33= (S11+S12)/SS
      FF= C11*C44
      GG= (C13*(2.*C44+C13)-C11*C33)
      HH= C33*C44
      V3 = 2.*C44/(C11-C12)
      CALL QUAD (FF, GG, HH, V1, V2)
      W1= SQRT(V1)
      W2= SQRT(V2)
      K1= ((C11*V1-C44)/(C13+C44))
      K2= ((C11*V2-C44)/(C13+C44))
C     MAX. INDENTATION PRESSURE 'P' ASSUMED UNITY
      P= 1.
C     THE RADIUS OF CONTACT CIRCLE 'A' ASSUMED UNITY
      A=1.
      DO 20 J = 1, M
      Z1= DEL(J)/W1
      Z2= DEL(J)/W2
      T1= CMPLX(Z1, A)
      T2= CMPLX(Z2, A)
```

```
      T3 = CMPLX(0., A )
      DO  2 I =1,N
      RØ 1 =  CSQRT(T1**2+R(I)**2)
      RØ2  =  CSQRT(T2**2+R(I)**2)
      P1   =  Z1*CLOG(T1+RØ1)-RØ1
      P2   =  Z2*CLOG(T2+RØ2)-RØ2
      E1   = AIMAG(P1)
      E2   = AIMAG(P2)
      Q1   =  CLOG(T1+RØ1)+0. 5*(2. *T1-3. *Z1)/(T1+RØ1)
      Q2   =  CLOG(T2+RØ2)+0. 5*(2. *T2- 3. *Z2)/(T2+RØ2)
      F1   = AIMAG(Q1)
      F2   = AIMAG(Q2)
      SI   = P*(W1*E1-W2*E2)/(W1-W2)
      U    = F1-F2
      XI   = 0. 5*P*R(I)*U/(W1-W2)
      YU   = AIMAG(((RØ1**2+RØ1*T1+T1**2)/(3. *(RØ1+T1)))-
     1((T3*A*T1)/(RØ1+T1))-(0. 5*Z1))
      YV   =  AIMAG(((RØ2**2+RØ2*T2+T2**2)/(3. *(RØ2+T2)))-
     1((T3*A*T2)/(RØ2+T2))-(0. 5*Z2))
      YW   =  W1*((1. /(V3*(1. +K1)))-1. /V1)
      YX   =  W2*((1. /(V3*(1. +K2)))-1. /V2)
      YY   .= W1/(1. +K1)
      YZ   =  W2/(1. +K2)
      YZA  =  ((YW*E1-YX*E2)+(((W1/(V3*(1. +K1)))*YU)-((W2
     1/(V3*(1. +K2)))*YV)))
      YZB  =  YZA/(W1-W2)
      SHST =  (YZB-SI)/2.
      WRITE (6, 13)  DEL(J), R(I), SI, XI, YZB, SHST
   13 FORMAT (5X, 6F12. 3)
    2 CONTINUE
   20 CONTINUE
      STOP
      END

      SUBROUTINE QUAD((CC, DD, EE, X1, X2)
      DISC = DD**2 - 4. *CC*EE
      IF (DISC) 200, 200, 202
  200 X1 = -DD/(2. *CC)
      X2 = X1
      RETURN
  202 ST = SQRT(DISC)
      X1  = (-DD+ST)/(2. *CC)
      X2  =(-DD-ST) /(2. *CC)
      RETURN
      END
```

APPENDIX II

Computer program ØRIØN to find the crack extension function $\psi(c/a)$ and the crack extension force.

```
1.        PROGRAM ØRIØN (INPUT, OUTPUT, TAPE 5=INPUT,
          TAPE 6=OUTPUT)
2.        DIMENSION AH(100), C(100), Z(100)
3.        MTOT= 37
4.        READ(5, 11)  (CC(M), AH(M), M=1, MTOT)
5.   11   FORMAT (2F20.9)
6.        WRITE (6, 3)
7.   3    FORMAT (5X, 'CRACK LENGTH= ', 5X, 'DEPTH = ', 8X,
         1'CRACK EXTEN. FUNC. = ')
8.        M=0
9.   2    M=M+1
10        DEL = -AH(M)
11.       N=0
12.  1    N=N+1
13.       DEL=DEL+AH(M)
14.       Y= 1./SQRT(C(M)**2-DEL**2)
15.       CALL ARA (DEL, 0., SS)
16.       Z(N) =ABS(Y*SS)
17.       IF (N.LT.101)  GO TO 1
18.       CALL SIMP (Z, 101, AH(M), D1)
19.       BB= D1**2
20.       B  = C(M)*BB
21.       WRITE (6, 23) C(M), DEL, B
22.  23   FORMAT(///, 5X, 2F15.5, F20.2)
23.       IF (M.LT.MTOT) GO TO 2
24.       STOP
25.       END
```

```
1.        SUBROUTINE ARA (QH, RH, SS)
2.        COMPLEX T1, T2, T3, RØ1, RØ2, P1, P2, E1, E2
3.        C11 = 50.4
4.        C12 = 9.8
5.        C13 = 5.6
6.        C33 = 56.6
7.        C44 = 17.0
8.   C    THE RADIUS OF CONTACT CIRCLE 'A' ASSUMED UNITY
9.        A = 1.
10.  C    THE MEAN INDENTATION PRESSURE 'P' ASSUMED UNITY
11.       P = 1.
12.       FF = C11*C44
13.       GG = (C13*(2.*C44+C13)-C11*C33)
```

```
      HH = C33*C44
      V3 = 2.*C44/(C11-C12)
      CALL QUAD (FF, GG, HH, V1, V2)
      W1 = SQRT(V1)
      W2 = SQRT(V2)
      Z1 = QH/W1
      Z2 = QH/W2
      T1 = CMPLX(Z1, A)
      T2 = CMPLX(Z2, A)
      T3 = CMPLX(0., A)
      RØ1 = CSQRT(T1**2+RH**2)
      RØ2 = CSQRT(T2**2+RH**2)
      K1  = ((C11*V1-C44)/(C13+C44))
      K2  = ((C11*V2-C44)/(C13+C44))
      P1  = Z1*CLOG(T1+RØ1)-RØ1
      P2  = Z2*CLOG(T2+RØ2)-RØ2
      E1  = AIMAG(P1)
      E2  = AIMAG(P2)
      YU  = AIMAG(((RØ1**2+RØ1*T1+T1**2)/(3.*(RØ1+T1)))-
     1((T3*A*T1)/(RØ1+T1))-(0.5*Z1))
      YV  = AIMAG(((RØ2**2+RØ2*T2+T2**2)/(3.*(RØ2+T2)))-
     1((T3*A*T2)/(RØ2+T2))-(0.5*Z1))
      YW  = W1*((1./(V3*(1.+K1)))-1./V1)
      YX  = W2*((1./(V3*(1.+K2)))-1./V2)
      YY  = W1/(1.+K1)
      YZ  = W2/(1.+K2)
      YZC = ((YW*E1-YX*E2)-(((W1/(V3*(1.+K1)))*YU)-((W2/(V3
     1*(1.+K2)))*YV)))
      SS  = YZC/(W1-W2)
      RETURN
      END

      SUBROUTINE SIMP(F, N, RH, RESULT)
      DIMENSION F(200)
      LAST = N-3
      S  = 0.
      DO 50 I=2, LAST, 2
   50 S=S+4.*F(I)+2.*F(I+1)
      RESULT = (S+F(I)+4.*F(N-1)+F(N))*RH/3.
      RETURN
      END

      SUBROUTINE QUAD(CC  DD, EE, X1, X2)
      DISC = DD**2-4.*CC*EE
      IF (DISC) 200, 200, 202
  200 X1 = -DD/(2.*CC)
      X2 = X1
```

```
6.        RETURN
7.  202   ST= SQRT(DISC)
8.        X1 = (-DD+ST)/(2.*CC)
9.        X2 = (-DD-ST)/(2.*CC)
10.       RETURN
11.       END
```

Note. The subroutine ARA finds the stress field component $\sigma_{\theta\theta}$, the subroutine SIMP solves the following integral, by Simpson's rule,

$$= \int_0^c \frac{dc}{[(c/a) - 1]^2}$$

and the subroutine QUAD determines the roots of a quadratic equation.

APPENDIX III

Calculation of the E.R.S.S. values

The E.R.S.S. values, for a given slip system, were determined by use of a stereographic projection following the method used by Daniels and Dunn[94]. The central plane of the projection is made to coincide with the plane of the specimen under the investigation. A Wulff net is used to locate the slip plane (SP) and the axis of rotation (AR). (See Fig. 1). The four corners of the indenter are plotted from the known angles, viz. $172^{\circ}30$ and $130^{\circ}\ 00'$. In Fig.1. , A, B, C and D represent the intersection lines of the indenter facets. The lines joining A and B, B and C etc. on great circles indicate the planes of the facets. Upon extending the lines AB etc. they intersect the primitive circle at points H, H' etc. These points denote the direction of a line parallel to the intersection of the facet with the specimen surface . The greatest slope of the facet happens to be midway between H and H' on the great circle which joins these points. The indenter is now rotated with respect to the test specimen , in increments of 10° , and the loci of slip plane (SP), slip direction (SD) and axis of rotation (AR) are plotted for each rotation and the corresponding angles ϕ , λ , ψ and γ are read by means of a Wulff net.

The E.R.S.S. values for all the four facets are calculated from the values of the one facet. It may be noted that because of a symmetry the results for facet AB and CD are

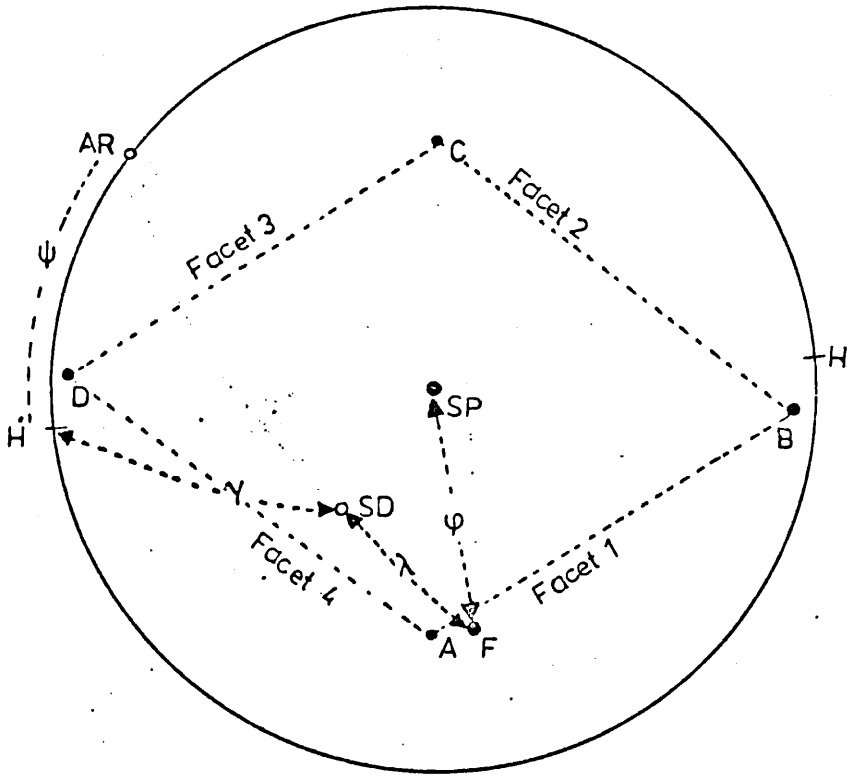

Fig. 1

identical but are out of phase by 180^{o}. Facet BC is out of phase from AB by 16^{o} due to the indenters facets being inclind to one another. It is assumed that slip occurs only on the slip system with the highest value of E. R. S. S. The maximum values for each facets are averaged to give a resultant E. R. S. S.

APPENDIX IV

X-ray and electron diffraction studies on some test specimens

The basal pinacoids of almost all the test specimens were well-formed and easily recognizable. Their orientation was often verified by obtaining electron diffraction patterns from ion-thinned sections. Fig. 2 shows an electron diffraction pattern from a silicon carbide crystal (type II). The electron beam, incident on the sample, was perpendicular to it. Table IV.1 gives the indices, the calculated interplanar spacings and the observed interplanar spacings, of some principal planes of silicon carbide crystals type II.

TABLE IV.1.

(h k l)	d-spacings (Å) observed	calculated
0 1 0	2.70	2.66
0 1 1	2.70	2.62
$\bar{1}$ 1 0	1.53	1.53

Combined use of x-ray diffraction and electron diffraction techniques enabled us to find out the nature of the intergrown structures, if they were present. Fig. 3 is a Laue transmission photograph from a silicon carbide crystal which appeared hexagonal in shape. A silicon carbide type II crystal gives a diffraction pattern with six-fold symmetry, as shown in Fig. 4, but the Laue transmission photograph shows only a three-fold symmetry. It, therefore, appears that this test specimen has a strong component of rhombohedral structure.

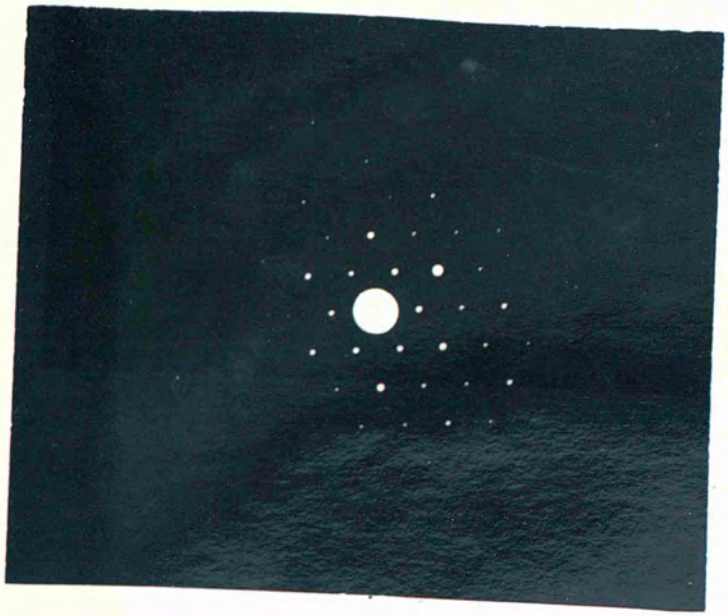

Fig. 2.

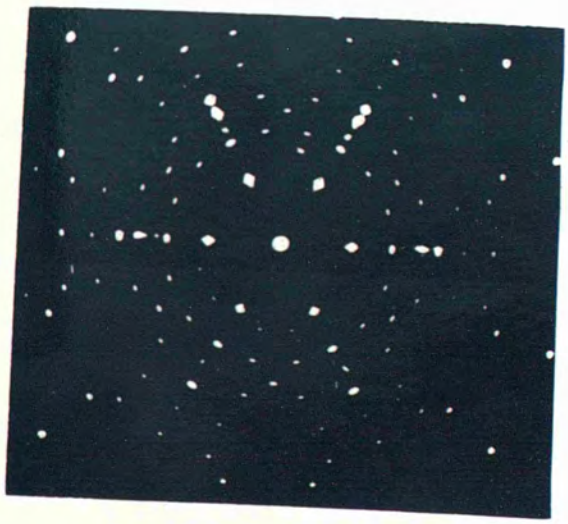

Fig. 3.

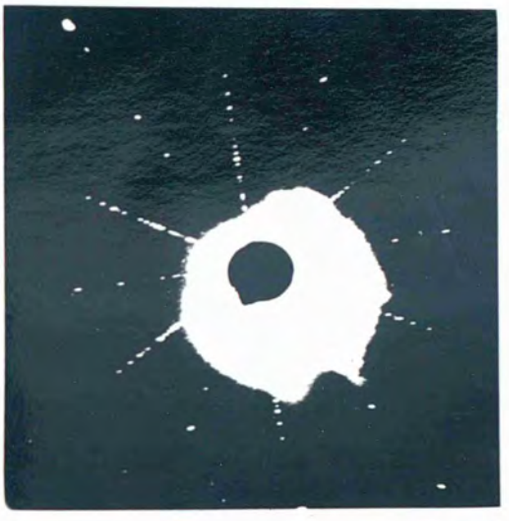

Fig. 4 . Laue back reflection photograph from SiC type II.

APPENDIX V

Illustrations of median and lateral vents formation

The median vent cracks are formed during indenter loading half-cycle. Figs. 5 a, c show the section view of the specimen being indented with a spherical indenter. The central deformation zone is shown by dark region. The crack tends to grow when the load on the indenter is increased, (Fig. 5 c). Fig. 6 shows *in situ* view of a Vickers indentation. The median crack is obscured by the central deformation zone.

The lateral vent cracks are formed during indenter unloading half-cycle. Figs. 5 b, d illustrate the section view for spherical indenter. The lateral vent cracks are indicated by heavy lines (light lines indicate the preceding median vent cracks). Figs. 5. e, f illustrate the plan view for Vickers and Knoop indenters. The lateral cracks appear like lobes between the median vent cracks. Fig. 5 b illustrates both the median and lateral cracks formed during unloading. Fig. 5. g shows an asymmetry in the lateral cracks formation. This is due to skew loading.

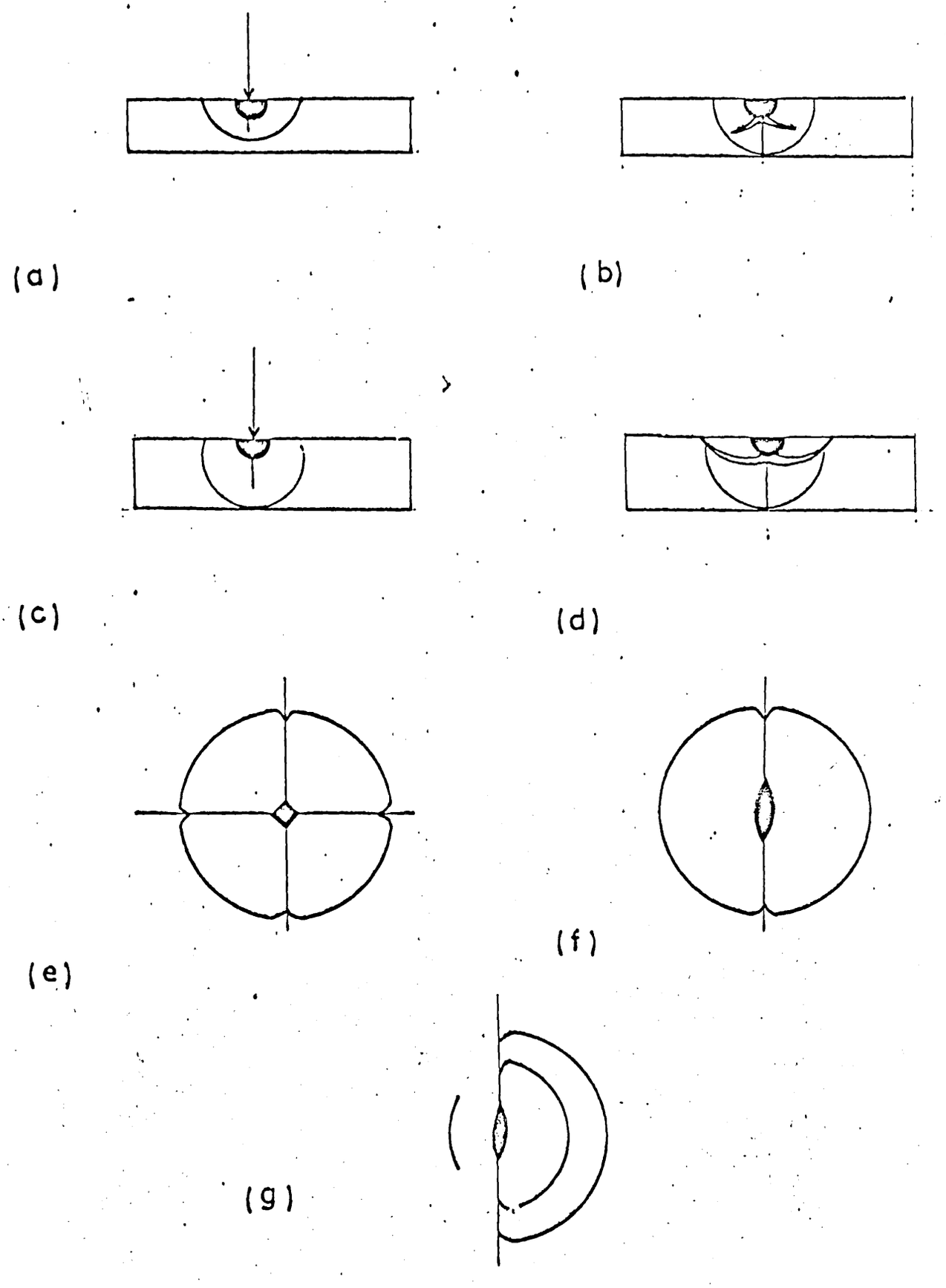

Fig. 5 . Schematic of vent crack formation.

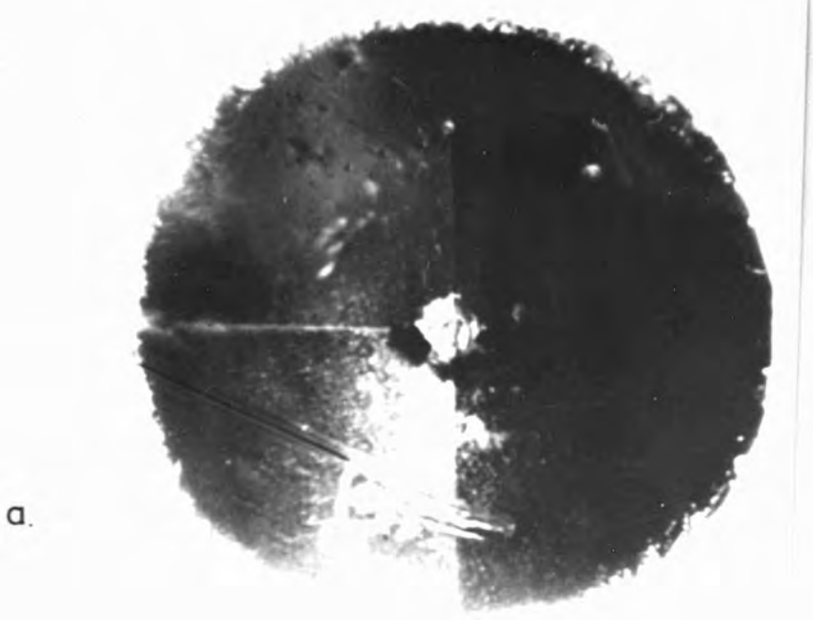

a.

X500

b.

X500

Fig. 6 . In situ photograph of Vickers indentation taken in transmitted light, specimen loaded to (a) 500 g; and unloaded to (b) zero.

REFERENCES

1. Hardness and Hardness Testing, (The Industrial Diamond Information Bureau, London), Bibliography No. 3, 1962.

2. Grodzinski, P., Metallurgica, 125, Sept., 1954.

3. Smith, R. and Sandland, G., J Iron St. Inst. 111, 285, 1925.

4. Knoop, F., Peters, C.G. and Emerson, W.B., J. Res. Nat. Bur. Stand. 23, 39-61, 1939.

5. Grodzinski, P., Ind. Diam. Rev. 12, 209, 235, 1952.

6. Richer, G.C., Metallurgica 31, 296, 1945.

7. Davidenkov, N.N., Metallurgica 37, 102, 1947.

8. Hill, R., Phil. Mag. 41, 745, 1950.

9. Tabor, D., J. Inst. Met. 79, 1-18, 1951.

10. Boeklen, R., Metall. 7, 436-441, 1953.

11. Braun, A., Schweiz Arch. Angew Wiss. 19, 67, 1953.
Cited in ref. No. 1 page 37.

12. Murphy, G., U.S.A.E.C. ISC-356, (Tech. Infor. Ser.) 1953.

13. Chuze, V.P. and Kontorova, T.A., Zhurn. Tekh. Fiz. 28, 1727, 1958.
Cited in ref. No. 1 page 70.

14. Bochvar, A.A. and Zhadaeva, O.S., Izvestia Akad. Nauk. SSSR 10, 1089, 1945.
Cited in ref. No. 1 page 10.

15. Saulnier, A., Rev. Alumin 29, 262, 1952.
Cited in ref. No. 1 page 34.

16. Drits, M.E. and Dokukina, N.V., in Microhardness of Metals and Semiconductors, (Consultant Bureau, New York), 194, 1971.

17. Friedkin, M.Ya., Za. Lab. 14, 1450, 1948.
Cited in ref. No. 1 page 17.

18. Brenner, P. and Kostron, H., Metallurgica 41, 209, 1950.

19. Bueckle, H., Z. Metallkde 43, 83, 1952.
Cited in ref. No. 1 page 31.

20. Gudstov, N.T. and Lozinskii, M.G., Zhurn. Tekh. Fiz. 22, 1249, 1952.
Cited in ref. No. 1 page 32.

21. Arkharov, V. I., Berenova, I. P. and Kozina, N. A., Doklady Akad. Nauk. SSSR 98, 207, 1954.
Cited in ref. No. 1 page 42.

22. Sammour, H. M., Metallurg. Ital. 13, 397, 1958.
Cited in ref. No. 1 page 70.

23. Glazov, V. M., Korol'kov, G.A. and Chistiakov, Y. D., Izvest. Akad. Nauk. SSSR OTN 12, 131, 1955.
Cited in ref. No. 1 page 51.

24. Glazov, V. M., Korol'kov, G. A. and Chistiakov, Y. D., Zhur. Fiz. Khim. 31, 1981, 1957.
Cited in ref. 1 page 66.

25. Glazov, V. M., Korol'kov, G. A. and Chistiakov, Y. D., Izvest. Akad. Nauk. SSSR OTN 10, 143, 1955.
English Abs. in Batelle Tech. Rev. Abstr. 5, 74, 1956.

26. Chernevaskaya, E. G., J. Technology UDC 548:539. 21, 3466, 1965.

27. Koval'skii, A. E., and Kanova, L. A., Za. Lab. 16, 225, 1950.

28. Povarennykh, A. S., Doklady Akad. Nauk. SSSR 112(6), 1098, 1957.

29. Howotny, H. and Vitovec, F., Pulvermetallurgee, I. Plansee Seminar: De Re Metallica Vienna, 1953.

30. Wolff, G. A., In:Semiconductors and Phosphors, New Jersey, 1958.

31. Petzold, A., Wihsmann, F. G. and Kamtz, H., Physics & Chem. Abst., pp 3, 1961.

32. Gol'dshmidt, V. M., Crystal Chemistry, Mocow-Leningrad, 1937.

33. Rebinder, P. A., Proc. 6th Physics Conf., Moscow, 1928.

34. Rebinder, P. A. and Likhtman, V., Proc. 2nd Int. Conf. Surface Activity, Academic Press, New York, pp 563, 1957.

35. Gendelev, S. Sh. and Scherbak, N. G., Soviet Physics – Crystallography 10(5), 592, 1966.

36. Goryunova, N. A. and Osmanov, E. S., Cited in: Microhardness of Metals and Semiconductors, (Consultant Bureau, New York-London), pp 203, 1971.

37. O'Neill, H. and Cuthbertson, J. W., J. Inst. Met. 46, 288, 1931.

38. Crow, T. B. and Hinsley, J. F., J. Inst. Met. 72, 461, 1946.

39. Lysaght, V. E., Mater. and Meth. 27, 84, 1948.

40. Thibault, N. W. and Nyquist, H. L., Trans. Amer. Soc. Metals 38, 271, 1947.

41. Yukutovich, M. V., Vandyshev, B. A. and Surikoya, E. E., Zavod Lab. 14, 338, 1948.

42. Tolansky, S. and Nickols, D. G., Nature 164, 103, 1949.

43. Tolansky, S. and Nickols, D. G., Nature 161, 840, 1949.

44. Tolansky, S. and Nickols, D. G., Phil. Mag. 43, 548, 1952.

45. Tolansky, S. and Williams, A. P., Proc. Phys. Soc. 68, 548, 1955.

46. Boyarskaya, Yu. S. and Val'kovskaya, M. I., Soviet Physics — Crystallography 7, 202, 1962.

47. Takeo, I., J. Amer. Ceram. Soc. 54, 24, 1971.

48. Smakula, A. and Klein, M. W., J. Opt. Soc. Amer. 39, 445, 1949.

49. Smakula, A. and Klein, M. W., Phy. Rev. 84, 1043, 1951.

50. Seitz, F., Phy. Rev. 79, 723, 1950.

51. Gilman, J. J. and Johnston, W. G., Dislocations and Mechanical Properties of Crystals, (John Wiley & Sons Inc., New York), 116-163, 1957.

52. Stokes, R. J., Johnston, T. L. and Li, O. H., Trans. AIME 215, 437, 1959.

53. Churchman, A. T., Geach, G. A. and Winton, J., Proc. Roy. Soc. (London) A238, 194, 1956.

54. Trefilov, V. I. and Mil'man, Yu. V., Soviet Physics Doklady 18, 1240, 1964.

55. Sumino, K. and Hasegawa, H., Trans. Japan Inst. Metals Supple. 9, 749, 1968.

56. Krylov, Y. A. and Iveronova, V. I., Kristallografiya 6, 784, 1961.

57. Pugh, E. N. and Samuel, L. E., Phil. Mag. 8, 301, 1963.

58. Johnson, O. W., J. Applied Phy. 37(7), 2521, 1966.

59. Rinder, W. and Tramposch, R. F., Applied Phy. Letters 3, 42, 1963.

60. Craig, J. V. and Pugh, E. N., J. Applied Phy. 35, 3417, 1964.

61. Ikeda, M., Japan J. Applied Phy. 7, 551, 1968.

62. Rinder, W. and Tramposch, R. F., J. Applied Phy. 36, 2079, 1965.

63. Carroll, K. G. and Tanaka, A., Trans. Met. Soc. of AIME 242, 338, 1948.

64. Nikitenko, V. I., Myshlyaev, M. M. and Eremenko, V. G., Soviet Physics Solid State 9, 2047, 1968.

65. Palmour III, H., Kriegel, W. W. and Duplessis, J. J., In: Mechanical Properties of Engg. Ceramics, 313-328, 1961.

66. Hockey, B. J., J. Amer. Ceram. Soc. 54(5), 223, 1971.

67. Rozhanskii, V. N., Nazarova, M. P., svetlov, I. L. and Kalashnikova, L. K., Phy. Stat. Solidi 41, 579, 1970.

68. Corteville, J. and Pons, L., Comp. Rend. Acad. Sci. 257, 1915, 1963.

69. French, D. N. and Thomas, D. A., Trans. AMIE 233, 950, 1965.

70. Takahashi, T. and Freise, E. J., Phil Mag. 12, 1, 1965.

71. Vahldiek, F. W., Mersol, S. A. and Lynch, C. T., Trans. AIME 236, 1490, 1966.

72. Rhodes, C. G., Trans. AIME 227, 286, 1963.

73. Hannink, R. H. J., Kohlstedt, D. L. and Murray, M. J., Phy. Stat. Solidi A6, K26, 1971.

74. Rowcliffe, D. J. and Warren, W. J., J. Mat. Sci. 5, 345, 1970.

75. Rowcliffe, D. J. and Hollox, G. E., J. Mat. Sci. 6, 1261, 1971.

76. Morgan, G. and Lewis, M. H., J. Mat. Sci. 9, 349, 1974.

77. Hannink, R. H. J., Kohlstedt, D. L. and Murray, M. J., Proc. Roy. Soc. A326, 409, 1972.

78. Shaffer, P. T. B., J. Amer. Ceram. Soc., 47, 466, 1964.

79. Bernhardt, E. O., Z. Metallk. 33, 135, 1941.
Cited in ref. No. 1 page 5.

80. Mitsche, R. and Onitsch, E. M., Mikroskopie 3, 257, 1948.

81. Schulze, R., Feinw Tech. 55, 190, 1951.
Cited in: Micro-Indentation Hardness Testing by Mott, B. W., (Butterworths Scientific Publications), pp 264, 1956.

82. Samuels, L. E., J. Inst. Met. 77, 626, 1950.

83. Mott, B. W., Ford, S. D. and Jones, E. R. W., A. E. R. E. Harwell Report M/R 1017, 1952.

84. Campbell, R. F., Henderson, O. and Donleavy, M. R., Trans. Amer. Soc. Metals 40, 954, 1948.

85. Rostoker, W., J. Inst. Met. 77, 175, 1950.

86. Meincke, H., Metallk. 34, 403, 1942.

87. Onitsch, E. M., Mikroskopie 2, 131, 1947.

88. Walker, W. W. and Demer, L. J., Trans. AIME 230, 613, 1964.

89. Jorgensen, P. J. and Westbrook, J. H., J. Amer. Ceram. Soc. 47, 332, 1964.

90. Westbrook, J. H. and Jorgensen, P. J., Trans. AIME 233, 425, 1965.

91. O'Neill, H., J. Inst. Met. 30, 299, 1923.

92. Schulz, F. and Hanemann, H., Z. Metallkunde 34, 124, 1941.

93. Winchell, H., Am. Mineral. 30, 583, 1945.

94. Daniels, F. W. and Dunn, C. G., Trans. ASM 41, 419, 1949.

95. Sandulova, A. V. and Rybak, V. M., In: Microhardness of Metals and Semiconductors, (Consultant Bureau, New York-London) pp 52, 1971.

96. Ablova, M. S. and Feoktstova, N. N., ibid.

97. Attinger, C., Ind. Dia. Rev. 12, 136, 1952.

98. Garfinkle, M. and Garlick, R. G., Trans. AIME 242, 809, 1968.

99. Meincke, H., Ind. Dia. Rev. 11, 37, 1951.

100. Peter, C. G. and Knoop, F., Metals and Alloys, 12, 292, 1940.

101. Shriramurty, T., Ph. D Dissertation, University of London, 1962.

102. Verma, A. R., Electrochem. 56, 268, 1952.

103. Verma, A. R., Phil. Mag. 43, 441, 1952.

104. Verma, A. R., Phil. Mag. 42, 1005, 1951.

105. Verma, A. R., Nature 168, 430, 1951.

106. Amelinckx, S., J. Chim. Phys. 50, 45, 1953.

107. Amelinckx, S., Naturwissenschaten 39, 425, 1952.

108. Amelinckx, S., J. Chim. Phys. 49, 411, 1952.

109. Amelinckx, S., J. Chim. Phys. 48, 475, 1951.

110. Burton, W. K., Cabrera, N. and Frank, F. C., Nature 163, 398, 1949.

111. Mitchell, R., Zeitschrift fur Kristallographie 109, 1, 1957.

112. Bhide, V. G. and Verma, A. R., Z. fur Krist. 111, 142, 1959.

113. Horn, F. H., Phil. Mag. 43, 1210, 1952.

114. Amelinckx, S. and Gevers, R., J. Chim. Phys. 50, 321, 1953.

115. Amelinckx, S. and Strumane, G., J. Appl. Phys. 31(8), 1359, 1960.

116. Hamilton, D. R., J. Appl. Phys. 31, 112, 1960.

117. Hockey, B. J., J. Mat. Sci. 10, 1351, 1975.

118. Dash, W. C., Am. Phys. Soc. Meeting, Baltimore, Maryland, March 17, 1953.

119. Lang, A. R., Nature , pp 248, Jan. 1967.

120. Bond, W. L. and Andrus, J., Phys. Rev. 106, 1211, 1956.

121. Nye, J. F., Spencer, R. D. and Spracking, M. T., Proc. Roy. Soc., 773, 1957.

122. Bullough, R., Phy. Rev. 10, 620, 1958.

123. Lederhandler, S. R., J. Appl. Phys. 30, 1631, 1959.

124. Urusovskaya, A. A., Tyaagaradzhan, R. and Kostin, N., Soviet Physics — Crystallography 11, 245, Sept. 1966.

125. Okudu, S. et al., Japan J. Appl. Phys. 7, 1422, 1968.

126. Wiedehorn, S. M., Hockey, B. J. and Roberts, D. E., Phil. Mag. 28, 783, 1973.

127. Howes, V. R. and Tolansky, S., Proc. Roy. Soc. A230, 287, 1955.

128. Tolansky, S. and Howes, V. R., Proc. Roy. Soc. b70, 521, 1957.

129. Eremenko, V. G. and Nikitenko, V. I., Phy. Stat. Solidi (a) 14, 317, 1972.

130. Hill, M. J. and Rowcliffe, D. J., J. Mat. Sci. 9, 1569, 1974.

131. Eagle, G. B. and Liggett, L. M., Mat. in Des. Engg. 49, 88, 1959.

132. Taylor, K. M., Materials & Methods 44, 92, 1956.

133. Sevin, R., J. Four. Elect. 64, 55, 1955.

134. Knippenberg, W. F., Growth Phenomenon in Silicon Carbide (Philips Technical Report), Drrukkerij J. Valkenburg, Echt, 1963.

135. Drowart, J., Maria G. and Inghram, M. G., J. Chim. Phys. 29, 1015, 1958.

136. Kendall, J. T., J. Chem. Phy. 21, 821, 1953.

137. Lely, J. A. and Kroger, F. A., Proc. Int. Con. Semiconductors, Phosphors, Vieweg Braun Schweig, 1958.

138. Van Daal, H. J., Knippenberg, W. F. and Wasscher, J. D., J. Chem. Solids 24, 109, 1963.

139. Smith, R. A., In: Semiconductors, C. U. P., 1959.

140. Busch, G., Labhart, H., Helv. Phy. AcT. 19, 463, 1946.

141. Racette, J. R., Phys. Rev. 107, 1542, 1957.

142. Choyke, W. J. and Patrick, L., Phys. Rev. 105, 1721, 1957.

143. Lea, A. C., J. Soc. Tech. 33, 27, 1949.

144. Nakatogawa, T., J. Chem. Soc. Japan (Ind. Chem. Sect.) 57, 348, 1954.

145. Lambertson, W. A., U. S. A. E. C., TID 7530 I, 1957.

146. Adamsky, R. F., J. Phy. Chem. 63, 305, 1959.

147. Baumhauer, H., Z. Krist. 50, 249, 1915.

148. Ott, H., Z. Krist. 62, 201, 1925.

149. Thibault, N. W., Am. Miner. 29, 249, 327, 1944.

150. Verma, A. R., Krishna, P., Polymorphism and Polytypism in Crystals (John Wiley & Sons, Inc. New York. London. Sydney), pp 106, 1966.

151. Wyckoff, R. W. G., In: Crystal Structure Vol. I (Interscience Pub. N. Y.), 1948.

152. Pauling, L., In: Nature of Chemical Bond (Cornell University Press, Ithaca), 1945.

153. Faessler, A., In: Proc. Int. Conf. Semiconductors Phys., Prague, 914, 1960.

154. Hooge, F. W., Z. Physik Chem. (Frankfurt) 21, 288, 1959. Cited in reference No. 150.

155. Tolansky, S., Multiple-beam Interferometry of Surfaces and Films (Oxford), 1948.

156. Thomas, G., In: Electron Microscopy and Strength of Crystals (Wiley, N. Y), 1963.

157. Heidenreich, R. D., J. Applied Phys. 20, 993, 1949.

158. Hietel, B. & Meyerhoff, K., Z. Physik 165, 52, 1961.

159. Shimomura, Y., Minagawa, S. and Saito, S., Bull. Univ. Osaka Prefect. Ser. A:12, 139, 1964. Cited in Rev. Sci. Inst. 38, 223, 1967.

160. Drum, C. M., Third European Reg. Conf. on Electron Microscopy, held in Prague 64A, 329, 1964.

161. Cabrera, N., Bull. Am. Phy. Soc. 1, 3, 140, 1956.

162. Cabrera, N. and Levin, M. M., Phil. Mag. 1, 450, 1956.

163. Wyon, G. and Lacombe, P., Report on Conf. on Defects in Crystalline Solids, Phy. Soc. London, pp. 187-202, 1955.

164. Tyapunina, N. A., Predvoditelev Nauch. dokl. vyssh. Shkoly 2, 184, 1958.

165. Frank, F. C., Phil. Mag. 42, 151, 1950.

166. Forty, A. J., Phil. Mag. 43, 72, 1952.

167. Vogel, E. L. and Lovell, L. C., J. Appl. Phys. 27, 1413, 1956.

168. Pfan, W. G. and Lovell, L. C., Acta Met. 3, 512, 1955.

169. Gilman, J. J. and Johnston, W., J. Appl. Phys. 27, 1018, 1956.

170. Griffin, L. J., Phil. Mag. 42, 775, 1951.

171. Patel, A. R. and Mathai, K. J., Ind. J. Pure Appl. Phy. 7, 486, 1969.

172. Horn, H., Phil. Mag. 43, 1210, 1950.

173. Hirth, J. P. and Vassamilet, L., J. Appl. Phys. 29, 595, 1958.

174. Faust (Jr.), J. W., In: Silicon Carbide (Pergamon Press, London), 403, 1960.

175. Hertz, H., Hertz's Misc. Papers (Macmillan, London), 1896.

176. Willis, J. R., J. Mech. Phys. Solids 14, 163, 1966.

177. Elliot, H. A., Proc. Camb. Phil. Soc. 45, 621, 1949.

178. Westergaard, In: Contributions to the Mechanics of Solids, 1938.

179. Sen, B., Phil. Mag. 27, 596, 1939.

180. Green, A. E. and Zerna, W., Theoretical Elasticity (Clarendon Press), 1954.

181. Galin, L. A., Contact Problems in Theory of Elasticity, Trans. North Carolina State College, 1961.

182. Chen, W. T., Int. J. Solid Struc. 5, 191, 1969.

183. Conway, H. D. and Farnham, K. A., J. Appl. Mech. 34, 756, 1967.

184. Hamilton, G. M. and Goodman, L. E., J. Appl. Mech. 33, 371, 1966.

185. Griffith, A. A., Phil. Trans. A 221, 163, 1920.

186. Griffith, A. A., First Int. Cong. Appl. Mech. (Delft), 55, 1924.

187. Irwin, G. R., Handbuch der Physik 6, 551, 1958.

188. Kelly, A., Strong Solids (Clarendon Press), London, Chap. 1, 1966.

189. Frank, F. C. and Lawn, B. R., Proc. Roy. Soc. A299, 291, 1967.

190. Lawn, B. R., J. Appl. Phy. 39, 4828, 1968.

191. Frocht, M. M., In: Photoelasticity (John Wiley & Sons, Inc., London) pp. 194, 1949.

192. Chung, D. H. and Buessem, W. R., In: Anisotropy in Single-Crystal Refractory Compounds, Ed. Vahldiek, F. W and Mersal, S. A. (Plenum Press, N. Y.) Vol. II, 218, 1968.

193. Lawn, B. R., In: The Science of Hardness Testing and its Research Applications. Symposium Proc., Ed. Westbrook and Conrad (ASM), pp. 421, 1973.

194. Brodie, C. B. and Smoluchowski, R., Trans. Am. Soc. Metals-Discussion 35, 374, 1945.

195. Bergsman, E. B., Am. Soc. Met. Bull. 37, 176, 1951.

196. Espig, H., Cited in Am. Miner. 29, 249, 327, 1944.

197. Allen, J. W., Phil. Mag. 4, 1046, 1959.

198. Kohn, J. A., Ind. Dia. Rev. 11, 211, 1951.

199. Stern, W., Ind. Dia. Rev. 11, 237, 255, 1951.

200. Keyes, R. W., In: Silicon Carbide (Pergamon Press, N. Y.), pp. 521, 1960.

201. Feng, C. and Elbaum, C., Tran. AIME 212, 47, 1958.

202. Partridge, P. G. and Roberts, E., J. Inst. Met. 92, 50, 1963.

203. Vahldiek, F. W., Mersol, S. A. and Lynch, C. T., Trans. AIME 236, 1490, 1966.

204. Gilman, J. J., Trans. AIME 212, 783, 1958.

205. Dale, J. R. and Price, J. C., Solid State Electronics 3, 105, 1961.

206. Mil'vidskii, M. G. and Lainer, L. V., Metallurgizdat 6, 149, 1962.

207. Friedel, J., In: Dislocations (Pergamon Press) pp. 277, 1964.

208. Hasselman, D. P. H. and Batha, H. D., Appl. Phy. Letters 2(6), 111, 1963.

209. Williams, W. S. and Lye, R. G., U. S. A. Report ML-TDR-64-25 PartII, April, 1965.

210. Bowden, F. P. and Tabor, D., In: Friction and Lubrication of Solids Vol. I (Oxford University Press, London), 1950.

211. Brookes, C. A., O'Neill, J. B., and Redfern, A. W., Proc. Roy. Soc. (London), 322A, 73, 1971.

PUBLICATIONS

JOURNAL OF MATERIALS SCIENCE 10 (1975) 1375–1380

Creep of hot-pressed silicon nitride

SALAH UD DIN, PATRICK S. NICHOLSON
Department of Metallurgy and Materials Science, McMaster University, Hamilton, Ontario, Canada

Creep tests were undertaken on hot-pressed silicon nitride in the temperature range 1200 to 1400°C. The activation energy for creep was determined to be 140 kcal mol^{-1} and the stress exponent of creep rate was 1.7. The creep behaviour is ascribed to grain-boundary sliding accommodated by void deformation at triple points and by limited local plastic deformation. Electron microscopic evidence supporting this mechanism is presented.

1. Introduction

In recent years there has been considerable interest in hot-pressed silicon nitride because of its high strength. It has emerged as a prime candidate material for high efficiency gas turbines, and its creep behaviour is an essential design parameter.

Little or no creep data have been reported in the open literature on silicon nitride. In 1961 the creep characteristics of a low-strength material were studied by Glenny and Taylor [1], and Stokes *et al.* [2] made passing mention of the relative creep resistance of high- and low-strength silicon nitride materials in 1972. More recently, tensile and bend data generated by Westinghouse [3] have become available.

Creep of materials at high temperatures and low stresses can generally be divided into three creep-rate regimes. The initial deformation is rapid (stage I), and the creep rate subsequently decreases until the second stage (II) is reached, wherein the creep rate remains constant. Finally, in stage III, the creep rate increases again, producing cracks followed by failure. Most ceramics show the first two stages. This work was undertaken to investigate stage II or "steady state" creep of hot-pressed* silicon nitride and the microstructural changes associated therewith.

2. Experimental

2.1. Material characterization

The Si_3N_4 material was characterized by spectrographic analysis, bulk density measurements, grain size determinations and X-ray analysis. Samples for spectrographic analysis were ground in a silicon carbide mortar and pestle and dissolved in HF.

Spectrographic analysis revealed that the material was 97% silicon nitride. The major impurities were Ca (0.04 wt %), Mg (0.7 wt %), Fe (0.4 wt %), and Al (0.4 wt %). The density was found to be 98% of the theoretical value. Sections for grain size determination were mounted in plastic and rough polished with 400 grit diamond. Final polishing was undertaken on 0.25 μm diamond. After polishing, the samples were removed from the mount and etched in a mixture of HF, HNO_3, and H_2O_2 (1:1:3) at 80°C for 15 min. Shadowed replicas of the etched surface, made by the two-stage carbon replica technique, were examined in the electron microscope and grain sizes determined by the intercept method. About 85% of grains were equi-axed with diameter in the range 0.5 to 2 μm. The remainder were elongated with lengths in the range 1 to 5 μm large. X-ray diffraction showed that the β and α phases of silicon nitride were present. The energy-dispersive X-ray analysis technique was used to identify the intergranular glassy phase. It was found to be a compound of Mg, Ca, and Fe silicates.

2.2. Creep testing

All specimens were taken from a single hot-pressed billet to eliminate variables such as different chemical compositions and thermal history. The material was received in the form of $(1\frac{1}{4} \times \frac{1}{4} \times \frac{1}{4})$ in. bars.

Creep tests were conducted in four-point bending with silicon carbide knife edges and a

*Norton H.S. 130 Si_3N_4.

© *1975 Chapman and Hall Ltd.*

TABLE I

Specimen	Temperature	Stress (10^3 psi)	Strain after 80 h ϵ (%)	Steady state strain-rate $\dot{\epsilon}$ (h^{-1})
1	1260	8	0.16	3.8×10^{-6}
2	1260	10	0.20	0.6×10^{-5}
3	1260	15	0.41	1.25×10^{-5}
4	1260	20	0.63	2.00×10^{-5}
5	1300	10	0.86	1.6×10^{-5}
6	1300	15	1.02	2.8×10^{-5}
7	1300	20	1.24	4.5×10^{-5}
8	1350	10	1.18	6.5×10^{-5}
9	1350	15	1.47	1.5×10^{-4}
10	1350	20	1.80	2.5×10^{-4}
11	1400	10	1.55	2.1×10^{-4}
12	1400	15	1.82	4.5×10^{-4}
13	1400	20	2.1	5.8×10^{-4}

templet was used to centrally locate the samples. The desired load was applied by lowering appropriate slotted weights on to a load plate located on top of the sample loading column. Counter weights were used to balance the load-free column weight. A silicon carbide clamshell furnace was used to heat the sample to 1400 ± 5°C and a Pt/Pt–Rh thermocouple measured the specimen temperature. Samples were creep tested between 1200 and 1400°C at stresses between 8000 and 25 000 psi*. Maximum deformation was limited to about 3.0% and an LVDT utilized to monitor the creep deflection. The LVDT was mounted rigidly under the load plate.

A series of isothermal creep tests was undertaken for times up to 250 h (standard creep tests). In addition, individual specimens were creep tested by (a) stress cycling at constant temperature and (b) temperature cycling wherein the stress was held constant and the temperature changed incrementally. The former was used to evaluate the stress exponent of the creep rate and the latter to determine the activation energy for the creep process.

2.3. Electron microscopy

Samples for the electron microscopic analysis were taken from the tension edge of crept specimens. The first step involved the production of a geological thin section by grinding to 20 μm on a diamond wheel. The material was then ion-thinned until a small perforation was observed in the centre of the foil. A graphite film was evaporated onto the specimen before introduction into the transmission electron microscope.

3. Results

Creep data for the specimens tested are summarized in Table I. Typical standard creep curves at 1260 and 1300°C at a stress of 10 000 psi are shown in Fig. 1. The regimes of creep are readily distinguishable. The transients in all the creep tests were quite long (40 to 50 h) and, therefore, long-time tests (up to 250 h) were conducted.

The outer fibre stress and strain in bending specimens were calculated using the Timoshenko [4] elastic equations. The use of elastic equations for the evaluation of the plastic strain is questionable but it has been shown in a previous study [5] that for low plastic strains up to 3%, the elastic equations are valid.

Fig. 2 shows the log-log plot of steady state creep rate versus stress. The relationship between the two is given by the empirical law:

$$\dot{\epsilon} = A e^{-E/RT} \sigma^n \qquad (1)$$

where E is the activation energy.

From the slope of these plots, the stress exponent (n) of the creep rate was determined and is given in Table II. The exponent was also found by changing the stress level during a test and using Equation 1. The result of a stress change experiment is illustrated in Fig. 3.

The activation energy for the creep process was also determined in two ways, i.e. constant stress,

*10^3 psi ≡ 6.89 N mm^{-2}

TABLE II

Activation energy (kcal mol^{-1})			Stress exponent	
Temperature change (°C)	Temperature cycling experiment	Arrhenius plot	Stress change experiment	Arrhenius plot
1300–1350	140 ± 2	135 ± 2	1.70 ± 0.05	1.75 ± 0.02
1350–1400	144 ± 2	138 ± 2		

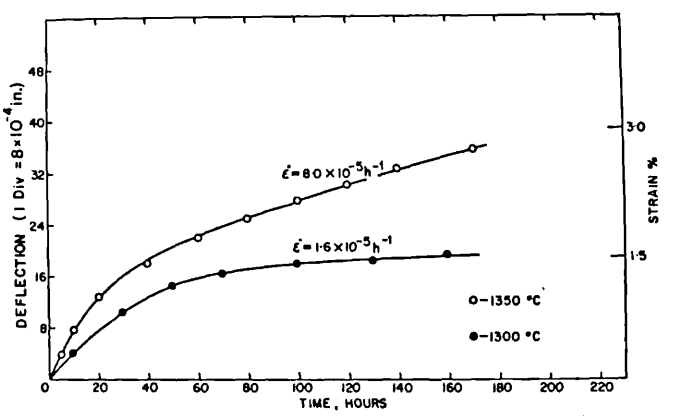

Figure 1 Strain-time curves.

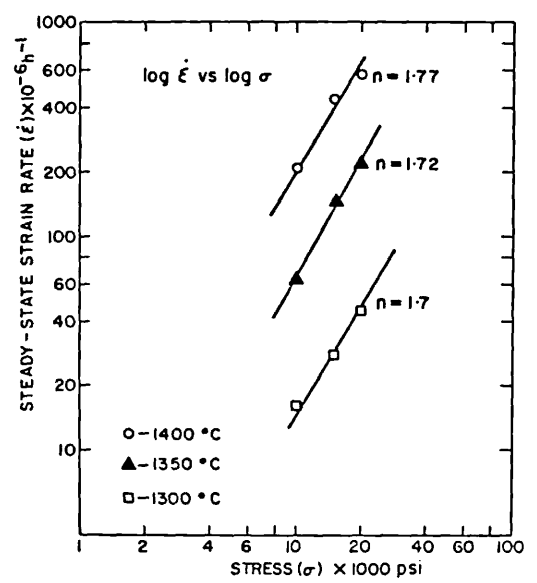

Figure 2 Steady state strain-rate as a function of stress.

temperature-change experiments, and Arrhenius plots derived from the individual creep experiments. The former technique again involves the application of Equation 1 (this time at constant stress) and the same restrictions concerning stage II creep apply. The curves of the temperature-change experiments are shown in Fig. 4 and the calculated activation energies listed in Table II. An Arrhenius plot (log $\dot{\epsilon}$ versus $1/T$) for the individual creep runs is shown in Fig. 5 and the activation result included in Table II. An average value of activation energy of 140 kcal mol^{-1} resulted from the temperature-change experiments and 135 kcal mol^{-1} from the Arrhenius plot.

Transmission electron microscopic images of the structures before and after the creep tests are shown in Figs. 6 and 7. Voids and grain-boundary separation can be seen in the crept specimens. Such features might result from the ion-thinning process but their absence in the uncrept specimens and the fact that the specimen areas examined were selected away from the perforated areas of the foil preclude this explanation. These features, therefore, develop during creep and can be explained by the classic triple-point void formation accompanying grain-boundary sliding (Fig. 8). Also evident in this figure is dislocation activity in a grain in the vicinity of the void. This suggests that some plastic accommodation has also occurred in this case.

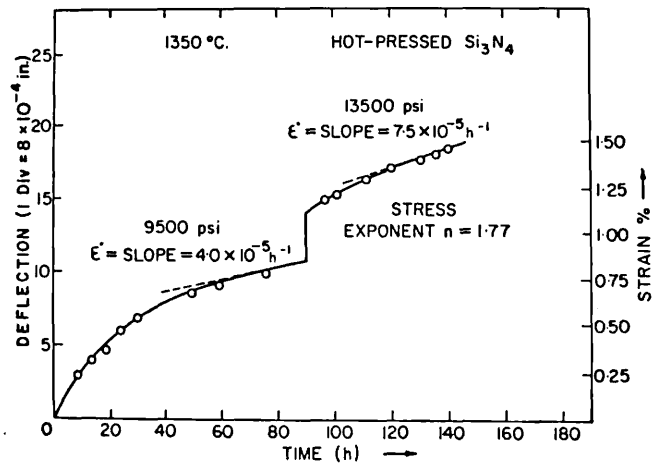

Figure 3 Stress-change data plot.

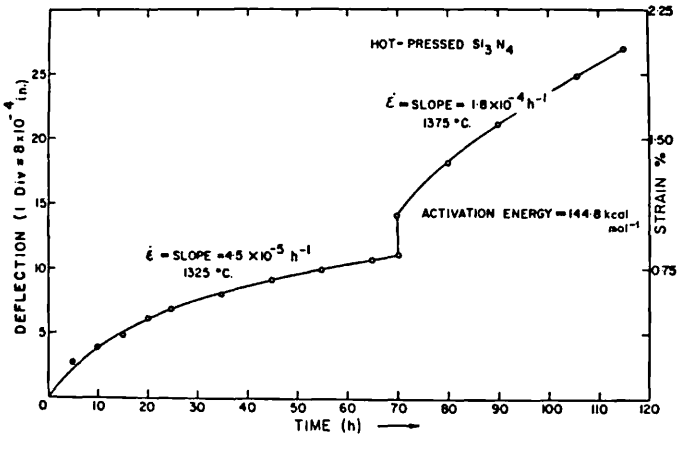

Figure 4 Temperature-change data plot.

4. Discussion

All the experimental creep curves exhibited the stage I transient and secondary stage II creep regimes. The third region, that of an accelerating creep rate, commonly observed in metals and some ceramic materials, was not attained within 250 h or a strain of $\sim$ 2.5%. To ensure the analysis of stage II creep, extended time tests were carried out.

The stress exponents ranged between 1.55 and 1.8. Purely viscous creep would give a stress exponent of 1. Hence, if grain-boundary sliding accommodated by a viscous mechanism were the rate-controlling mechanism, a value of n of 1 would be expected. A non-integral value of n has been obtained for other ceramic materials. Poteat and Yust [6] determined values of n between 1.04 and 1.59 for the creep of ThO_2; Passmore *et al.* [7] obtained n = 1.5 for the creep of ZrO_2 and Vasilos *et al.* [8] 1.60 for MgO. Gifkins [9] made a survey of the published creep data on a variety of materials and remarked that the non-integral value of n was due to the existence of "parallel-concurrent" mechanism of creep. Alden [10] and Heuer *et al.* [11] advanced the theory of non-Newtonian grain-boundary sliding involving climb-glide motion of dislocations near grain boundaries in fine-grain metallic systems and ceramic polycrystals. Fig. 1 indicates that there was no transition from one process to another over the range of stresses and temperatures employed. If it had taken place it would have been shown by two lines of different slopes instead of one continuous line. A non-Newtonian grain-boundary sliding model is the most likely explanation

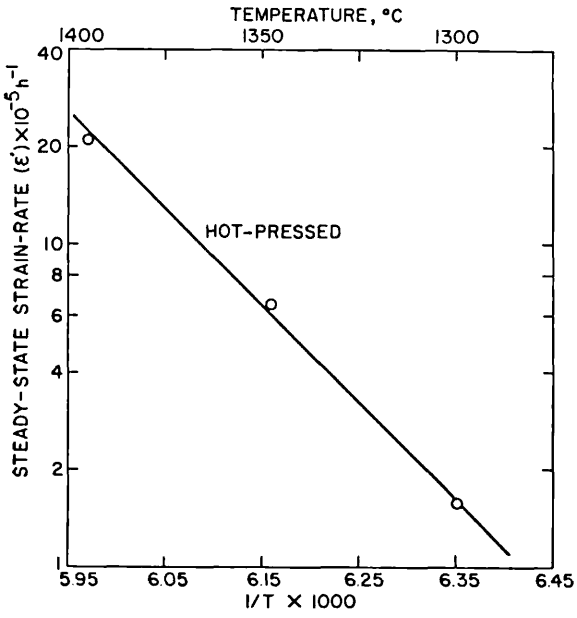

Figure 5 log $\dot{\epsilon}$ versus $1/T$ plot.

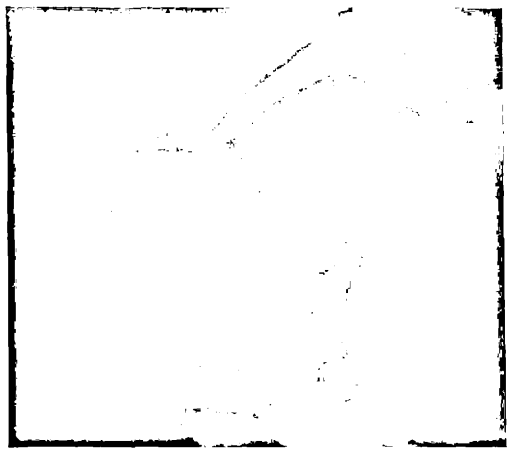

Figure 7 Grain-boundary separation after deformation.

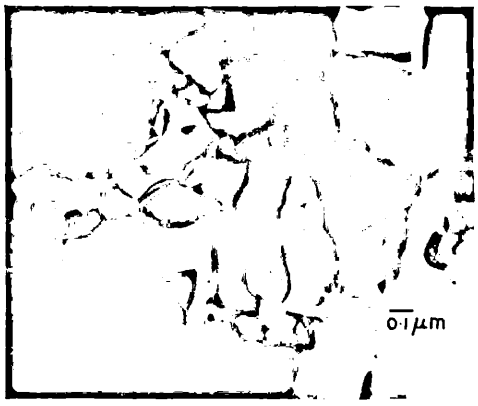

Figure 6 Microstructure of as-fabricated material.

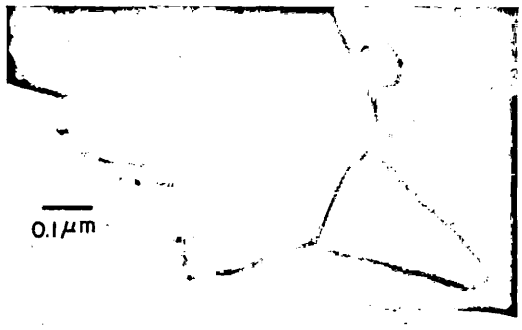

Figure 8 Void at triple point and grain-boundary dislocations.

of the creep results presently reported wherein creep occurs via the glassy grain-boundary phase (grain-boundary sliding) and accommodation mechanisms other than just void formation, such as localized plastic flow controlling the creep rate. The dislocation activity observed near some grain-boundary voids tends to support this explanation, and such "mixed" control could result in a non-integral stress exponent.

The activation energy in itself is not indicative of the creep mechanism but it is interesting to compare mechanisms suggested for some other ceramic materials having values of activation energies close to that determined in this work. Poteat and Yust [6] working on polycrystalline ThO_2 determined the activation energy for the creep process to be $\sim$ 120 kcal mol^{-1}. They observed voids and grain-boundary shearing following deformation. The activation energy for the creep of alumina was reported to be 126 $\pm$ 10 kcal mol^{-1} by Heuer *et al.* [11] and Sugita *et al.* [12] and in both cases, microstructural studies provided evidence of grain-boundary sliding accommodated by voids at triple points and associated grain-boundary dislocations. The activation energy for creep in the present work agrees with that reported by Kossowsky [13]. He observed triangular wedges to develop in

hot-pressed silicon nitride following creep and suggested grain-boundary sliding as the rate-controlling mechanism. However, the non-unity stress exponent value precludes grain-boundary sliding accommodated by viscous mechanism as exerting exclusive control of the creep rate, and a mixed control mechanism is suggested.

5. Conclusions

High temperature creep tests on hot-pressed silicon nitride showed that the creep rate was proportional to stress to $\sim$ 1.7 power. Based on this value and microstructural observations of triple-point voids, and in some cases adjacent dislocation activity, a creep mechanism of grain-boundary sliding with some accommodation by dislocation climb and/or glide is suggested.

The activation energy for creep was calculated as 140 kcal mol^{-1} and this value compares favourably with other values obtained in ceramic systems in which grain-boundary sliding during creep has been observed.

Acknowledgement

The research for this paper was supported, in part, by The Defence Research Board of Canada, Grant number 7565-09, and samples were supplied by Norton Co.

References

1. E. GLENNY and T. A. TAYLOR, *Powder Met.* **8** (1961) 164.
2. R. F. STOKES, R. J. LUMBY and R. F. COE, *Abstract Bull. Amer. Ceram. Soc.* **51** (1972) 428.
3. WESTINGHOUSE RESEARCH LABORATORY, *Pittsburgh*, U.S.A., private communication.
4. S. TIMOSHENKO, "Strength of Materials, Part I, Elementary Theory and Problems" (Van Nostrand, New York, 1930) p. 359.
5. G. R. TERWILLIGER, Ph.D. Thesis, University of Utah, (1968) A-15.
6. L. E. POTEAT and C. E. YUST, *J. Amer. Ceram. Soc.* **49** (1966) 410.
7. E. M. PASSMORE, R. H. DUFF and T. VASILOS, *ibid* **11** (1966) 594.
8. T. VASILOS, J. B. MITCHELL and R. M. SPRIGGS, *ibid* **47** (1964) 203.
9. R. C. GIFKINS and K. U. SNOWDEN, *Trans. Met. Soc. AIME* **239** (1967) 910.
10. T. H. ALDEN, *Acta Met.* **15** (1967) 469.
11. A. H. HEUER, R. M. CANNON and N. J. TIGHE, in "Ultra fine-Grain Ceramics", edited by J. J. Burke, N. L. Reed and V. Weiss (Syracuse University Press, New York, 1970).
12. T. SUGITA and J. PASK, *J. Amer. Ceram. Soc.* **53** (1970) 609.
13. R. KOSSOWSKY, *J. Mater. Sci.* **8** (1973) 1803.

Received 22 November 1974 and accepted 8 January 1975.

Reprinted from the Journal of The American Ceramic Society, Vol. 58, No. 11-12, November-December, 1975
Copyright 1975 by The American Ceramic Society

Creep Deformation of Reaction-Sintered Silicon Nitrides

SALAH UD DIN* and PATRICK S. NICHOLSON*

Department of Metallurgy and Materials Science, McMaster University, Hamilton, Ontario, Canada

The steady-state creep behavior of reaction-bonded silicon nitride, prepared by slip casting and injection molding, was examined in 4-point bending with stresses ranging from 10,000 to 20,000 psi at temperatures from 1200° to 1450°C. Creep rates were proportional to the 1.4 power of the stress. The creep process exhibited an activation energy of 130 ± 5 kcal/mol. The microstructure of deformed specimens, which was revealed by transmission and scanning electron microscopy, contained triple-point voids suggesting that the rate-controlling mechanism of creep is grain-boundary sliding.

I. Introduction

THREE major techniques are used to fabricate polycrystalline Si_3N_4: hot-pressing, slip casting, and injection molding. Hot-pressing has the advantage of fully densifying Si_3N_4, but complex mechanical parts cannot be fabricated easily using this technique. Components prepared by slip casting and injection molding are generally less dense, but these techniques facilitate the fabrication of complex shapes.

Silicon nitrides are prime candidates for use in high-temperature gas turbines. Creep is an essential parameter for the proper selection and application of ceramic materials in the gas turbine; little creep data has been reported in the open literature on Si_3N_4. However, Glenney and Taylor,[1] Stokes *et al.*,[2] Seltzer,[4] and Kossowsky[5] have studied the creep characteristics of high- and low-strength hot-pressed silicon nitrides, and some creep data on slip-cast and injection-molded silicon nitride have recently become available.[3,5-7]

The present work examines the creep behavior of slip-cast and injection-molded Si_3N_4. The creep resistance of these materials is markedly influenced by the impurities they contain. These impurities produce a grain-boundary glassy phase[8] and, thus, exert major control over the high-temperature mechanical properties.

II. Experimental Procedure

(1) Materials

Two grades of slip-cast Si_3N_4 (types A* and B†) and one injection-molded‡ Si_3N_4 were studied. Samples were rectangular bars ⅛ by ⅛ by 1½ in. A complete processing history of the samples is given in Ref. 6. X-ray diffraction analysis showed that the slip-cast materials had a phase composition of 75 wt% α-Si_3N_4 and 25 wt% β-Si_3N_4, and the injection-molded material 65 wt% α-Si_3N_4 and 35 wt% β-Si_3N_4. Emission spectrography was used to analyze the samples (Table I).

Table I. Impurity Analysis* of Creep Samples (in wt%)

Material	Ca	Al	Fe	Ni	Co	V
Slip-cast (type A)	0.1	0.5	0.7			
Slip-cast (type B)	0.04	0.5	0.7			
Injection-molded	0.06	0.5	0.65	0.02	0.01	0.01

*Impurity contents < 0.01 wt% not included.

(2) Creep Testing

The samples were tested in transverse 4-point bending with stresses ranging from 10,000 to 20,000 psi (based on flexure theory) and at temperatures from 1300° to 1450°C in ambient air. By use of a gear system, the load on the sample could be varied instantaneously. An LVDT placed under the load plate in conjunction with an amplifier and a potentiometric recorder was used for measuring the displacement of the bend samples, and strain (ε) was calculated from the deflection. An SiC clamshell furnace with a Pt–Pt13Rh thermocouple was used to heat the samples. Temperature was controlled to within ±5°C.

The stress exponent of the strain rate was determined by changing the load during an experiment and by replotting the strain-rate data from the isothermal creep experiments. The activation energy for the creep process was also determined by (1) replotting the isothermal creep data and (2) changing the temperature during a test and monitoring the response of the creep rate. In both the stress-change and temperature-change experiments, care was taken to allow sufficient time for transient effects accompanying the parameter change to dissipate and for steady-state conditions to be reestablished.

(3) Specimen Preparation for Electron Microscopy

To prepare foils for TEM examination, slices ≈ 1 mm thick were cut with a diamond wheel from the crept samples. The slice was

Received January 25, 1975; revised copy received June 30, 1975.

Supported in part by the Defense Research Board of Canada under Grant No. 7565-09.

*Member, the American Ceramic Society.

*Type NE9, Engine Research Div., Ford Motor Co., Dearborn, MI; contained 3% CaF_2 as a nitriding additive; density = 2.63 g/cm³.

†Type NE8, Ford Motor Co.; contained no nitriding additive; density = 2.69 g/cm³.

‡Ford Motor Co.; contained 1.8% $H_2 + N_2$ as a nitriding additive and nitrided for 36 h at 1260° and 24 h at 1460°C; density = 2.35 g/cm³.

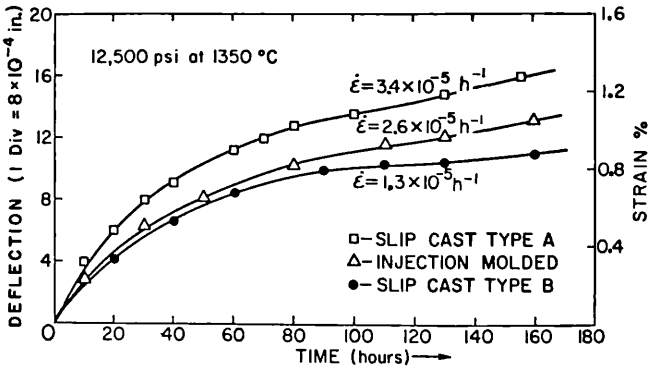

Fig. 1. Creep resistance of slip-cast and injection-molded Si_3N_4.

mounted on a glass slide and carefully ground with a diamond cup wheel to 0.05 mm thick. These samples were removed from the glass slide and thinned to perforation by ion thinning. Samples to be examined by SEM were polished and etched in a mixture of HNO_3. H_2O_2, and HF (5:1:1) at 80°C for 25 min.

III. Results

Comparative creep curves for the slip-cast and injection-molded materials at 12,500 psi and 1350°C are shown in Fig. 1. In all cases, only the primary and secondary stages of creep were noted. Creep fracture was observed at higher temperatures (1450°C) and high stress levels (12,500 psi). The dependence of the creep rate on stress at 1300° and 1350°C is plotted in Fig. 2. The stress exponent (n) of the creep rate in the empirical creep equation

$$\dot{\varepsilon}=\sigma^{n}[(Ae)^{-E/RT}] \qquad (1)$$

(where $\dot{\varepsilon}$ is creep rate, σ stress, and E activation energy) was obtained from the slope of these lines. The exponent was also found by changing the stress during a test and measuring the corresponding strain rate at constant temperature. If a sample has been strained under a certain applied stress (σ_1) and the value of this stress is changed (σ_2), the stress exponent is given by

$$n=\frac{\log\dot{\varepsilon}_2-\log\dot{\varepsilon}_1}{\log\sigma_2-\log\sigma_1} \qquad (2)$$

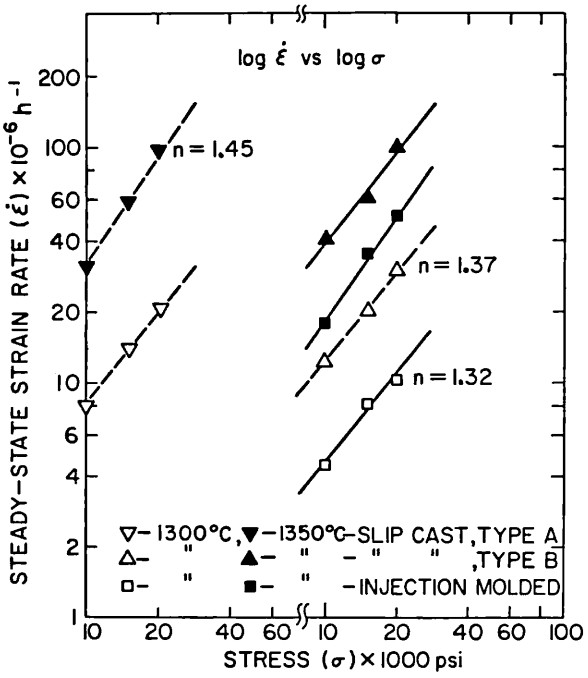

Fig. 2. Creep rate vs stress at constant temperature.

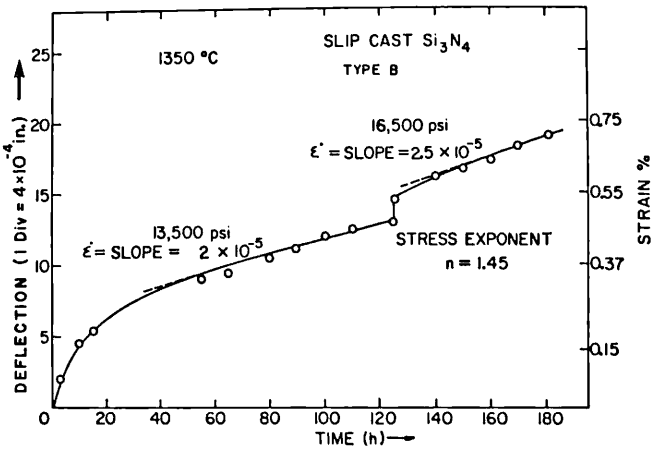

Fig. 3. Typical stress-change plot.

Table II. Activation Energies and Stress Exponents

Material	E(kcal/mol) Arrhenius plots (±5)	E(kcal/mol) Temperature-change experiments	Stress exponent (n) Isobaric tests (±0.01)	Stress exponent (n) Stress-change experiments
Slip-cast				
Type A	125	135	1.45	1.40
Type B	130	134	1.30	1.30
Injection-molded	121	137	1.33	1.40

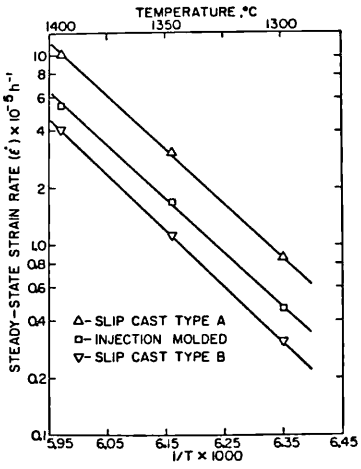

Fig. 4. Plots of log $\dot{\varepsilon}$ vs $1/T$.

A typical result for slip-cast type-B material is shown in Fig. 3. Table II shows the stress exponents and the activation energy results obtained from Arrhenius plots and temperature-change experiments. In Fig. 4, plots of log $\dot{\varepsilon}$ vs $1/T$ are compared for all 3 materials. The activation energy calculated from the slope of each line was approximately the same (≈ 135 kcal/mol). The general straight-line fit of Figs. 2 and 4 suggests that no change in creep mechanism occurred over the ranges of temperature and stress used in the creep test.

Previous studies of creep of some polycrystalline metals have shown the nucleation and growth of voids at triple points by grain-boundary sliding.[9] Fracture occurs when a void reaches a critical size or when a certain part of the cross-sectional area is cracked. The injection-molded specimens fractured during the creep tests in the range 1400° to 1500°C. Figure 5 shows the inverse relation of the type $\dot{\varepsilon}=t_f^{-m}$ ($m\approx 1$), where t_f = time to failure. The linear inverse relation could indicate that the growth rate for voids is controlled by grain-boundary sliding.[9–12]

A characteristic feature of the microstructure of all Si_3N_4 samples investigated was the development of triangular grain-boundary voids during creep. Although the as-received samples were not theoretically dense, no such triple-point porosity was noted in TEM studies. The remnant porosity in these materials is probably too large to be studied by TEM and is therefore difficult to define using

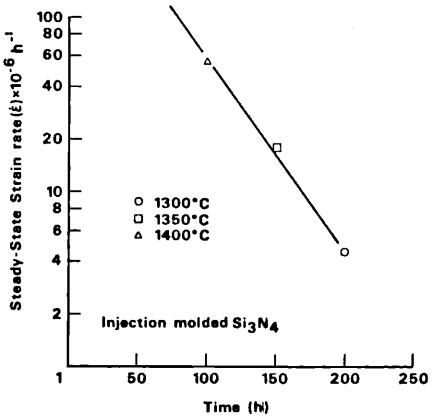

Fig. 5. Steady-state creep rate vs time-to-fracture.

this technique. Grain-boundary void development in slip-cast material (type A) is shown in Figs. 6 and 7. Similar voids developed in both slip-cast and injection-molded materials in a direction normal to the tensile stress; these voids varied in size from 0.5 to 1 μm, the larger sizes being located farthest from the neutral axis of the bend specimen.

The voids increased in both size and number with increasing temperature and stress, indicating void development and growth during creep. Results of TEM studies of crept hot-pressed Si_3N_4 materials showed localized plastic flow to occur adjacent triple-point voids, indicating some accommodation of the generated stresses by plastic deformation.[13] The present TEM studies of all 3 reaction-sintered samples revealed less evidence of such mechanisms. Electron diffraction showed that the grains which contain dislocations were mostly β-Si_3N_4.

IV. Discussion

The results of the present investigation and a previous one on hot-pressed Si_3N_4[13] suggest that the creep resistance of these materials could depend on two factors, i.e. impurity content and the proportion of α phase present in the microstructure. The development of voids during creep of the slip-cast and injection-molded materials suggests that the primary mechanism of creep is grain-boundary sliding. This process can be facilitated by a liquid silicate phase on grain boundaries. Spectrographic examination of the present materials revealed such a phase with the composition CaO-$2Al_2O_3$-$2SiO_2$.[14] Reducing the Ca levels from 0.1 wt% (type A) to 0.04 wt% (type B) decreases the steady-state creep rate by half. This observation is in agreement with the increasing refractoriness of the system $CaO \cdot 2Al_2O_3 \cdot 2SiO_2$ as CaO content is reduced.[15] The lower stress exponent values for these materials as compared with those for hot-pressed Si_3N_4[13] ($n = 1.8$) agrees with the TEM evidence of lack of plastic deformation around slipped grain boundaries. Dislocation activity indicating such deformation was observed in the crept hot-pressed material.

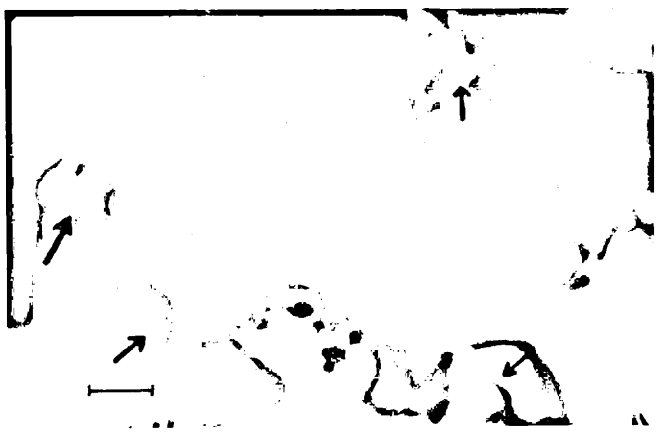

Fig. 6. Transmission electron micrograph of thin section from a crept sample of slip-cast (type A) material (bar = 0.1 μm).

Fig. 7. Scanning electron micrograph of bent specimen of slip-cast (type A) material (bar = 0.1 μm).

The influence of phase composition (percent α- vs percent β-Si_3N_4) is suggested by comparison of the slip-cast type-B (0.04 wt% Ca) and injection-molded (0.06 wt% Ca) materials. The 10% increase in β-Si_3N_4 content in the injection-molded material could be responsible for its lower creep resistance. This explanation is strengthened by the observation of dislocations in some β-Si_3N_4 grains and their comparative rarity in α-Si_3N_4.

V. Conclusions

(1) The calcium impurity level seems to influence markedly the creep rate of Si_3N_4, possibly because of its lower refractoriness as CaO levels are increased in the glassy grain-boundary phase.

(2) The creep resistance of slip-cast and injection-molded Si_3N_4 might be improved by increasing the proportion of α phase while decreasing the Ca content.

(3) Under similar test conditions, activation energies and stress exponents of creep are lower for reaction-sintered Si_3N_4 than for hot-pressed materials.

(4) A grain-boundary-sliding model can explain both the development of voids at triple points and the observed creep kinetics.

References

[1] E. Glenny and T. A. Taylor, "Mechanical Strength and Thermal Fatigue Characteristics of Silicon Nitride," *Powder Met.*, **8**, 164–95 (1961).

[2] R. F. Stokes, R. J. Lumby, and R. F. Coe, "Hot Pressing of Alpha Silicon Nitride Powder"; for abstract see *Am. Ceram. Soc. Bull.*, **51** [4] 428 (1972).

[3] A. F. McLean, E. A. Fisher, and D. E. Harrison, "Brittle Materials Design, High Temperature Gas Turbine," Technical Reports prepared by Army Materials and Mechanics Research Center, Watertown, MA, 1971–72.

[4] M. S. Seltzer, "High-Temperature Creep of Si_3N_4 and Sialons"; for abstract see *Am. Ceram. Soc. Bull.*, **54** [4] 398 (1975).

[5] R. Kossowsky, "Microstructure of Hot-Pressed Silicon Nitride," *J. Mater. Sci.*, **8** [11] 1603–15 (1973).

[6] J. A. Mangels; pp. 195–206 in Ceramics for High Performance Applications. Edited by J. J. Burke, R. N. Gorum, and A. E. Katz. Brook Hill Publishing Co., Chestnut Hill, MA, 1974.

[7] J. A. Mangels, "Effect of H_2-N_2 Nitriding Atmospheres on the Properties of Reaction-Sintered Si_3N_4," *J. Am. Ceram. Soc.*, **58** [7–8] 354–55 (1975).

[8] S. Wild, P. Grieveson, K. H. Jack, and M. J. Latimer; pp. 271–87 in Special Ceramics, Vol. 5. Edited by P. Popper. The British Ceramic Research Association, Stoke-on-Trent, 1972.

[9] R. C. Gifkins, "Mechanism for the Formation of Intergranular Cracks When Boundary Sliding Occurs," *Acta Metall.*, **4** [1] 98–99 (1956).

[10] A. Gittins and H. D. Williams, "Effect of Creep Rate on the Mechanism of Cavity Growth," *Philos. Mag.*, **16**, 849–51 (1967).

[11] C. K. L. Davies and S. K. Sinha Ray; pp. 193–207 in Ref. 8.

[12] F. C. Monkman and N. J. Grant, "Empirical Relation Between Rupture Life and Minimum Creep Rate in Creep-Rupture Tests," *Proc. Am. Soc. Test. Mater.*, **56**, 593 (1956).

[13] S. Ud Din and P. S. Nicholson, "Creep of Hot-Pressed Silicon Nitride," *J. Mater. Sci.*, **10**, 1375–80 (1975).

[14] J. A. Mangels, Ford Motor Co.; private communication.

[15] E. M. Levin, C. R. Robbins, and H. F. McMurdie, Phase Diagrams for Ceramists. Edited by M. K. Reser. The American Ceramic Society, Inc., Columbus, OH, 1964.